INFORMATION TO USERS

The most advanced technology has been used to photograph and reproduce this manuscript from the microfilm master. UMI films the text directly from the original or copy submitted. Thus, some thesis and dissertation copies are in typewriter face, while others may be from any type of computer printer.

The quality of this reproduction is dependent upon the quality of the copy submitted. Broken or indistinct print, colored or poor quality illustrations and photographs, print bleedthrough, substandard margins, and improper alignment can adversely affect reproduction.

In the unlikely event that the author did not send UMI a complete manuscript and there are missing pages, these will be noted. Also, if unauthorized copyright material had to be removed, a note will indicate the deletion.

Oversize materials (e.g., maps, drawings, charts) are reproduced by sectioning the original, beginning at the upper left-hand corner and continuing from left to right in equal sections with small overlaps. Each original is also photographed in one exposure and is included in reduced form at the back of the book.

Photographs included in the original manuscript have been reproduced xerographically in this copy. Higher quality 6" x 9" black and white photographic prints are available for any photographs or illustrations appearing in this copy for an additional charge. Contact UMI directly to order.

U·M·I

University Microfilms International
A Bell & Howell Information Company
300 North Zeeb Road, Ann Arbor, MI 48106-1346 USA
313 761-4700 800 521-0600

Order Number 9110958

Interfacial properties of fluid phases in two dimensions and of three-component surfactant systems

Chen, Li-Jen, Ph.D.

Rice University, 1989

U·M·I

300 N. Zeeb Rd.
Ann Arbor, MI 48106

RICE UNIVERSITY

INTERFACIAL PROPERTIES OF FLUID PHASES IN TWO DIMENSIONS AND OF THREE-COMPONENT SURFACTANT SYSTEMS

by

Li-Jen Chen

A THESIS SUBMITTED
IN PARTIAL FULFILLMENT OF THE
REQUIREMENTS FOR THE DEGREE

DOCTOR OF PHILOSOPHY

APPROVED, THESIS COMMITTEE

Dr. Marc Robert, Director
Associate Professor of Chemical Engineering

Dr. Riki Kobayashi
Professor of Chemical Engineering

Dr. Mark D'Evelyn
Assistant Professor of Chemistry

Houston, Texas

June, 1989

INTERFACIAL THICKNESS OF FLUID PHASES IN TWO DIMENSIONS AND OF THREE-COMPONENT SURFACTANT SYSTEMS

by Li-Jen Chen

ABSTRACT

In this thesis, we study two fundamental problems in the theory and experiment of interfaces in simple and complex fluids.

The first problem concerns the behavior of the interface of simple fluids in two dimensions of space. This is a controversial problem for which no exact results are available and no experimental measurements have been performed, and for which the two leading phenomenological theories, the non-classical van der Waals theory and the capillary wave theory of Buff, Lovett, and Stillinger, make contradictory predictions for the critical behavior of the interfacial thickness in two dimensions of space. We study this problem using both theory and computer simulations.

In our theoretical study of this problem, the equilibrium interface is assumed, in accord with current ideas, to consist of an intrinsic interface of the non-classical van der Waals type broadened by capillary wave fluctuations. It is shown that in two dimensions of space, but not in three, the interfacial thickness exhibits a crossover with change of critical exponent from capillary wave behavior at low and near-critical temperatures to intrinsic structure behavior at temperatures extremely close to the critical temperature. The location of the crossover temperature is determined by a critical amplitude ratio. From available experimental

data and theory, an estimate of the order of magnitude of the critical amplitude ratio is given from which the crossover is found to occur in the temperature range 3×10^{-4} K < T_c - T < 0.3 K, approximately at T_c - T=10^{-3} K. In the currently accessible temperature range, the capillary wave prediction prevails, in contrast to the case of three-dimensional systems.

In our computer simulation study of this problem, the interfacial thickness between two two-dimensional fluid phases is determined as a function of temperature by using the method of molecular dynamics. The model fluid is one of 242 particles interacting via a truncated Lennard-Jones potential. The temperature is varied between that of the triple point to values as close to the critical point as is consistent with the finiteness of the system studied on the computer. Within statistical uncertainty, the results for the interfacial thickness are found to be consistent with the prediction of the non-classical van der Waals theory of the intrinsic interface.

The second problem studied in this thesis concerns the wetting behavior of three-component surfactant systems. In a three-phase equilibrium system, the middle phase either wets or does not wet the interface between the upper and lower phases. In this work, we perform a systematic experimental search for wetting transitions between wetting and nonwetting behaviors in the three-component systems water/n-alkane/C_iE_j, where C_iE_j denotes the surfactant polyoxyethylene alcohol $C_iH_{2i+1}(OC_2H_4)_jOH$. It is found that two systems, water/n-hexadecane /C_6E_2 and water/n-octadecane/C_6E_2, exhibit a wetting transition lying at least 10 ^oC below the upper critical temperature, and one system, water/n-tetradecane/C_6E_2, exhibits a wetting transition lying 4.3 ^oC below the upper critical temperature.

ACKNOWLEDGEMENTS

I would like to express my sincere gratitude to the following persons and organizations:

Professor M. Robert: for his instructive and enlightening guidance as my thesis advisor, for the sharing of his profound knowledge, and for his generosity with the time and efforts to improve the quality of this thesis.

Professor T.W. Leland: for his guidance as my thesis advisor until his death in 1986. His humanity and scholarship are highly respected.

Professor G. Ali Mansoori: for his hospitality during my 1986-1987 visiting and for substantial discussions on mixing rules.

Dr. J.-F. Jeng: for his frequent fruitful discussions and constructive suggestions on my study of microemulsions.

Mr. M. Knackstedt: for collaborating on parts of the theoretical study of interfaces in two dimensions and the early stage of the computer simulation study.

Professors R. Kobayashi and M. D'Evelyn: for serving on my thesis committee.

The National Science Foundation, the Gas Research Institute and the Texas Advanced Technology Program: for financial support.

This thesis is dedicated to my parents for their support and love.

TABLE OF CONTENTS

		Page
ABSTRACT		i
ACKNOWLEDGEMENTS		iii
TABLE OF CONTENTS		iv
LIST OF FIGURES		vi
LIST OF TABLES		xii
CHAPTER 1	THEORETICAL BACKGROUND	1
	1.1 VAN DER WAALS THEORY	2
	1.2 CAPILLARY WAVE THEORY	11
	1.3 THE CONTRADICTION BETWEEN VAN DER WAALS AND CAPILLARY WAVE THEORIES IN TWO DIMENSIONS	15
CHAPTER 2	CROSSOVER FROM CAPILLARY WAVE TO VAN DER WAALS BEHAVIOR IN THE CRITICAL REGION	20
	2.1 THERMAL BROADENING OF INTRINSIC INTERFACE IN ARBITRARY DIMENSION	21
	2.2 EXPRESSION FOR INTERFACIAL THICKNESS	28
	2.3 CRITICAL BEHAVIOR OF INTERFACIAL THICKNESS AND CROSSOVER TEMPERATURE	31
CHAPTER 3	COMPUTER SIMULATION STUDY OF INTERFACIAL STRUCTURE IN TWO-DIMENSIONAL FLUIDS	40
	3.1 COMPUTER SIMULATION	41

3.2 MOLECULAR DYNAMICS METHOD 43
3.2.1 Equations of Motion 43
3.2.2 Algorithm of Predictor-Corrector Method 46
3.2.3 Periodic Boundary Conditions 52
3.2.4 Neighbor Lists 56
3.2.5 Initiation 57
3.2.6 Equilibration 62
3.3 SIMULATION OF A TWO-DIMENSIONAL VAPOR LIQUID PHASE EQUILIBRIUM 63
3.4 RESULTS AND DISCUSSION 68
3.5 SUGGESTED FURTHER WORKS 100
CHAPTER 4 INTERFACIAL PHASE TRANSITIONS IN THREE-COMPONENT SURFACTANT SYSTEMS 102
4.1 PHASE BEHAVIOR OF THREE-COMPONENT SURFACTANT SYSTEMS 104
4.2 WETTING AND NONWETTING REGIMES 111
4.3 EXPERIMENTAL 117
4.4 RESULTS AND DISCUSSION 122
4.5 SUGGESTED FURTHER WORKS 128
REFERENCES 138

LIST OF FIGURES

		Page
Fig. 1.1	A vapor-liquid phase equilibrium.	3
Fig. 1.2	Density profile of liquid-vapor interface shown in Fig. 1.1.	3
Fig. 1.3	Free energy density of hypothetical uniform system in two-phase region.	7
Fig. 1.4	Capillary wave $\zeta(x)$.	12
Fig. 2.1	(a) Intrinsic interface; (b) Capillary wave; (c) Intrinsic interface distorted by capillary wave.	23
Fig. 2.2	Variation of the interfacial thickness L as a function of the dimensionless temperature t for various values of the amplitude ratio R.	36
Fig. 2.3	Variation of the slope S as a function of the dimensionless temperature t for various values of the amplitude ratio R.	38
Fig. 3.1	Illustration of use of periodic boundary conditions for a two-dimensional system.	53
Fig. 3.2	Illustration of minimum image convention.	55
Fig. 3.3	Use of two one-dimensional arrays to store neighbor-list for each particle.	58
Fig. 3.4	Triangular lattice structure used to initiate the simulation for a two-dimensional Lennard-Jones fluid of 121 particles.	60

Fig. 3.5 Schematic illustration of the construction of the vapor-liquid interface from the equilibrated bulk liquid slab shown to the left. 65

Fig. 3.6 Density profiles for a Lennard-Jones fluid at T*=0.433 obtained by averaging over (a) 10,000 (b) 50,000 (c) 100,000 and (d) 300,000 time steps. 67

Fig. 3.7 Density profile of a two-dimensional Lennard-Jones fluid at T*=0.424 obtained by averaging over 250,000 time steps. 70

Fig. 3.8 Density profile of a two-dimensional Lennard-Jones fluid at T*=0.433 obtained by averaging over 300,000 time steps. 71

Fig. 3.9 Density profile of a two-dimensional Lennard-Jones fluid at T*=0.436 obtained by averaging over 300,000 time steps. 72

Fig. 3.10 Density profile of a two-dimensional Lennard-Jones fluid at T*=0.441 obtained by averaging over 300,000 time steps. 73

Fig. 3.11 Density profile of a two-dimensional Lennard-Jones fluid at T*=0.446 obtained by averaging over 300,000 time steps. 74

Fig. 3.12 Density profile of a two-dimensional Lennard-Jones fluid at T*=0.456 obtained by averaging over 120,000 time steps. 75

Fig. 3.13 Density profile of a two-dimensional Lennard-Jones fluid at T*=0.461 obtained by averaging over 300,000 time steps. 76

Fig. 3.14 Density profile of a two-dimensional Lennard-Jones fluid at T*=0.468 obtained by averaging over 300,000 time steps. 77

Fig. 3.15 Density profile of a two-dimensional Lennard-Jones fluid at T*=0.474 obtained by averaging over 200,000 time steps. 78

Fig. 3.16 Variation of the interfacial thickness L as a function of the dimensionless temperature t . 79

Fig. 3.17 Intermediate results for the density profile at T*=0.424. Each curve is obtained by averaging over 50,000 time steps. 80

Fig. 3.18 Intermediate results for the density profile at T*=0.433. Each curve is obtained by averaging over 50,000 time steps. 81

Fig. 3.19 Intermediate results for the density profile at T*=0.436. Each curve is obtained by averaging over 100,000 time steps. 82

Fig. 3.20 Intermediate results for the density profile at T*=0.441. Each curve is obtained by averaging over 100,000 time steps. 83

Fig. 3.21 Intermediate results for the density profile at T*=0.446. Each curve is obtained by averaging over 100,000 time steps. 84

Fig. 3.22 Intermediate results for the density profile at T*=0.456. Each curve is obtained by averaging over 40,000 time steps. 85

Fig. 3.23 Intermediate results for the density profile at T*=0.461. Each curve is obtained by averaging over 100,000 time steps. 86

Fig. 3.24 Intermediate results for the density profile at T*=0.468. Each curve is obtained by averaging over 100,000 time steps. 87

Fig. 3.25 Intermediate results for the density profile at T*=0.474. Each curve is obtained by averaging over 100,000 time steps. 88

Fig. 3.26 Snapshot of the particle positions at T*=0.424 after a trajectory of 250,000 time steps following equilibration. 91

Fig. 3.27 Snapshot of the particle positions at T*=0.433 after a trajectory of 300,000 time steps following equilibration. 92

Fig. 3.28 Snapshot of the particle positions at T*=0.436 after a trajectory of 300,000 time steps following equilibration. 93

Fig. 3.29 Snapshot of the particle positions at T*=0.441 after a trajectory of 300,000 time steps following equilibration. 94

Fig. 3.30 Snapshot of the particle positions at T*=0.446 after a trajectory of 300,000 time steps following equilibration. 95

Fig. 3.31 Snapshot of the particle positions at T*=0.456 after a trajectory of 120,000 time steps following equilibration. 96

Fig. 3.32 Snapshot of the particle positions at T*=0.461 after a trajectory of 300,000 time steps following equilibration. 97

Fig. 3.33 Snapshot of the particle positions at T*=0.468 after a trajectory of 300,000 time steps following equilibration. 98

Fig. 3.34 Snapshot of the particle positions at T*=0.474 after a trajectory of 100,000 time steps following equilibration. 99

Fig. 4.1 Schematic illustration of three phases in equilibrium: (a) nonwetting; (b) wetting. 103

Fig. 4.2 Three types of phase equilibrium according to Winsor.[53] 106

Fig. 4.3 Schematic illustration of simple microemulsion phase behavior as a function of system parameter (here temperature). 108

Fig. 4.4 Evolution of the three-phase triangles with rising temperature for three surfactant systems. 110

Fig. 4.5 (a) Phase volume percentage and (b) surface tensions of the three-phase region of the system water/n-decane/ C_8E_3 . 114

Fig. 4.6 Qualitative behavior of surface tensions for systems with two wetting transition temperatures T_w^l and T_w^u . 118

Fig. 4.7 Schematic illustration of the observation of the wetting transition from nonwetting (a) to wetting (b). 121

Fig. 4.8 Schematic illustration of the observation of Perrot, Robert and Beysens[69] of the wetting transition from nonwetting (a) to wetting (b) in a optical cell. 126

Fig. 4.9 Nonwetting middle phase in the system water/n-hexadecane/ C_6E_2 at T=25 ^{0}C:

(a) Lens; 131

(b) Ring. 132

Fig. 4.10 Nonwetting middle phase in the system water/n-hexadecane/ C_6E_2 at T=35 ^{0}C. 133

Fig. 4.11 Nonwetting middle phase in the system water/n-hexadecane/ C_6E_2 at T=42 ^{0}C. 134

Fig. 4.12 Wetting middle phase in the system water/n-hexadecane/C_6E_2 at T=49.1 ^{0}C. 135

Fig. 4.13 Wetting middle phase in the system water/n-hexadecane/C_6E_2 at T=50 ^{0}C. 136

LIST OF TABLES

		Page
Table 1.1	Critical exponent of the interfacial thickness as a function of dimension of space.	19
Table 3.1	Values of parameter C_i proposed by Gear[44] in predictor-corrector algorithm for nth order predictors.	51
Table 3.2	Statistical averages for the bulk phases and the interfacial thickness.	69
Table 4.1	The three-component systems water/n-alkane/C_iE_j used in the search of the wetting transition temperature.	123
Table 4.2	The wetting transition temperature T_w and the upper critical temperature T_u of the systems water/n-alkane/ C_6E_2.	124

CHAPTER 1

THEORETICAL BACKGROUND

When a two-fluid phase equilibrium is brought close to its critical point, the two coexisting fluid phases become more and more alike, the surface tension of the interface which separates them decreases, and the thickness of the interface increases considerably. As the critical point is reached, the two previously distinct fluid phases merge into a single fluid phase, the surface tension vanishes, and the interfacial thickness becomes infinite. Of course, in the presence of an external field such as gravity, the phase equilibrium is driven away from criticality, so that the otherwise vanishing (divergent) quantities remain nonzero (finite), even when the system is at its critical point. In particular, at and above the critical point itself, where a single fluid phase exists, an external field induces density gradients in the system.[1] This leads for example to the familiar barometric law describing the decrease with altitude of atmospheric density and pressure.

In the next two sections, we briefly describe the two leading theories of fluid interfaces, the theory of van der Waals and its more recent extended versions, and the capillary wave theory of Buff, Lovett and Stillinger. While the assumptions of the van der Waals theory is now known to be incorrect, it is useful to review it and see how some of its features can be retained in a more fundamental theory. Emphasis is given in the last section of this

chapter to the strongly contradictory predictions of these theories for the critical behavior of fluid interfaces in two-dimensional phase equilibria.

1.1 VAN DER WAALS THEORY

In 1889 van der Waals[2], using concepts and ideas of Poisson[3] and Maxwell[4], developed an elegant theory of fluid interfaces in the neighborhood of the critical point. A basic assumption of the van der Waals theory is that there exists an intrinsic structure of the interface characterized by a continuous density profile, i.e., a continuous variation of density across the interface, in contrast to the treatments of Young[5] and Becker[6] who assumed the density profile to be a step-function of vanishing thickness. It is further assumed in the van der Waals theory that the equilibrium interfacial structure is definable without any reference either to a macroscopic external field such as gravity or to a finite interfacial area. Such assumptions are now known to be incorrect.[7] In the van der Waals theory, the nonzero thickness of the interface arises from the spontaneous density or composition fluctuations in the coexisting bulk phases. Of course, this view is not the original one of van der Waals, who never used fluctuations in his works; it emerged in the modern extension of his theory, which is described below.

Consider, for simplicity, a vapor-liquid phase equilibrium of a one-component fluid, as shown in Fig. 1.1. The distance z is measured along the direction normal to the interface. The density profile $\rho(z)$ gives the mean density at height z across the interface and is depicted in Fig. 1.2. The location of z=0 can be specified by a Gibbs dividing surface of vanishing

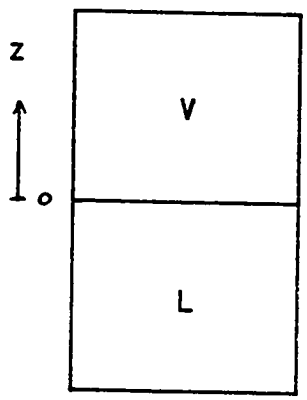

Fig. 1.1 A vapor-liquid phase equilibrium.

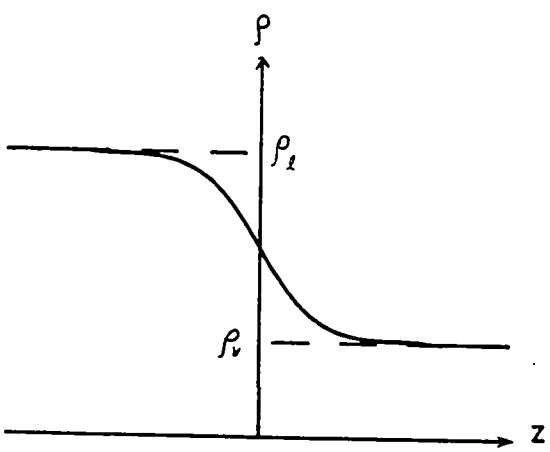

Fig. 1.2 Density profile of liquid-vapor interface shown in Fig. 2.1.

superficial density of matter; that is, z=0 is chosen subject to the condition that the first moment of the density gradient $\rho'(z)$ vanishes, i.e.,

$$\int_{-\infty}^{\infty} z\rho'(z)dz = 0 , \tag{1.1}$$

or, equivalently

$$\int_{-\infty}^{0} (\rho(z)-\rho_L)dz + \int_{0}^{\infty} (\rho(z)-\rho_V)dz = 0 , \tag{1.2}$$

where ρ_L and ρ_V are the number densities of the bulk liquid and vapor phases, respectively.

In the van der Waals theory, one assumes also the existence of a local Helmholtz free energy density $\Psi(z)$. The total Helmholtz free energy A of this inhomogeneous liquid-vapor system can then be obtained from

$$A = a \int_{-\infty}^{\infty} \Psi(z)dz , \tag{1.3}$$

where a is the interfacial area.

The free energy A can be rewritten as a sum of contributions from the vapor, liquid, and interfacial phases by integrating eqn. (1.3) by parts, obtaining:

$$A = a\,[\, z\Psi(z) \mid_{z=\infty} - z\Psi(z) \mid_{z=-\infty} - \int_{-\infty}^{\infty} z\Psi'(z)dz \,]$$

$$= A_V + A_L + A_S\,, \qquad (1.4)$$

where $\Psi'(z)$ is the derivative with respect to z of the free energy density, the subscripts V, L, and S denote respectively the vapor, liquid, and interfacial phases, and

$$A_S = -\,a \int_{-\infty}^{\infty} z\Psi'(z)dz\,. \qquad (1.5)$$

The surface tension σ can be defined as the superficial density of the Helmholtz free energy of the interfacial phase,

$$\sigma = \frac{A_S}{a}\,,$$

$$= -\int_{-\infty}^{\infty} z\Psi'(z)dz\,. \qquad (1.6)$$

It also can be expressed as

$$\sigma = \int_{-\infty}^{\infty} [\Psi(z) - \mu\rho(z)]dz\,, \qquad (1.7)$$

where μ is the chemical potential of the bulk phases.

The free energy density $\Psi(z)$ can be viewed as a functional of $\rho(z)$, i.e., $\Psi(z) = \Psi(\rho(z))$. Expanding $\Psi(z)$ up to second order yields:

$$\Psi(z) = \psi[\rho(z)] + \frac{1}{2}m[\rho'(z)]^2 , \qquad (1.8)$$

where $\psi(\rho)$ is the free energy density as a function of the density ρ for a fixed value of the temperature T, and m is proportional to the second moment of the attractive part of the intermolecular potential $\phi_{attr}(r)$; in three dimensions of space, we have:

$$m = -\frac{1}{6}\int r^2 \phi_{attr}(r) d^3r . \qquad (1.9)$$

It is one of the essential and most disputable postulates of the van der Waals theory that the function $\psi(\rho)$ admits an analytical continuation from the one-phase region into the two-phase region, and is related to the true energy density $\psi^+(\rho)$ by the double tangent construction shown in Fig. 1.3.

Eqns. (1.1) and (1.7)-(1.9) constitute the basis of the original theory of van der Waals.

In the modern extension[8] of the van der Waals theory, the parameter m can be shown to be proportional to the second moment of the direct correlation function $c(\rho,r)$ of Ornstein and Zernike:

$$m = \frac{kT}{6}\int r^2 c(\rho,r) d^3r , \qquad (1.10)$$

where k is Boltzmann's constant and T is the absolute temperature. The numerical factor in eqn. (1.10) is that appropriate to a three-dimensional system.

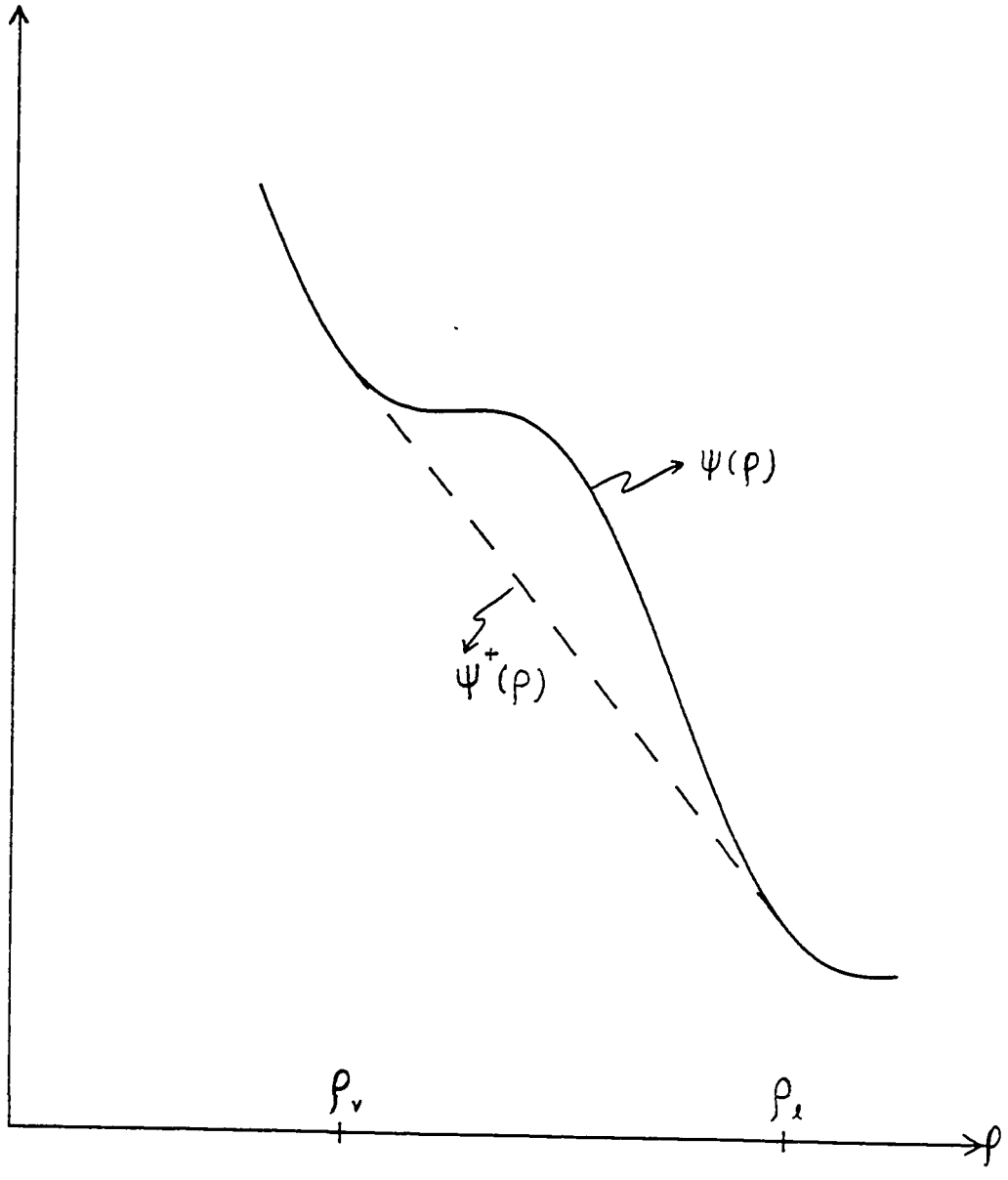

Fig. 1.3 Free energy density of hypothetical uniform system in two-phase region.

The equilibrium density profile is by definition that function $\rho(z)$ which minimizes the free energy functional (1.3), with $\Psi(z)$ given by eqn.(1.8). In solving this variational problem, the Euler-Lagrange equation is used to minimize the surface tension σ in eqn.(1.7) subject to the constraint (1.1), with $\Psi(z)$ given by eqn.(1.8). One finds

$$\psi(\rho) - \mu\rho(z) = \frac{1}{2}m[\rho'(z)]^2 . \tag{1.11}$$

It is a characteristic of the van der Waals theory that the free energy associated with a density inhomogeneity contains a term proportional to the square of the density gradient. For that reason, this theory is sometimes called the squared-gradient theory.

The density profile can be obtained at once by integrating eqn. (1.11),

$$z = \int \sqrt{\frac{m}{2\Delta\psi(\rho)}}\, d\rho , \tag{1.12}$$

where $\Delta\psi(\rho) = \psi(\rho) - \mu\rho$.

Substitution of eqns. (1.8) and (1.11) into eqn. (1.7) gives a simple expression of the surface tension,

$$\sigma = \int_{-\infty}^{\infty} m[\rho'(z)]^2 dz , \tag{1.13}$$

or, equivalently,

$$\sigma = \int_{\rho_v}^{\rho_L} \sqrt{2m\Delta\psi(\rho)}\, d\rho \,. \tag{1.14}$$

In the above calculations, the language used is that appropriate to the vapor-liquid equilibrium in a one-component fluid. The generalization to multicomponent fluid phase equilibria is straightforward and does not involve any new ideas; see, for example, Cahn and Hilliard[9]. These authors assumed the total molecular number density to be constant across the interface; Fleming, Yang, and Gibbs[10] further extended the theory to multicomponent systems, generalizing it to allow for the variation of the number density across the interface.

In the original van der Waals theory, the density profile $\rho(z)$ is derived from a classical equation of state, in which $\Delta\psi(\rho)$ is a quartic, and can be shown to have the analytical form

$$\rho(z) = \frac{1}{2}\left[(\rho_L + \rho_V) - (\rho_L - \rho_V)\tanh\left(\frac{2z}{L}\right)\right], \tag{1.15}$$

where L is the thickness of the interface separating the coexisting phases. If L is assumed to vary as a power law,

$$L = \text{const}\cdot\left(1 - \frac{T}{T_c}\right)^{-\omega} , \tag{1.16}$$

where T_c is the critical temperature, then the critical exponent ω of the interfacial thickness L is found to be equal to $\frac{1}{2}$.[11]

Widom[11] and Buff, Lovett and Stillinger[12] reformulated and extended the van der Waals theory for a fluid in the neighborhood of its critical point. When the non-classical behavior of the compressibility and coexistence curve is taken into account, the theory was found to be in good agreement with experimental[13] results for three-dimensional systems.

In his extension of the van der Waals theory, Widom[11] has given heuristic scaling arguments according to which the interfacial thickness L should be identified with the correlation length ξ of the bulk density (composition) fluctuations; i.e.,

$$L \sim \xi$$
$$= \text{const} \cdot (1 - \frac{T}{T_c})^{-\upsilon}, \quad \upsilon > 0 \ . \tag{1.17}$$

The numerical value of the critical exponent υ is close to 0.64 in three dimensions of space, while in two dimensions of space $\upsilon=1$ is an exact result due to Kaufman and Onsager[15] for the two-dimensional Ising (lattice gas) model with nearest-neighbor forces. Therefore, according to Widom's reformulation of the van der Waals theory, one has $\omega=0.64$ in d=3, and $\omega=1$ in d=2. When the interfacial thickness is identified with the bulk correlation length, as it should according to Widom, this reformulated van der Waals theory becomes equivalent to the Ornstein-Zernike, Debye theory of molecular correlations in a homogeneous fluid.[14]

Replacing the classical equation of state originally used by van der Waals by a more accurate non-classical equation of state, Fisk and Widom[16] showed that the density profile is given by

$$\rho(z) = \frac{1}{2}\left\{(\rho_L + \rho_v) - (\rho_L - \rho_v)\sqrt{\frac{2}{3}}\frac{\tanh\left(\frac{\sqrt{6z}}{L}\right)}{\sqrt{1 - \frac{1}{3}\tanh^2\left(\frac{\sqrt{6z}}{L}\right)}}\right\}. \qquad (1.18)$$

For identical values of $\rho_L - \rho_v$ and L, this profile is qualitatively similar to the classical profile (1.15), although slightly less steep. Remarkably enough, optical reflectivity measurements[13] are able to discriminate between the density profile given by eqns. (1.15) and (1.18).

1.2 CAPILLARY WAVE THEORY

In direct contrast to the assumptions of the van der Waals theory, the capillary wave theory[12] assumes that the diffuseness of the interface is due to purely interfacial fluctuations, which are associated to the capillary and gravity waves, and which have no analog in the bulk.

In the capillary wave theory, one considers an infinitely sharp but rough interface separating two coexisting fluid phases in d dimensions. Fig. 1.4 shows a typical capillary wave distortion $\zeta(\mathbf{x})$. The probability $p[\zeta(\mathbf{x})]$ of a single-valued distortion ζ of the sharp interface is given by

$$p[\zeta(\mathbf{x})] = \text{const} \cdot \exp\{-\beta W[\zeta(\mathbf{x})]\}, \qquad (1.19)$$

where $W[\zeta(\mathbf{x})]$ is the energy necessary to distort the flat interface to $\zeta(\mathbf{x})$, $\mathbf{x}$ is a $(d-1)$-dimensional vector, shown in Fig. 1.4, which describes position in the transverse directions parallel to the interfacial plane, and $\beta = 1/kT$.

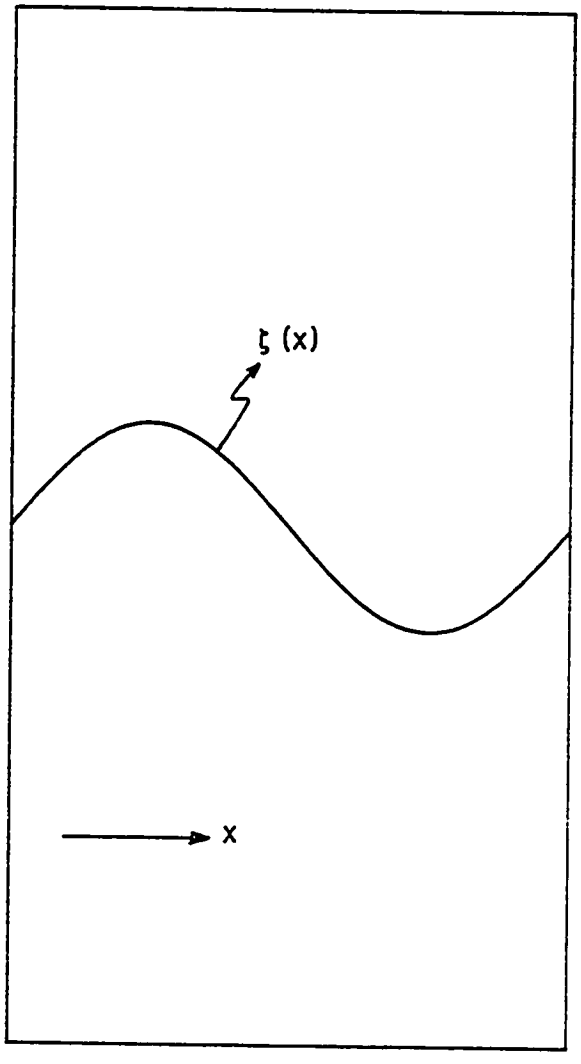

Fig. 1.4 Capillary wave $\zeta(x)$.

The energy $W[\zeta(\mathbf{x})]$ is composed of work against gravity and work against a bare surface tension σ_o, which is the surface tension of the infinitely sharp fluctuating interface, i.e.,

$$W[\zeta(\mathbf{x})] = \sigma_o \int \sqrt{1+|\nabla\zeta(\mathbf{x})|^2}\, d\mathbf{x} - \sigma_o \int d\mathbf{x} + \frac{1}{2} g\Delta\rho \int \zeta^2(\mathbf{x}) d\mathbf{x}, \qquad (1.20)$$

where $\Delta\rho$ is the difference between the densities of the two coexisting bulk phases and g is the acceleration of gravity.

Expanding the integrand of the first integral in eqn. (1.20) to second order in $|\nabla\zeta(\mathbf{x})|^2$ reduces eqn. (1.20) to

$$W[\zeta(\mathbf{x})] = \frac{\sigma_o}{2} \int |\nabla\zeta(\mathbf{x})|^2 d\mathbf{x} + \frac{1}{2} g\Delta\rho \int \zeta^2(\mathbf{x}) d\mathbf{x}. \qquad (1.21)$$

We next decompose the single-valued distortion ζ into decoupled surface waves

$$\zeta(\mathbf{x}) = \sum_{\mathbf{k}} a_{\mathbf{k}} \exp(i\mathbf{k}\cdot\mathbf{x}), \qquad (1.22)$$

with $\mathbf{k}$ the wave vector of a surface wave and $a_{\mathbf{k}}$ its amplitude. Introducing eqn.(1.22) to eqn.(1.21), the energy W becomes

$$W(a_{\mathbf{k}}) = \frac{1}{2} g L^{d-1} \Delta\rho \sum_{\mathbf{k}} a_{\mathbf{k}}^2 \left(1+\frac{1}{2}|\mathbf{k}|^2 l^2\right), \qquad (1.23)$$

where L is the transverse edge length of the system and l is the capillary length defined by

$$l = \sqrt{\frac{2\sigma_o}{g\Delta\rho}}. \tag{1.24}$$

From eqns. (1.19) and (1.23), the equilibrium average of the squared amplitude $a_{\mathbf{k}}$ is found to be

$$\langle a_{\mathbf{k}}^2 \rangle = \frac{\int_0^\infty a_{\mathbf{k}}^2 \exp[-\beta W(a_{\mathbf{k}})] da_{\mathbf{k}}}{\int_0^\infty \exp[-\beta W(a_{\mathbf{k}})] da_{\mathbf{k}}},$$

$$= \frac{1}{\beta g L^{d-1} \Delta\rho \left(1 + \frac{1}{2} l^2 |\mathbf{k}|^2\right)} \quad . \tag{1.25}$$

The mean-squared thickness of the interface is defined by:

$$\langle \zeta^2 \rangle = \sum_{\mathbf{k}} \langle a_{\mathbf{k}}^2 \rangle$$

$$= \sum_{\mathbf{k}} \left\{ \beta g L^{d-1} \Delta\rho \left(1 + \frac{1}{2} l^2 |\mathbf{k}|^2\right) \right\}^{-1}, \tag{1.26}$$

from which one can determine the critical behavior of the interfacial thickness in any dimension of space.

At the limit of a large system ($L \to \infty$), we can evaluate the sum in eqn.(1.26) as an integral and find the mean-squared thickness to be of the form

$$<\zeta^2> = \frac{1}{2\pi\beta g\Delta\rho} \int_0^{|\mathbf{k}_{max}|} \frac{|\mathbf{k}|^{d-2}}{1+\frac{1}{2}l^2|\mathbf{k}|^2} d|\mathbf{k}| \,. \tag{1.27}$$

1.3 THE CONTRADICTION BETWEEN VAN DER WAALS AND CAPILLARY WAVE THEORIES IN TWO DIMENSIONS

In two dimensions (d=2), carrying out the integration in eqn. (1.27) yields[17a]

$$<\zeta^2> = \frac{1}{\sqrt{2}\pi\beta g\Delta\rho l} \arctan\left(\frac{l\,|\mathbf{k}_{max}|}{\sqrt{2}}\right), \tag{1.28}$$

where $|\mathbf{k}_{max}|$ is of the order of the inverse interfacial thickness.[12,17]

There are two limiting cases: one for $l\,|\mathbf{k}_{max}| \gg 1$ and another for $l\,|\mathbf{k}_{max}| \ll 1$. In three-dimensional fluids,[18] the former case corresponds to the temperature range 10^{-3} C < T_c-T < 10 C, while the latter one corresponds to T_c-T << 10^{-5} C. In the latter case, the assumptions underlying capillary wave theory can no longer be considered realistic[19];

moreover such temperatures are usually not accessible to experiment. We therefore only consider the regime $l\,|\mathbf{k}_{max}| >> 1$.

For large y, one may use the approximation $\arctan(y) \approx \pi/2 - 1/y$, and eqn.(1.28) can then be approximated by

$$<\zeta^2> \approx \frac{1}{2\sqrt{2}\beta g \Delta\rho l} = \frac{1}{4\beta\sqrt{2\sigma_o g \Delta\rho}}. \tag{1.29}$$

In the neighborhood of the critical point, we have the power law behaviors:

$$\Delta\rho \sim (\Delta\rho)_o \left(1 - \frac{T}{T_c}\right)^{\beta}, \tag{1.30}$$

$$\sigma_o \sim \sigma_{oo} \left(1 - \frac{T}{T_c}\right)^{\mu}, \tag{1.31}$$

where $(\Delta\rho)_o$ and σ_{oo} are critical amplitudes which do not depend on the temperature.

With known exact values ($\beta = \frac{1}{8}$, and $\mu = 1$) of the critical exponents in two-dimensional fluids with short-ranged forces, it is found from eqn.(1.29) that the interfacial thickness L, which is equal to $<\zeta^2>^{1/2}$, diverges like

$$L \sim \left(1 - \frac{T}{T_c}\right)^{-\frac{\mu+\beta}{4}},$$

$$= \left(1 - \frac{T}{T_c}\right)^{-\frac{9}{32}}, \tag{1.32}$$

so that $\omega=\frac{9}{32}$.

In three dimensions (d=3), we find by integrating eqn. (1.27) that

$$<\zeta^2>=\frac{1}{2\pi\beta g\Delta\rho l^2}\ln\left(1+\frac{1}{2}l^2|\mathbf{k}_{max}|^2\right). \qquad (1.33)$$

The interfacial thickness $L=<\zeta^2>^{1/2}$ is now found to diverge like

$$L\sim\frac{1}{\sqrt{g\Delta\rho l^2}},$$

$$\sim\frac{1}{\sqrt{\sigma_o}},$$

so that:

$$L\sim\left(1-\frac{T}{T_c}\right)^{-\frac{\mu}{2}}. \qquad (1.34)$$

With μ=1.26 in three dimensions of space, one finds[12] ω=0.63 in good agreement with experimental results obtained by optical reflectivity measurements.[13]

In Table 1.1, we summarize the predictions for the value of the critical exponent ω of the interfacial thickness according to the non-classical van der Waals theory and the capillary wave theory in arbitrary dimension of space d. The value of the exponent ω predicted by both theories in d=4 can be straightforwardly obtained by following the arguments

mentioned previously. As is well known from Wilson's renormalization group theory, d =4 is appropriate for very long-ranged forces.

Remarkably, the two completely different van der Waals and capillary wave theories are seen to make identical predictions for the value of the critical exponent ω of the interfacial thickness in three or more dimensions of space. In addition, both theories predict the hyperscaling-like relation $\mu=(d-1)\omega$, with μ the critical exponent of the surface tension.

However, in two dimensions of space the value of the critical exponent ω predicted by capillary wave theory is seen to differ significantly from that predicted by the non-classical van der Waals theory. We return to this important difference in the following two chapters.

Table 1.1 Critical exponent of the interfacial thickness as a function of dimension of space.

d	2	3	4
ω_{cw} [a]	$\frac{9}{32}$	~0.64	$\frac{1}{2}$
ω_{vdw} [b]	1	~0.64	$\frac{1}{2}$

[a] ω_{cw} denotes prediction of capillary wave theory in the case of a gravitational external field.

[b] ω_{vdw} denotes prediction of non-classical van der Waals theory.

CHAPTER 2

CROSSOVER FROM CAPILLARY WAVE TO VAN DER WAALS BEHAVIOR IN THE CRITICAL REGION

It is a current belief shared by most authors that a consistent picture of the fluid interface is one in which both capillary wave and spontaneous bulk density (composition) fluctuations are simultaneously present. This belief is supported by theoretical studies[20,21] and by analyses of experimental results[22].

Far from the critical point, where the interfacial thickness is very small, of the order of a few angströms for ordinary simple fluids, the original capillary wave theory[12] has been shown to offer a valid description of the interfacial structure.[23] As the critical point is approached, it is generally believed, on the basis of heuristic arguments[24], that the thickness of the interface becomes proportional to the correlation length of the spontaneous density (composition) fluctuations in either bulk phases. This point of view is supported by recent ellipsometric measurements[25] which indicate, as the critical temperature is approached, a crossover from capillary wave to van der Waals behavior.

Of course, as we mentioned earlier, extremely close to the critical point, the gravity-induced density gradients become very pronounced and ultimately prevent the interfacial thickness from diverging at the critical

point itself. However, for Earth gravity, which is very weak, such effects occur so close to the critical temperature as to be generally unobservable[1].

In this chapter, we analyze the critical behavior of the interfacial thickness in two dimensions of space with emphasis on the crossover from capillary wave behavior at low temperatures to van der Waals behavior at near-critical temperatures. In Section 2.1, a unified picture which combines the bulk fluctuations of the van der Waals theory and the capillary wave fluctuations is introduced. An analytical expression for the interfacial thickness is derived in Section 2.2 by assuming the intrinsic density profile of the van der Waals theory to be given by a simple exponential. It is then shown in Section 2.3 that the interfacial thickness exhibits a crossover from capillary wave to van der Waals behavior, a critical amplitude ratio playing the key role in determining the location of the crossover temperature. Estimates are given of the order of magnitude of the critical amplitude ratio and of the corresponding crossover temperature.

2.1 THERMAL BROADENING OF INTRINSIC INTERFACE IN ARBITRARY DIMENSION

Let us consider a vapor-liquid interface in d dimensions of space with an arbitrary intrinsic interface broadened by capillary wave fluctuations. We thus generalize the original capillary wave theory described in the previous chapter by replacing the infinitely sharp fluctuating interface with a diffuse fluctuating interface of non-zero thickness, the intrinsic interface.

The probability $p[\zeta(\mathbf{x})]$ of a distortion ζ of the interface is still defined by eqn. (1.19), as in the original capillary wave theory. However, the energy W required to distort the interface from z to $z-\zeta(\mathbf{x})$ is now of the form[21c]

$$W[\zeta(\mathbf{x})] = \sigma_o\int\sqrt{1+|\nabla\zeta(\mathbf{x})|^2}\,d\mathbf{x} - \sigma_o\int d\mathbf{x}$$

$$+ \int\rho_I[z-\zeta(\mathbf{x})]u_{ext}(z)d\mathbf{r} - \int\rho_I(z)u_{ext}(z)d\mathbf{r}\,, \qquad (2.1)$$

where $u_{ext}(z)$ is the external field taken to depend on the coordinate z only, ρ_I is the intrinsic density profile, $\mathbf{x}$ is a $(d-1)$-dimensional vector describing position in the transverse directions parallel to the interfacial plane, and $d\mathbf{r}=d\mathbf{x}dz$. The distorted intrinsic profile $\rho_I[z-\zeta(\mathbf{x})]$ is schematically illustrated in Fig. 2.1.

Expanding the distorted profile $\rho_I[z-\zeta(\mathbf{x})]$ to second order in $\zeta(\mathbf{x})$, assuming $\int\zeta(\mathbf{x})d\mathbf{x}=0$ to preserve the average position of the profile and expanding $\sqrt{1+|\nabla\zeta(\mathbf{x})|^2}$ to second order in $|\nabla\zeta(\mathbf{x})|^2$ reduces eqn. (2.1) to

$$W[\zeta(\mathbf{x})] = \frac{\sigma_o}{2}\int|\nabla\zeta(\mathbf{x})|^2d\mathbf{x} + \frac{1}{2}\int\rho_I''(z)u_{ext}(z)dz\int\zeta^2(\mathbf{x})d\mathbf{x}\,, \qquad (2.2)$$

where $\rho_I''(z)$ is the second derivative of the intrinsic profile $\rho_I(z)$ with respect to the coordinate z. Integrating by parts the second term in eqn. (2.2) yields

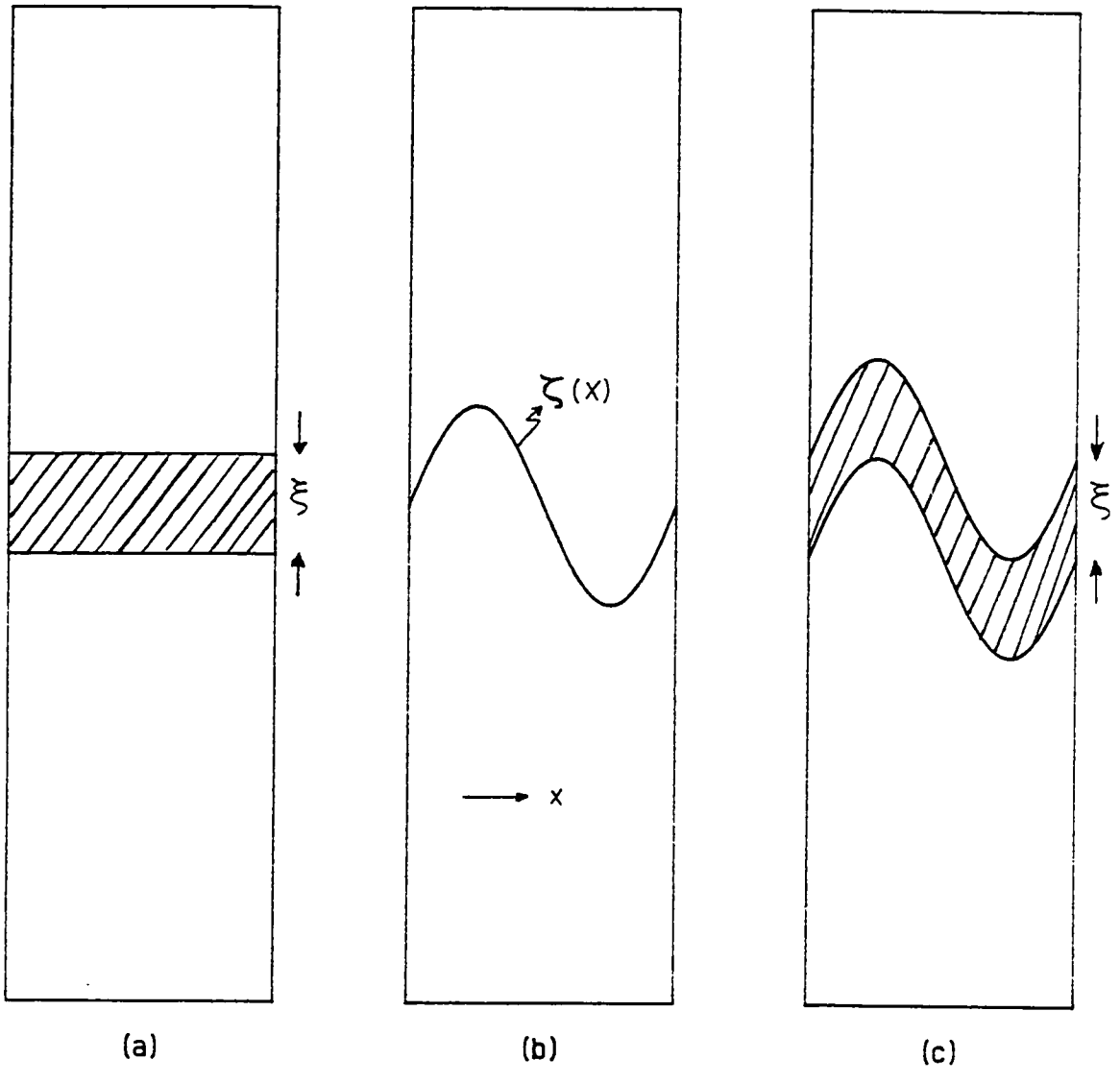

Fig. 2.1
(a) Intrinsic interface;
(b) Capillary wave;
(c) Intrinsic interface distorted by capillary wave.

$$W[\zeta(\mathbf{x})] = \frac{\sigma_o}{2}\int |\nabla\zeta(\mathbf{x})|^2 d\mathbf{x} - \frac{1}{2}\int \rho_I'(z) u_{ext}'(z) dz \int \zeta^2(\mathbf{x}) d\mathbf{x} . \qquad (2.3)$$

Assuming the fluctuations of the intrinsic interface as a whole to be capillary wave-like, as shown in Fig. 2.1, enables one to decompose the distortion ζ into surface waves:

$$\zeta(\mathbf{x}) = \sum_{\mathbf{k}} a_{\mathbf{k}} \exp(i\mathbf{k}\cdot\mathbf{x}) . \qquad (2.4)$$

Introducing eqn.(2.4) to eqn.(2.3) yields, as shown by Percus,[21c]

$$W(a_{\mathbf{k}}) = \frac{1}{2} K L^{d-1} \sum_{\mathbf{k}} a_{\mathbf{k}}^2 \left(1 + \frac{1}{2}|\mathbf{k}|^2 l^2\right), \qquad (2.5)$$

where L is as before the transverse edge length of the system, l is the generalized capillary length defined by

$$l = \sqrt{\frac{2\sigma_o}{K}}, \qquad (2.6)$$

and

$$K = -\int_{-\infty}^{+\infty} \rho_I'(z) u_{ext}'(z) dz . \qquad (2.7)$$

The interfacial profile $\rho(z)$ is obtained by averaging over the ensemble of capillary fluctuations $\zeta(\mathbf{x})$ of the intrinsic density profile $\rho_I(z)$, i.e.,

$$\rho(z) = \langle \rho_I[z-\zeta(\mathbf{x})] \rangle , \tag{2.8}$$

where the brackets denote a statistical average over capillary wave fluctuations of the interface.

For our purposes, it is convenient to rewrite the distorted interface $\rho_I[z-\zeta(\mathbf{x})]$ in terms of the δ-function $\delta(y-\zeta)$,

$$\rho_I[z-\zeta(\mathbf{x})] = \int_{-\infty}^{+\infty} \delta[y-\zeta(\mathbf{x})]\rho_I(z-y)dy , \tag{2.9}$$

and to rewrite eqn. (2.9) by making use of the inverse Fourier transform of the δ-function $\delta[y-\zeta(\mathbf{x})]$

$$F^{-1}[\delta(y-\zeta)] = \frac{1}{\sqrt{2\pi}} \int_{-\infty}^{+\infty} \delta(y-\zeta)\exp(iqy)dy$$

$$= \frac{1}{\sqrt{2\pi}} \exp(iq\zeta) ,$$

together with the equivalent form:

$$\delta[y-\zeta(\mathbf{x})] = F\{F^{-1}[\delta(y-\zeta)]\}$$

$$= \frac{1}{2\pi}\int_{-\infty}^{+\infty}\exp(-iqy)\exp(iq\zeta)dq \ . \qquad (2.10)$$

Substituting eqn. (2.10) into eqn. (2.9) yields

$$\rho_I[z-\zeta(\mathbf{x})] = \frac{1}{2\pi}\int_{-\infty}^{+\infty}\rho_I(z-y)\int_{-\infty}^{+\infty}\exp\{-iq[y-\zeta(\mathbf{x})]\}dqdy \ . \qquad (2.11)$$

From eqns. (2.8) and (2.11), the equilibrium density profile $\rho(z)$ is given by

$$\rho(z) = \frac{1}{2\pi}\int_{-\infty}^{+\infty}\rho_I(z-y)\int_{-\infty}^{+\infty}\exp(-iqy)\langle\exp(iq\zeta)\rangle dqdy \ . \qquad (2.12)$$

We introduce new variables η_k to replace the wave amplitudes a_k[26],

$$a_k = \frac{\eta_k + i\eta_{-k}}{\sqrt{2}} \ , \qquad (2.13a)$$

$$a_{-k} = \frac{\eta_k - i\eta_{-k}}{\sqrt{2}} \ , \qquad (2.13b)$$

$$a_0 = \eta_0 \ , \qquad (2.13c)$$

so that eqns. (2.4) and (2.5) can be expressed in terms of the new variables $\eta_{\mathbf{k}}$

$$\zeta(\eta_{\mathbf{k}}) = \sqrt{2} \sum_{\mathbf{k}>0} \left[\eta_{\mathbf{k}} \cos(\mathbf{k}\cdot\mathbf{x}) + \eta_{-\mathbf{k}} \sin(\mathbf{k}\cdot\mathbf{x}) \right] , \tag{2.14}$$

$$W(\eta_{\mathbf{k}}) = \frac{1}{2} K L^{d-1} \Sigma_{\mathbf{k}} \eta_{\mathbf{k}}^2 \left(1 + \frac{1}{2} |\mathbf{k}|^2 l^2 \right) . \tag{2.15}$$

Using eqns. (2.8), and (2.13)-(2.15), we calculate $\langle \exp(iq\zeta) \rangle$ to be[26]

$$\langle \exp(iq\zeta) \rangle = \exp\left(-\frac{q^2 \lambda^2}{2} \right) , \tag{2.16}$$

where λ^2 is the mean-squared thickness of the interface which corresponds to $\langle \zeta^2 \rangle$ in the original capillary wave theory:

$$\lambda^2 = \frac{1}{\beta K L^{d-1}} \sum_{\mathbf{k}} \left(1 + \frac{1}{2} l^2 |\mathbf{k}|^2 \right)^{-1} . \tag{2.17}$$

The Fourier transform in eqn. (2.12) can be performed by using eqn. (2.16) and the resulting density profile is found to be

$$\rho(z) = \frac{1}{\sqrt{2\pi\lambda^2}} \int_{-\infty}^{+\infty} \rho_I(z-\zeta) \exp\left(-\frac{\zeta^2}{2\lambda^2} \right) d\zeta . \tag{2.18}$$

Note that if, following Buff, Lovett, and Stillinger[12], we choose the intrinsic interface to be a step function, i.e.,

$$\rho_I(z) = \rho_l - (\rho_l - \rho_v)\theta(z) , \tag{2.19}$$

with $\theta(z)$ the unit step function, and the external field to be that of gravity, i.e.,

$$u_{ext}(z) = gz , \tag{2.20}$$

then the constant K of eqn. (2.7) is given by $K=g\Delta\rho$, so that l reduces to the ordinary capillary length given by eqn. (1.24). The original capillary wave theory discussed in Section 2.3 is thus seen to be a special case of the present model.

2.2 EXPRESSION FOR INTERFACIAL THICKNESS

In the framework of the intrinsic structure theory, several density profiles have been proposed[27]; we have already encountered examples of those in eqns. (1.15) and (1.18). In this study, the intrinsic density profile $\rho_I(z)$ is taken to be a simple exponential, i.e.:

$$\rho_I(z) = \begin{cases} \rho_v + \frac{1}{2}(\rho_l - \rho_v)\exp\left(-\frac{z}{\xi}\right) & \text{for } z \geq 0 \\ \rho_l - \frac{1}{2}(\rho_l - \rho_v)\exp\left(\frac{z}{\xi}\right) & \text{for } z < 0 \end{cases} , \tag{2.21}$$

where ξ is the bulk correlation length. It is assumed here that the bulk correlation length of the liquid phase is identical to that of the vapor phase. This assumption is valid only when the temperature is close to the critical temperature, where the two coexisting phases are almost identical to each other. It is of interest to note that the density profile given by (2.21) has recently been derived rigorously by Robert and Widom [28] for the one-dimensional lattice gas, in which, due to the symmetry of the model, the bulk correlation length of the two coexisting phase are identical at all temperatures and not only close to the critical point.

If the interfacial thickness L is defined[29] by

$$L = -(\rho_l - \rho_v)\left(\frac{d\rho}{dz}\right)^{-1}_{z=0} , \qquad (2.22)$$

then the interfacial thickness L of the intrinsic density profile (2.21) is equal to 2ξ, and diverges like $(T_c\text{-}T)^{-\upsilon}$ in the neighborhood of the critical point, which is of course the prediction $\omega=\upsilon$ of the van der Waals theory.[24] Other definitions of the interfacial thickness can be used and all yield the same value of the critical exponent ω.

Introducing eqn. (2.21) into eqn. (2.18) yields, after some straightforward algebra, an analytical expression for the density profile:

$$\rho(z) = \frac{1}{2}(\rho_l + \rho_v) - \frac{1}{2}(\rho_l - \rho_v)\,\mathrm{erf}\left(\frac{z}{\sqrt{2}\lambda}\right)$$

$$+\frac{1}{4}(\rho_l - \rho_v)\left[1 + \mathrm{erf}\left(\frac{z - \lambda^2/\xi}{\sqrt{2}\lambda}\right)\right]\exp\left(-\frac{z}{\xi} + \frac{\lambda^2}{2\xi^2}\right)$$

$$-\frac{1}{4}(\rho_l - \rho_v)\left[1 - \mathrm{erf}\left(\frac{z - \lambda^2/\xi}{\sqrt{2}\lambda}\right)\right]\exp\left(\frac{z}{\xi} + \frac{\lambda^2}{2\xi^2}\right)\ , \qquad (2.23)$$

where erf denotes the error function

$$\mathrm{erf}(x) = \frac{2}{\sqrt{\pi}}\int_0^x e^{-q^2}dq\ .$$

It follows that the interfacial thickness L defined by (2.22) is given, for the density profile (2.23):

$$L = \frac{2\xi\cdot\exp\left(-\frac{\lambda^2}{2\xi^2}\right)}{1 - \mathrm{erf}\left(\frac{\lambda}{\sqrt{2}\xi}\right)}\ . \qquad (2.24)$$

We first note that the interfacial thickness L as given by eqn. (2.24) reduces to that of the original capillary wave theory, $L=\sqrt{2\pi}\lambda$, at the limit of an intrinsic profile of vanishing thickness ($\xi=0$). Mathematically, at the limit $\xi \to 0$, the intrinsic density profile (2.21) becomes a step function of the form (2.19), and thus has a vanishing interfacial thickness. The density

profile (2.23) thus reduces, at that limit, to the error function profile well known[12] to correspond to the thermal averaging of capillary wave fluctuations of an infinitely sharp interface.

We also note that the interfacial thickness L given by (2.24) differs from that recently given by Sikkenk, van Leeuwen, Vossnack, and Bakker,[30] according to whom $L^2=\lambda^2+\xi^2$. This difference results from using a different intrinsic density profile $\rho_I(z)$. The latter authors assumed the derivative of the intrinsic density profile $\rho_I(z)$ with respect to z to be a Gaussian with effective width ξ. In addition, they did not assume the same form as (2.1) for the energy W needed to distort the interface but assumed instead W to be of the form (1.20), as in the original treatment of Buff, Lovett and Stillinger. Although the density profile $\rho(z)$ derived by Sikkenk, van Leeuwen, Vossnack, and Bakker[30] also has the same form as (2.18), the mean squared thickness λ^2 assumed by these authors has a form different from (2.17).

2.3 CRITICAL BEHAVIOR OF INTERFACIAL THICKNESS AND CROSSOVER TEMPERATURE

In the neighborhood of the critical point the bulk correlation length ξ and the root mean-squared thickness λ diverge like

$$\xi = \xi_0\left(1-\frac{T}{T_c}\right)^{-\upsilon} \quad , \tag{2.25}$$

and

$$\lambda = \lambda_0 \left(1-\frac{T}{T_c}\right)^{-\varpi} \quad , \tag{2.26}$$

respectively, where ξ_0 and λ_0 are critical amplitudes. Note that the critical exponents υ and ϖ correspond to the critical exponent ω of the interfacial thickness predicted by, respectively, the van der Waals and the generalized capillary wave theories. As mentioned in Chapter 2, υ=1 in d=2, υ=0.64 in d=3 and υ=1/2 in d=4.

The critical exponent ϖ can be determined by following the method used in Section 2.2 to calculate the critical exponent ω in the original capillary theory.

We first convert the sum in eqn. (2.17) into an integral, since we are considering the thermodynamic limit $L \to \infty$ of a large system:

$$\lambda^2 = \frac{1}{2\pi\beta K} \int_0^{|\mathbf{k}_{max}|} \frac{|\mathbf{k}|^{d-2}}{1+\frac{1}{2}l^2|\mathbf{k}|^2} d|\mathbf{k}| \quad . \tag{2.27}$$

In two dimensions of space (d=2), integration of eqn. (2.27) yields

$$\lambda^2 = \frac{1}{\sqrt{2}\pi\beta K l} \arctan\left(\frac{l\,|\mathbf{k}_{max}|}{\sqrt{2}}\right) \quad . \tag{2.28}$$

As mentioned previously, we need only consider the regime $l\,|\mathbf{k}_{max}| \gg 1$. Using the approximation $\arctan(y) \approx \pi/2 - 1/y$ for large y turns eqn. (2.28) into

$$\lambda^2 \approx \frac{1}{2\sqrt{2}\beta K l} ,$$

$$= \frac{1}{4\beta\sqrt{\sigma_o K}} . \qquad (2.29)$$

Here the intrinsic profile is again chosen to be a simple exponential (see eqn. (2.21)) and the external field is taken to be that of gravity (see eqn. (2.20)). From eqn. (2.12), the constant K is then given by

$$K = g\Delta\rho . \qquad (2.30)$$

Introducing eqns. (2.30), (1.30), and (1.31) into eqn. (2.29) yields a mean-squared thickness diverging like:

$$\lambda^2 = \frac{1}{4\beta\sqrt{g\sigma_o(\Delta\rho)_o}}\left(1 - \frac{T}{T_c}\right)^{-\frac{\beta+\mu}{2}} . \qquad (2.31)$$

Taking the square root of eqn.(2.31) and comparing it to eqn. (2.26), gives, by equating the corresponding coefficients to each other:

$$\lambda_o = \left(\frac{1}{16\beta^2 g\sigma_o(\Delta\rho)_o}\right)^{\frac{1}{4}} , \qquad (2.32)$$

and

$$\varpi = \frac{\beta + \mu}{4}$$

$$= \frac{9}{32} . \qquad (2.33)$$

The root-mean-squared thickness λ of the generalized capillary wave theory is thus seen from (2.33) to diverge according to the same power law as that of the original capillary wave theory. It should be pointed out that the critical exponent ϖ is strongly nonuniversal, i.e., field dependent, in two dimensions of space, but it is universal, i.e., field independent, in three or more dimensions of space, ϖ=0.64 in d=3 and $\varpi=\frac{1}{2}$ in d=4.[20a]

Substituting eqns. (2.25) and (2.26) into eqn. (2.24) and setting υ=1 and $\varpi=\frac{9}{32}$ yields

$$L = \frac{2\xi_0 t^{-1} \exp\left(-\frac{R^2}{2} t^{23/16}\right)}{1 - \mathrm{erf}\left(\frac{R}{\sqrt{2}} t^{23/32}\right)} , \qquad (2.34)$$

where the dimensionless temperature t and the amplitude ratio R are defined by

$$t = 1 - \frac{T}{T_c} , \qquad (2.35)$$

and

$$R = \frac{\lambda_o}{\xi_o} , \tag{2.36}$$

respectively.

Fig. 2.2 shows the variation of the interfacial thickness L as a function of the dimensionless temperature t for different values of the amplitude ratio R. All curves exhibit a linear behavior in the region of very small t, where the slope is asymptotically approaching unity, which is the value of the critical exponent ω according to the van der Waals theory. For slightly larger values of the dimensionless temperature t, the curves start to deviate from a straight line, the deviation becoming more pronounced for larger values of R. When the dimensionless temperature t is large enough, i.e., far from the critical point, the curve is seen to cross over to a different linear behavior with an asymptotic slope equal to 9/32, the critical exponent ω of capillary wave theory.

The change of the logarithmic slope S of the interfacial thickness can be expressed analytically in the form

$$S = -\frac{\partial \ln L}{\partial \ln t} ,$$

and we find

$$S = 1 + \frac{23}{32} R^2 t^{23/16} - \frac{23}{32} \sqrt{\frac{2}{\pi}} \frac{R t^{23/32} \exp\left(-\frac{R^2}{2} t^{23/16}\right)}{1 - \mathrm{erf}\left(\frac{R}{\sqrt{2}} t^{23/32}\right)} . \tag{2.37}$$

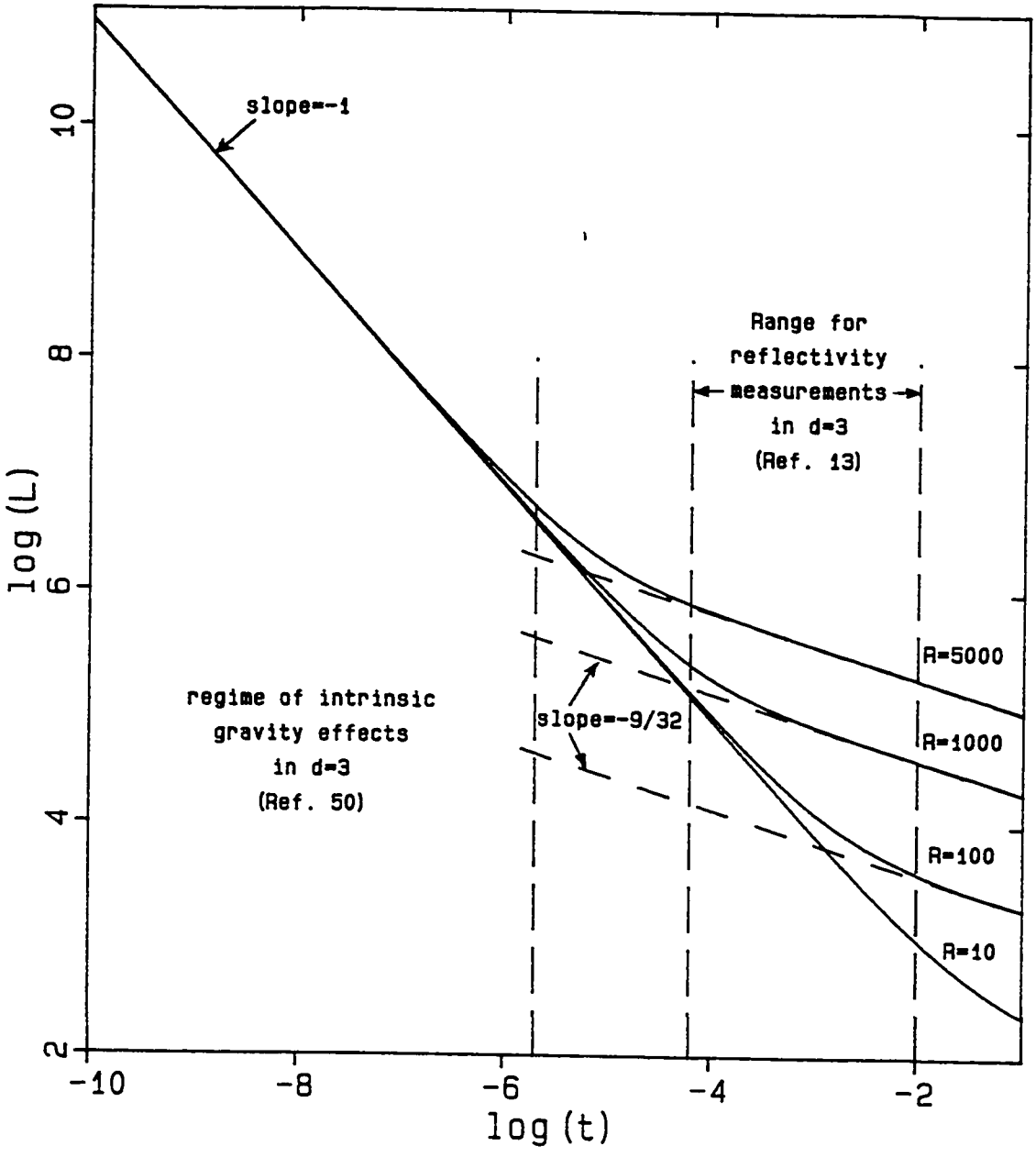

Fig. 2.2 Variation of the interfacial thickness L as a function of the dimensionless temperature t for various values of the amplitude ratio R.

The variation of the logarithmic derivative S as a function of the dimensionless temperature t for various values of the critical amplitude ratio R is shown in Fig. 2.3. Not shown in Fig. 2.3 is the curve for R=5,000, because the latter drops from S=1 to S=9/32 so abruptly that we can not, on this scale, distinguish it from the y-axis. Obviously, the extent of the crossover region depends strongly on the value of R, the curve for larger values of R having a narrower crossover region.

The amplitude ratio R is seen to be the key quantity in determining the critical behavior of the interfacial thickness L. We next estimate, qualitatively, the order of magnitude of the ratio R by combining the available data with theory.

The critical amplitude $(\Delta\rho)_0$ for pentadecanoic acid was found[31] to be 41.9 molecules per 10^4 $\mathring{A}^2$. Although the classical value of the critical exponent of the coexistence curve was used[31], the value of $(\Delta\rho)_0$ is of the same order of magnitude as that obtained for CH_4 by Kim and Chan[32].

Since there are, to the best of our knowledge, no experimental data available for the surface tension amplitude σ_0 for two-dimensional systems, an estimate of σ_0 is made on the basis of the exact result of the two-dimensional Ising model[33] $\sigma_0=\frac{kT}{\xi_0}$, where the amplitude ξ_0 is taken to be the particle diameter, about 10 $\mathring{A}$ (for pentadecanoic acid). The critical temperature of pentadecanoic acid is 300.1±0.2 K.[34] The interfacial thickness amplitude λ_0 can then be calculated from eqn.(2.32), which yields $\lambda_0 \approx 1.0 \times 10^{-4}$ cm. Finally, the amplitude ratio R is computed from its definition (2.36), which gives R≈1000, establishing that the crossover occurs

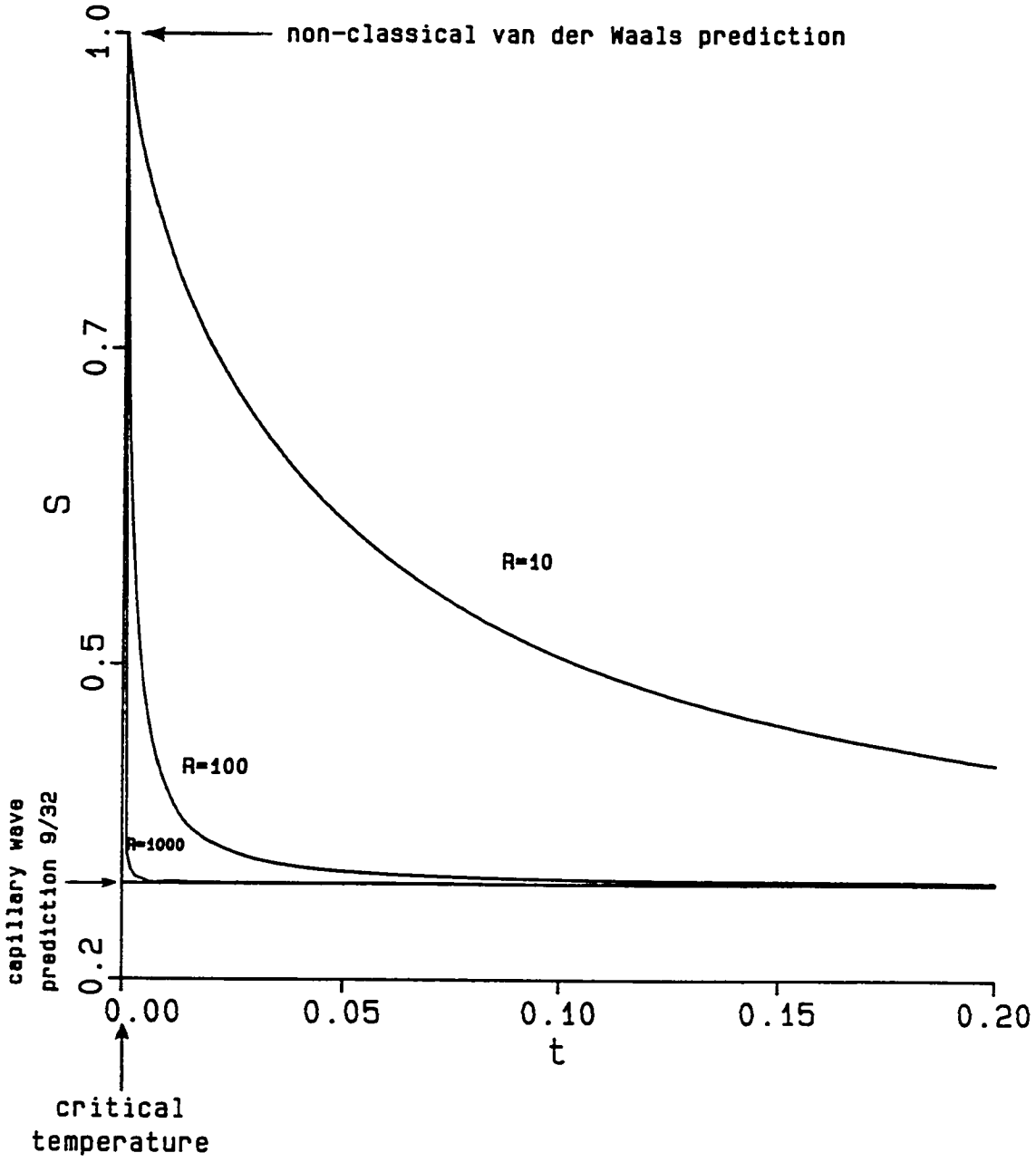

Fig. 2.3 Variation of the slope S as a function of the dimensionless temperature t for various values of the amplitude ratio R.

in the temperature range 3×10^{-4} K< T_c-T < 0.3 K, centered at approximately T_c-T~10^{-3} K (see Fig. 2.2).

The temperature range of Webb's reflectivity measurements[13] on three-dimensional systems is shown in Fig. 2.2. It is seen that within this temperature range, the capillary wave prediction $\omega=\frac{9}{32}$ prevails for R≥1000.

The ratio R is determined from two critical amplitudes, λ_0 and ξ_0. Critical amplitudes, unlike critical exponents, are well known to be nonuniversal, i.e., to depend on the details of the particular system studied. As a consequence, it is likely that R, as a ratio of two critical amplitudes, also depends upon the details of the system of interest. Unfortunately, there are not enough experimental data for us to confirm this expectation. In the following chapter, we will present a computer simulation study of a two-dimensional Lennard-Jones model fluid and attempt to solve this problem.

CHAPTER 3

COMPUTER SIMULATION STUDY OF INTERFACIAL STRUCTURE OF TWO-DIMENSIONAL FLUIDS

Because experimental results on fluid interfaces in two dimensions are most unfortunately not available and exact results are still out of reach, we have turned to computer simulations as a suitable tool to investigate the interfacial structure of two-dimensional fluids. While computer simulations have previously been used to study the structure of fluid interfaces[35], all existing studies of two-dimensional fluids[36] have been restricted to a single temperature and, moreover, to one that lies very far from the critical point, very close indeed to the triple point where the interfacial thickness is very small, of the order of the range of the intermolecular forces themselves.

In this chapter, we use the molecular dynamics method of computer simulations to study the interfacial structure of fluids in two dimensions and to attempt to resolve the problem described above of the strong contradiction between the values of the critical exponent ω of the interfacial thickness predicted by the capillary wave and van der Waals theories. In Section 4.1 we briefly give an overview of the computer simulation method with emphasis on the Monte Carlo and molecular dynamics methods. In Section 4.2 the molecular dynamics method we use is described in detail.

The simulation procedure used in this work for inhomogenous two-dimensional systems is given in Section 4.3. It is shown in Section 4.4 that the results of the interfacial thickness are consistent with the prediction $\omega=1$ of the van der Waals theory. A critical discussion of these results closes this chapter.

3.1 COMPUTER SIMULATION

Molecular dynamics and Monte Carlo methods are the most commonly used computer simulation techniques which simulate the behavior of fluids at the molecular level by considering a small system containing typically one hundred to a few thousand molecules.[37,38,39]

The Monte Carlo method was developed by Metropolis and coworkers[40] to study the diffusion of neutrons in fissionable materials. In a classical Monte Carlo calculation, a system of N particles interacting via a known potential is assigned a set of arbitrarily chosen initial coordinates. A sequence of configurations of the particles is then generated by successive random moves, which are accepted or rejected according to a rule ensuring that configuration space is arranged following the equilibrium probability density appropriate to a chosen statistical ensemble. After generating a long series of such configurations, the various equilibrium properties of the system can be obtained by averaging over these configurations. The sequence of the configurations does not correspond to an evolution of the system in time, and therefore this method can only be used to study equilibrium, but not dynamic, properties.

In principle, the Monte Carlo method is entirely stochastic in nature, in direct contrast to the deterministic nature of the molecular dynamics method. In a conventional molecular dynamics calculation, a system of N particles is confined to a cell of fixed volume. Initial velocities are randomly assigned or taken from a Maxwell-Boltzmann distribution appropriate to the temperature of interest, and chosen in such a way as to make the net linear momentum equal to zero. Specifying the intermolecular potential function, the subsequent trajectories of the particles are then calculated by integrating the Newtonian equations of motion. The thermodynamics properties of interest are finally obtained by averaging over the dynamical history of the system.

Although the Monte Carlo method is easier than that of molecular dynamics to program on the computer, the molecular dynamics method has three important advantages over the Monte Carlo method. First, in addition to the equilibrium properties, molecular dynamics simulations can be used to study time-dependent phenomena and transport properties. Secondly, the molecular trajectories are directly accessible in molecular dynamics simulations and therefore can be used to observe the dynamical history of the microscopic structure of interest. Thirdly, less computer storage space is needed for molecular dynamics simulations. Since the molecular dynamics method offers these additional important features, we choose it to study the interfacial structure of two-dimensional fluids.

3.2 MOLECULAR DYNAMICS METHOD

Originally devised by Alder and Wainwright[41] and applied to the study of hard sphere systems, the molecular dynamics method has been developed by Rahman[42] to treat systems in which the particles interact via continuous potentials. In this Section, we summarize the use of the molecular dynamics method in the microcanonical ensemble (constant N, V, and E).

3.2.1 Equations of Motion

Consider a system of N indistinguishable particles, each having mass m and being confined in a fixed volume V. The Hamiltonian of the system, H_N, is the sum of the kinetic and potential energies,

$$H_N(\mathbf{r}_1, \mathbf{r}_2, \cdots, \mathbf{r}_N, \mathbf{p}_1, \mathbf{p}_2, \cdots, \mathbf{p}_N) = K_N(\mathbf{p}_1, \mathbf{p}_2, \cdots, \mathbf{p}_N) + \Phi_N(\mathbf{r}_1, \mathbf{r}_2, \cdots, \mathbf{r}_N) \ , \tag{3.1}$$

where

$$K_N(\mathbf{p}_1, \mathbf{p}_2, \cdots, \mathbf{p}_N) = \sum_{i=1}^{N} \frac{|\mathbf{p}_i|^2}{2m} \ , \tag{3.2}$$

and

$$\Phi_N(\mathbf{r}_1, \mathbf{r}_2, \cdots, \mathbf{r}_N) = U(\mathbf{r}_1, \mathbf{r}_2, \cdots, \mathbf{r}_N) + \sum_{i=1}^{N} u_{ext}(\mathbf{r}_i) \quad , \tag{3.3}$$

where $\mathbf{r}_i$ and $\mathbf{p}_i$ are the position and momentum, respectively, of particle i, U is the total potential energy and $u_{ext}(\mathbf{r}_i)$ is the energy due to the external field acting on molecule i.

Differentiating eqn. (3.1) with respect to time t yields

$$\frac{dH_N}{dt} = \sum_{i=1}^{N} \frac{\partial H_N}{\partial \mathbf{p}_i} \frac{d\mathbf{p}_i}{dt} + \sum_{i=1}^{N} \frac{\partial H_N}{\partial \mathbf{r}_i} \frac{d\mathbf{r}_i}{dt} \quad . \tag{3.4}$$

Since Hamilton's equations of motion are

$$\frac{\partial H_N}{\partial \mathbf{p}_i} = \frac{d\mathbf{r}_i}{dt} \quad , \tag{3.5a}$$

and

$$\frac{\partial H_N}{\partial \mathbf{r}_i} = -\frac{d\mathbf{p}_i}{dt} \quad , \tag{3.5b}$$

it follows from eqns. (3.4) and (3.5) that:

$$\frac{dH_N}{dt} = 0 \quad , \tag{3.6}$$

i.e., the total energy $E(=H_N)$(kinetic and potential energies) is conserved as well as are N and V. Such an ensemble is called the microcanonical ensemble.

According to the equipartition theorem, in d dimensions of space the instantaneous temperature is proportional to the kinetic energy,

$$T = \frac{m}{d\,Nk} \sum_i \mathbf{r}_i^{(1)} \cdot \mathbf{r}_i^{(1)} \quad , \tag{3.7}$$

where $\mathbf{r}_i^{(1)}(t)$ the derivative of $\mathbf{r}_i$ with respect to t, i.e., the velocity of particle i.

Introducing eqn. (3.1) into eqn. (3.5), with the kinetic energy defined by (3.2), yields the Newtonian equations of motion

$$m\frac{d\mathbf{r}_i}{dt} = \mathbf{p}_i \quad , \tag{3.8a}$$

and

$$\frac{d\mathbf{p}_i}{dt} = -\frac{\partial \Phi_N(\mathbf{r}_1, \mathbf{r}_2, \cdots, \mathbf{r}_N)}{\partial \mathbf{r}_i} \quad ; \tag{3.8b}$$

or, equivalently, combining the last two equations

$$m\mathbf{r}_i^{(2)}(t) = -\frac{\partial \Phi_N(\mathbf{r}_1, \mathbf{r}_2, \cdots, \mathbf{r}_N)}{\partial \mathbf{r}_i} \quad , \tag{3.9}$$

where $\mathbf{r}_i^{(2)}(t)$ is the second derivative of $\mathbf{r}_i$ with respect to t.

In the absence of the external field ($v(\mathbf{r}_i)=0$ in eqn. (3.3)), the Newtonian equations of motion of particle i can be simply expressed, by substituting eqn. (3.3) into eqn. (3.9), as:

$$\mathbf{F}_i(t) = m\mathbf{r}_i^{(2)}(t) = -\frac{\partial U(\mathbf{r}_1, \mathbf{r}_2, \cdots, \mathbf{r}_N)}{\partial \mathbf{r}_i} \tag{3.10}$$

with $\mathbf{F}_i$ the total force acting on particle i.

The trajectories of the particles are determined by the Newtonian equations of motion, which constitute a set of second-order, nonlinear ordinary differential equations. If the potential is continuous, the trajectories of the particles, unlike those of hard spheres, can no longer be calculated exactly. A variety of algorithms have been used to solve these equations numerically, and several have been extensively reviewed.[43]

3.2.2 Algorithm of Predictor-Corrector Method

Here a fifth-order predictor-corrector method is adopted to solve the Newtonian equations. This method consists of three steps: prediction, evaluation, and correction. The sequence "predict-evaluate-correct", when repeated several thousand times, constitutes a molecular dynamics simulation.

In the prediction step, an estimate of the positions, velocities, accelerations, ··· , at time $t+\Delta t$ may be obtained from a Taylor expansion about time t,

$$\mathbf{r}_{ip}(t+\Delta t) = \mathbf{r}_i(t) + \mathbf{r}_i^{(1)}(t)\Delta t + \mathbf{r}_i^{(2)}(t)\frac{(\Delta t)^2}{2!} + \mathbf{r}_i^{(3)}(t)\frac{(\Delta t)^3}{3!} + \mathbf{r}_i^{(4)}(t)\frac{(\Delta t)^4}{4!} + \mathbf{r}_i^{(5)}(t)\frac{(\Delta t)^5}{5!}, \tag{3.11a}$$

$$\mathbf{r}_{ip}^{(1)}(t+\Delta t) = \mathbf{r}_i^{(1)}(t) + \mathbf{r}_i^{(2)}(t)\Delta t + \mathbf{r}_i^{(3)}(t)\frac{(\Delta t)^2}{2!} + \mathbf{r}_i^{(4)}(t)\frac{(\Delta t)^3}{3!} + \mathbf{r}_i^{(5)}(t)\frac{(\Delta t)^4}{4!}, \tag{3.11b}$$

$$\mathbf{r}_{ip}^{(2)}(t+\Delta t) = \mathbf{r}_i^{(2)}(t) + \mathbf{r}_i^{(3)}(t)\Delta t + \mathbf{r}_i^{(4)}(t)\frac{(\Delta t)^2}{2!} + \mathbf{r}_i^{(5)}(t)\frac{(\Delta t)^3}{3!}, \tag{3.11c}$$

$$\mathbf{r}_{ip}^{(3)}(t+\Delta t) = \mathbf{r}_i^{(3)}(t) + \mathbf{r}_i^{(4)}(t)\Delta t + \mathbf{r}_i^{(5)}(t)\frac{(\Delta t)^2}{2!}, \tag{3.11d}$$

$$\mathbf{r}_{ip}^{(4)}(t+\Delta t) = \mathbf{r}_i^{(4)}(t) + \mathbf{r}_i^{(5)}(t)\Delta t \ , \tag{3.11e}$$

$$\mathbf{r}_{ip}^{(5)}(t+\Delta t) = \mathbf{r}_i^{(5)}(t) \ , \tag{3.11f}$$

where the subscript p represents the prediction step and the superscript (i) denotes the ith derivative of **r** with respect to time.

Note that the optimum value of the time increment Δt is a compromise. On the one hand, we wish to have the value of Δt as large as possible in order to sample as much of the trajectory in phase space as possible. However, on the other hand Δt must be small compared to the mean time between molecular collisions, and small enough to reduce the error due to the numerical method.

Eqns. (3.11) will not generate correct trajectories as time evolves, because we have not introduced the equations of motion. In the evaluation step, we calculate, from the new position $\mathbf{r}_{ip}(t+\Delta t)$, the forces at time $t+\Delta t$

$$\mathbf{F}_i(t+\Delta t) = m\mathbf{r}_{ic}^{(2)}(t+\Delta t) = -\frac{\partial U(\mathbf{r}_{1p}, \mathbf{r}_{2p}, \cdots, \mathbf{r}_{Np})}{\partial \mathbf{r}_{ip}} \quad , \tag{3.12}$$

where $\mathbf{r}_{ic}^{(2)}(t+\Delta t)$ is the corrected acceleration of particle i at time $t+\Delta t$.

The total potential energy U of the system is assumed for simplicity to be pairwise additive

$$U(\mathbf{r}_1, \mathbf{r}_2, \cdots, \mathbf{r}_N) = \sum_{i<j} u(r_{ij}) \quad , \tag{3.13}$$

where $r_{ij} = |\mathbf{r}_j - \mathbf{r}_i|$, and $u(r_{ij})$ is the intermolecular pair potential.

In this study the intermolecular pair potential is chosen to be the truncated Lennard-Jones potential

$$u(r_{ij}) = \begin{cases} 4\varepsilon\left[\left(\frac{r_{ij}}{\sigma}\right)^{-12} - \left(\frac{r_{ij}}{\sigma}\right)^{-6}\right] & r_{ij} < r_c \\ 0 & r_{ij} > r_c \end{cases} \quad , \tag{3.14}$$

where ε and σ are the energy and length parameters, respectively, and r_c is the cut-off distance.

Substituting eqn. (3.13) to eqn. (3.12), the total force acting on particle i at time $t+\Delta t$ can be calculated from

$$\mathbf{F}_i(t+\Delta t) = m\mathbf{r}_{ic}^{(2)}(t+\Delta t) = -\sum_{i=j} \frac{\partial u(r_{ij})}{\partial r_{ij}} \mathbf{R}_{ij} \quad . \tag{3.15}$$

Applying the truncated Lennard-Jones potential (3.14) to eqn. (3.15) yields

$$\mathbf{F}_i(t+\Delta t) = \begin{cases} 24 \sum \frac{1}{r_{ij}} \left[2\left(\frac{r_{ij}}{\sigma}\right)^{-12} - \left(\frac{r_{ij}}{\sigma}\right)^{-6} \right] \mathbf{R}_{ij} & \text{for } r_{ij} < r_c \\ 0 & \text{for } r_{ij} > r_c \end{cases} , \tag{3.16}$$

where $\mathbf{R}_{ij}$ is the unit vector in the $\mathbf{r}_{ij}$ direction.

It should be pointed out that the evaluation of the forces is the most time-consuming part of the molecular dynamics simulation, since the sum in (3.16) must be performed for each particle i in the system. The cut-off distance used here significantly reduces the number of pairs contributing to the potential energy and hence the computing time.

The corrected accelerations can be compared with the predicted accelerations to estimate the error in the prediction step,

$$\Delta\mathbf{r}_i^{(2)} = \mathbf{r}_{ic}^{(2)}(t+\Delta t) - \mathbf{r}_{ip}^{(2)}(t+\Delta t) \quad . \tag{3.17}$$

The error term (3.17) is used to correct the predictions made in eqns. (3.11), yielding:

$$\mathbf{r}_i(t+\Delta t) = \mathbf{r}_{ip}(t+\Delta t) + C_0 \Delta\mathbf{r}_i^{(2)} \quad , \tag{3.18a}$$

$$\mathbf{r}_i^{(1)}(t+\Delta t) = \mathbf{r}_{ip}^{(1)}(t+\Delta t) + C_1 \Delta \mathbf{r}_i^{(2)} \quad , \tag{3.18b}$$

$$\mathbf{r}_i^{(2)}(t+\Delta t) = \mathbf{r}_{ip}^{(2)}(t+\Delta t) + C_2 \Delta \mathbf{r}_i^{(2)} \quad , \tag{3.18c}$$

$$\mathbf{r}_i^{(3)}(t+\Delta t) = \mathbf{r}_{ip}^{(3)}(t+\Delta t) + C_3 \Delta \mathbf{r}_i^{(2)} \quad , \tag{3.18d}$$

$$\mathbf{r}_i^{(4)}(t+\Delta t) = \mathbf{r}_{ip}^{(4)}(t+\Delta t) + C_4 \Delta \mathbf{r}_i^{(2)} \quad , \tag{3.18e}$$

$$\mathbf{r}_i^{(5)}(t+\Delta t) = \mathbf{r}_{ip}^{(5)}(t+\Delta t) + C_5 \Delta \mathbf{r}_i^{(2)} \quad , \tag{3.18f}$$

where the parameters C_i are chosen to ensure the numerical stability of the solutions to the differential equations. The values of the parameters C_i depend on the degree of the differential equations and the order of the Taylor expansion used in the prediction step. Table 3.1 gives the values of the parameters C_i proposed by Gear[44] for the third, fourth and fifth order predictions.

The predictor-corrector algorithm can be summarized as follows:

(a) predict the positions, velocities, accelerations, and so on, at time $t+\Delta t$, using the current values of these quantities;

(b) evaluate the forces, and hence the corrected accelerations from the new positions;

(c) correct the predicted positions, velocities, accelerations, and so on, using the corrected accelerations;

Table 3.1 Values of parameter C_i proposed by Gear[44] in predictor-corrector algorithm for nth order predictors.

C_i	n=3	n=4	n=5
C_0	$\frac{1}{6}$	$\frac{19}{120}$	$\frac{3}{16}$
C_1	$\frac{5}{6}$	$\frac{3}{4}$	$\frac{251}{360}$
C_2	1	1	1
C_3	$\frac{1}{3}$	$\frac{1}{2}$	$\frac{11}{18}$
C_4	---	$\frac{1}{12}$	$\frac{1}{6}$
C_5	---	---	$\frac{1}{60}$

(d) collect the data for the properties of interest, such as the density profile in this study;

(e) return to (a) for the next time step.

3.2.3 Periodic Boundary Conditions

The introduction of the simulation cell creates undesirable walls. In reality, a particle hitting a surface would be reflected back inside the cell. Because of the small system size, a comparably large fraction of particles will lie near or on the surface. Surface effects will thus produce a large undesirable contribution to any bulk property we wish to determine. In general, one is interested in properties at the thermodynamic limit, i.e., when the number of particles goes to infinity.

This problem can be overcome by implementing periodic boundary conditions, which are schematically illustrated in Fig. 3.1 for a two-dimensional system. The N particles are placed in a central cell surrounded on all sides by periodically repeated images of the central cell. Thus, as a particle leaves the central cell, one of its images will re-enter the central cell through the opposite surface.

Thanks to the periodic boundary conditions we have eliminated the surfaces and created a quasi-infinite system which mimics a macroscopic system more closely.

Mathematically, periodic boundary conditions can be described as follows:

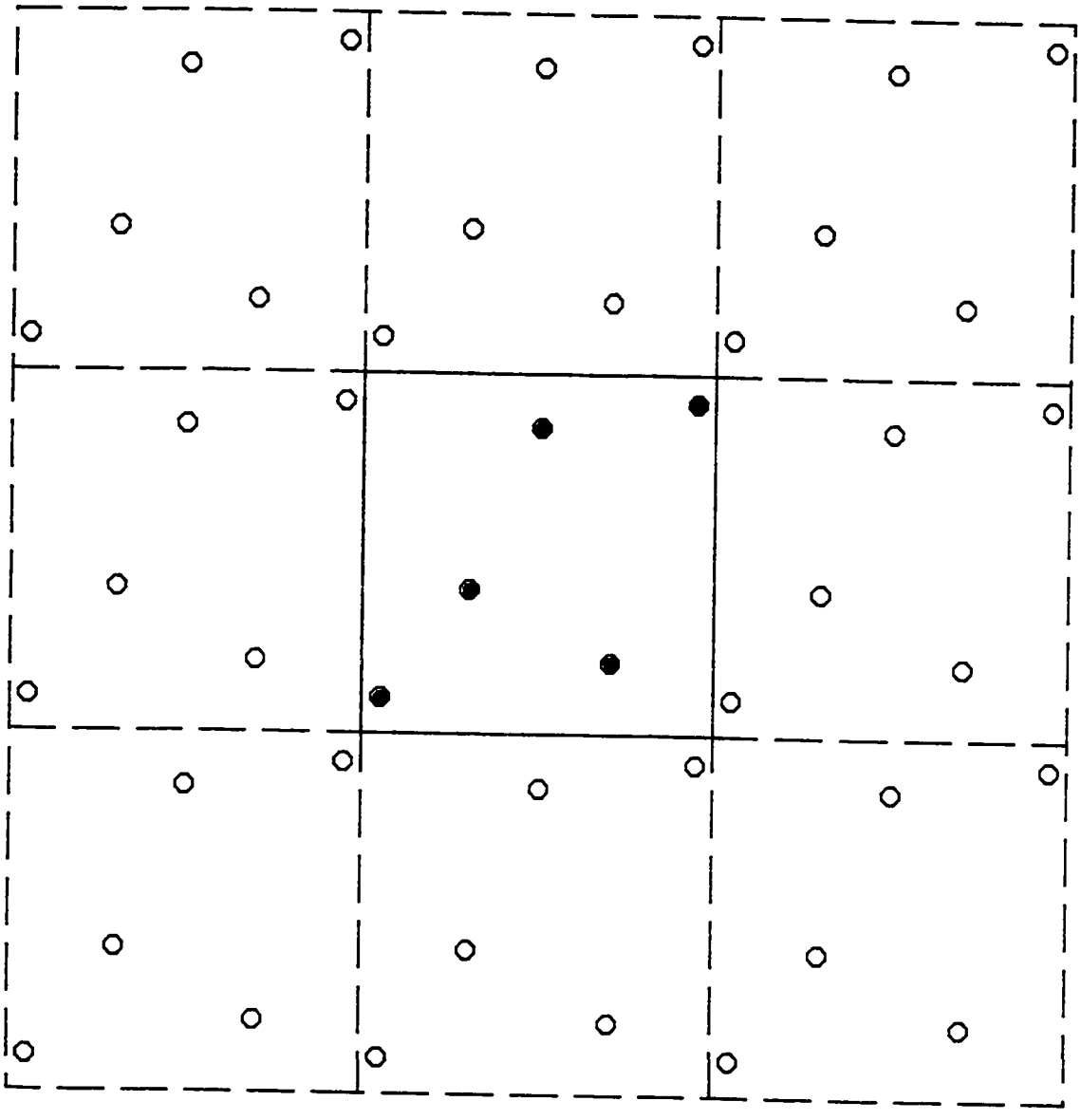

Fig. 3.1 Illustration of use of periodic boundary conditions for a two-dimensional system.

$$x_i^n = \begin{cases} x_i & \text{if } 0 < x_i < L_x \\ x_i + L_x & \text{if } x_i < 0 \\ x_i - L_x & \text{if } x_i > L_x \end{cases} , \qquad (3.19)$$

where L_x is the length of the cell along the x coordinate and the superscript n indicates the new component of x_i. Similar equations hold for the y and z coordinates.

With periodic boundary conditions, the molecular interactions are assumed to extend between particles in the central cell and the image particles in the infinite array. The total potential energy of the system is the sum of all the intermolecular energies. Clearly, it would be impossible to consider all the interactions in this infinite system. The cut-off method mentioned previously is conveniently used to reduce the computational efforts.

When a cut-off distance is used, the interaction of a particle with its neighbors is calculated with a "minimum image convention". The principle of this convention is illustrated in Fig. 3.2. A particle i lying inside the central cell is assumed to interact only with the nearest image particle j (including particle j itself), and there is no interaction if the distance from the nearest image is greater than the cut-off distance r_c.

The cut-off distance r_c is restricted to be smaller than $\frac{L_x}{2}$ (assuming $L_x=L_y=L_z$) to ensure that there is at most one image of particle j (including j itself) lying in any sphere of radius $r_{ij} < \frac{L_x}{2}$ centered on particle i.

Mathematically, the nearest distance can be determined by the coordinate transformations:

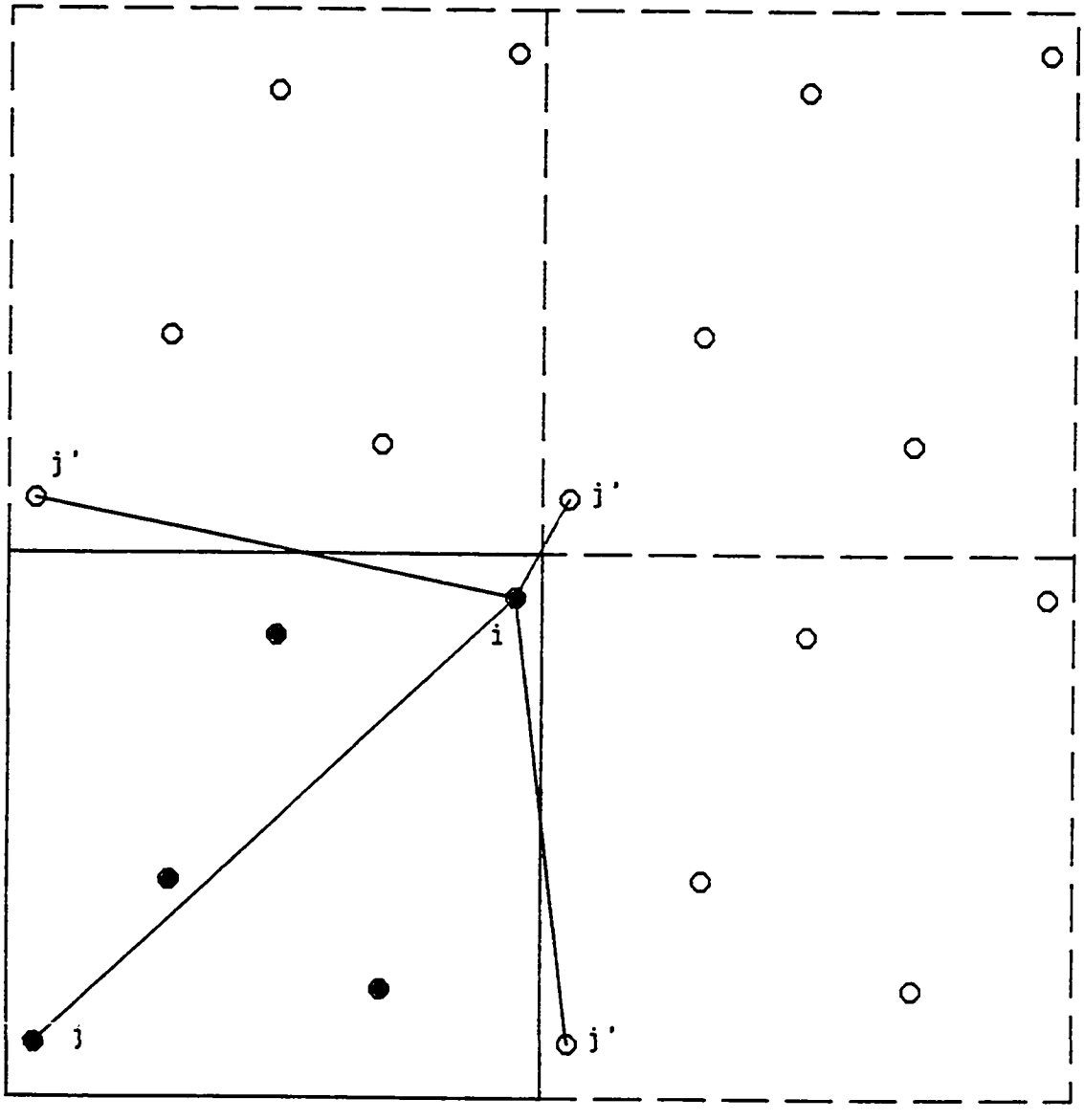

Fig. 3.2 Illustration of minimum image convention.

$$x_{ij}^{n} = \begin{cases} x_{ij} - L_x & \text{if } x_{ij} > \dfrac{L_x}{2} \\ x_{ij} + L_x & \text{if } -x_{ij} > \dfrac{L_x}{2} \end{cases} , \qquad (3.20)$$

and similarly for the y and z coordinates, where x_{ij} is the distance in the x direction between the particles i and j both in the central cell, and x_{ij}^{n} is the distance in the x direction used in the calculation.

It should be pointed out that the use of a cut-off distance is inappropriate when the intermolecular forces are very long-ranged. The problem is most severe for ionic systems, since there is then no guarantee that the system of particles within the cut-off sphere will be electrically neutral.

The introduction of a cut-off distance will create a small error due to neglecting the contributions to the force on particle i due to particle j when $r_{ij} > r_c$. The simulation results can be corrected for this long-ranged interactions by assuming that the radial distribution function is equal to unity for $r_{ij} > r_c$.

3.2.4 Neighbor Lists

We already pointed out in Section 3.2.2 that the most time-consuming calculation in the molecular dynamics simulation is that of the forces on each particle. For a fluid of N particles there are N(N-1)/2 pairs of particles i and j contributing to the force evaluated at each time step. Since the cut-off distance r_c is used, i.e., F_i=0 for $r_{ij} > r_c$, the evaluation of the forces for

$r_{ij} > r_c$ is unnecessary. Verlet[45] proposed a neighbor-list method for improving the speed of a program by maintaining for each particle i a list of neighboring particles that lie within a list distance r_L of particle i, where r_L is slightly larger than r_c. Only particles j from this neighbor list are used to calculate the force acting on particle i. The same neighbor list is used over several consecutive time steps and updated periodically, for example in this study every ten time steps. The list distance r_L is larger than r_c, so that any particles j may move across r_c and still be properly considered in the calculation. In this study, we choose $r_c = 3\sigma$ and $r_L = 3.5\sigma$.

For a vapor-liquid equilibrium of a two-dimensional Lennard-Jones fluid of N=242 particles, some particles in the liquid phase have about 17 neighbors within a circle shell of radius $r=3.5\sigma$. In total, an array LIST of about 3000 elements is needed to store the neighbor list. The elements of another array NABORS serve as pointers that locate for a specific particle the neighbors held in array LIST. The relation between arrays NABORS and LIST is illustrated in Fig. 3.3.

3.2.5 Initiation

To start the predictor-corrector algorithm, values for the $\mathbf{r}_i(t)$ and their derivatives must be assigned at time t=0. The initial positions $\mathbf{r}_i(0)$ may be assigned according to some lattice structure or taken from a previous simulation. It is not efficient to attempt to assign random positions $\mathbf{r}_i(0)$ because in random assignments it is difficult to avoid artificially large overlap of two adjacent particles. Such overlap produces a

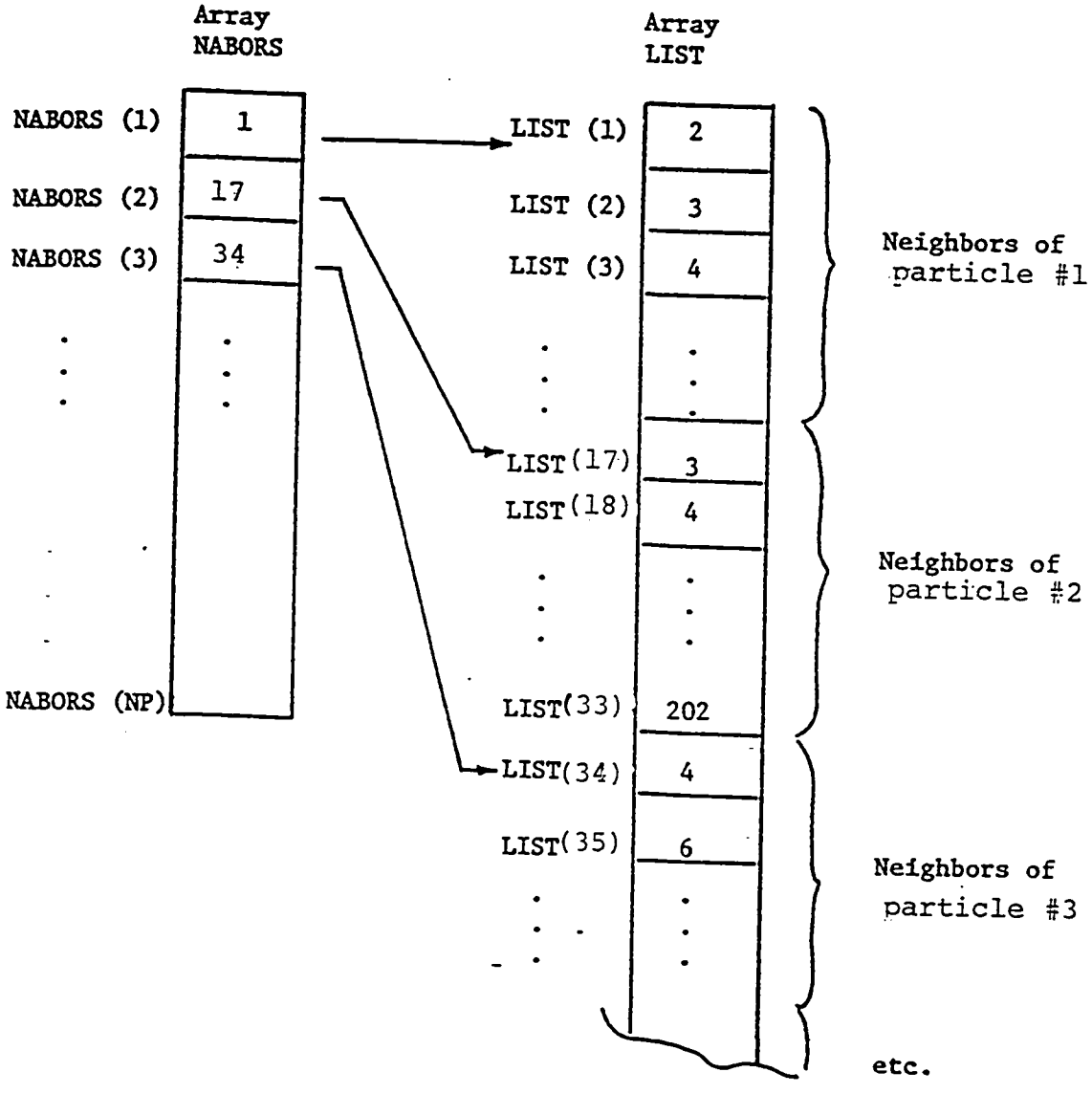

Fig. 3.3 Use of two one-dimensional arrays to store neighbor-list for each particle.

large repulsive force which often leads to numerical failure of the predictor-corrector algorithm.

Since the Lennard-Jones fluid can properly describe simple fluids such as argon and because the three-dimensional argon crystal has a face-centered cubic structure, the simulations of Lennard-Jones fluids are typically started from a face-centered cubic lattice. In our study, a triangular lattice structure is used to start up the simulation of two-dimensional Lennard-Jones fluids. Fig. 3.4 gives an example of the triangular lattice structure. It is kept in mind that while crystals with short-ranged forces do not exist in two dimensions at the thermodynamic limit,[46] periodic triangular structures are stable in finite two-dimensional systems.

Initial velocities $\mathbf{v}_i(0)(=\mathbf{r}_i^{(1)}(0))$ may be randomly assigned or they may be taken from a previous simulation. For randomly assigned velocities, the Cartesian components of the initial velocities $\mathbf{v}_i(0)$ are assigned by

$$v_{ix}(0) = \sqrt{\frac{3kT}{\varepsilon}} \frac{\cdot\xi_x}{\sqrt{\xi_x^2 + \xi_y^2 + \xi_z^2}}, \tag{3.21}$$

$$v_{iy}(0) = \sqrt{\frac{3kT}{\varepsilon}} \frac{\cdot\xi_y}{\sqrt{\xi_x^2 + \xi_y^2 + \xi_z^2}}, \tag{3.22}$$

$$v_{iz}(0) = \sqrt{\frac{3kT}{\varepsilon}} \frac{\cdot\xi_z}{\sqrt{\xi_x^2 + \xi_y^2 + \xi_z^2}}, \tag{3.23}$$

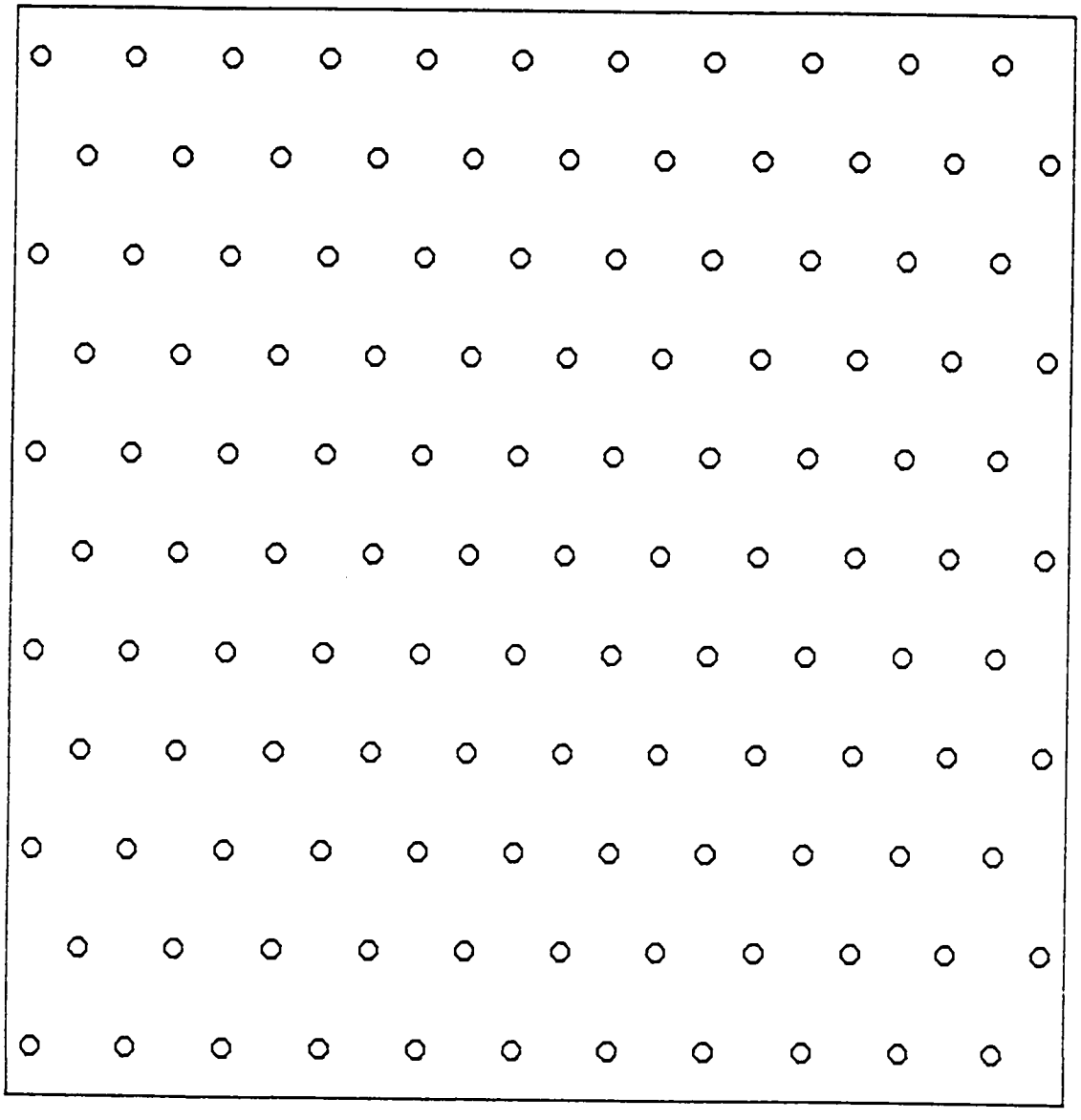

Fig. 3.4 Triangular lattice structure used to initiate the simulation for a two-dimensional Lennard-Jones fluid of 121 particles.

where ξ_x, ξ_y, and ξ_z represent three random numbers taken from a uniform distribution over the interval (-1,+1) and the prefactor $\sqrt{\frac{3kT}{\varepsilon}}$ is used to give the desired temperature.

To ensure that the total linear momentum of the N particles is zero, the initial velocities, obtained from (3.22), have to be adjusted according to

$$v_{ix}^{new}(0) = v_{ix}(0) - \frac{1}{N}\sum_i v_{ix}(0) \quad , \tag{3.24}$$

with similar adjustments for $v_{iy}(0)$ and $v_{iy}(0)$.

The initial values of the accelerations $\mathbf{a}_i(0)(=\mathbf{r}_i^{(2)}(0))$ can be determined from the initial position $\mathbf{r}_i(0)$ by using eqn. (3.16) with $\mathbf{r}_i^{(2)}=\mathbf{F}_i/m$. At t=0, therefore, we have the values for $\mathbf{r}_i(0)$, $\mathbf{r}_i^{(1)}(0)$, and $\mathbf{r}_i^{(2)}(0)$. However, there is no simple way to obtain the initial values for the higher derivatives of $\mathbf{r}_i(0)$, so we usually set

$$\mathbf{r}_i^{(3)}(0) = \mathbf{r}_i^{(4)}(0) = \mathbf{r}_i^{(5)}(0) = 0 \quad . \tag{3.25}$$

With these initial conditions, the trajectories of the particles have some deviations for the first few time steps because of the insufficient information on the higher derivatives of $\mathbf{r}_i(0)$. However, in 10-20 time steps the predictor-corrector algorithm adjusts itself to the correct trajectory.

3.2.6 Equilibration

During the first few thousand time steps of the simulation, the system relaxes from its initial state to its equilibrium state. If the system is undisturbed during this time period, the $\mathbf{r}_i$ and $\mathbf{v}_i$ rearrange themselves to equilibrium values consistent with the constant total energy E. Hence, the temperature of the system will usually drift from the desired value. To maintain the desired temperature T_D, energy is artificially added to or removed from the system by rescaling the molecular velocities at each time step while the system is approaching equilibrium. The new velocities can be obtained from

$$v_{ix}^{new}(t) = v_{ix}(t)\sqrt{\frac{T_D}{T_a}}, \tag{3.26}$$

where T_D is the desired temperature and T_a is the actual temperature at time t. A scaling procedure similar to (3.26) is also performed on the $v_{iy}(t)$ and $v_{iz}(t)$.

Equilibration usually requires a few hundred to few thousand time steps, depending on the initial values of $\mathbf{r}_i(0)$ and $\mathbf{v}_i(0)$ and on the desired thermodynamic state condition (V, T). When a bulk phase simulation is started from a face-centered cubic structure, the commonly used criterion for terminating equilibration is to check whether the mean-squared displacement of the particles,

$$< \Delta r^2 > = \frac{1}{N} \sum_i | \mathbf{r}_i(t) - \mathbf{r}_i(0) |^2 , \qquad (3.27)$$

exceed a certain prescribed value.

When the mean-squared displacement exceeds its prescribed value, we consider that the equilibration has already been reached and we cease the scaling of the velocities. This abrupt termination of the velocity scaling (3.26) imparts a small but discernable shock to the system. This shock dissipates in 30-50 time steps but is sufficient to shift the final average temperature at some value slightly different from the desired value T_D. Since the system is not at equilibrium during equilibration, all the dynamic history of equilibration should not be used to calculate any properties.

After the equilibration period, we can start to collect the data needed to compute the properties of interest.

3.3 SIMULATION OF A TWO-DIMENSIONAL VAPOR-LIQUID PHASE EQUILIBRIUM

We study a vapor-liquid phase equilibrium system of 242 particles confined in a rectangular cell 13.055σX52.218σ. The particles interact via a truncated Lennard-Jones pair potential given by eqn. (3.14), in which the length and energy parameters are chosen to be σ = 3.405 Å and $\frac{\varepsilon}{k}$ = 119.86 K, which are the currently accepted values for argon. The values of the cut-off distance r_c and the list distance r_L are taken to be 3σ and 3.5σ, respectively. The time increment Δt used in the predictor-corrector algorithm is chosen to be $0.004\sigma\sqrt{m/\varepsilon}$.

The initial slab configuration is set up according to the procedure used by Lee, Barker and Pound[35a]. A bulk liquid simulation of 121 particles at the desired temperature is performed, starting from a triangular lattice, as shown in Fig. 3.4, in a cell of height L_z^B and width L_x^B. L_x^B is fixed to 13.055σ at different temperatures to ensure a constant interfacial area. L_z^B is chosen such that the bulk density of the liquid phase corresponds to the coexisting liquid density at the desired temperature, as obtained from the coexistence curve of Barker, Henderson and Abraham[47]. Periodic boundary conditions are imposed in both the x and z directions. The equilibration of the liquid slab is conducted for $5x10^3$-10^4 time steps and a velocity scaling is performed at each time step to maintain the desired temperature.

The equilibrated bulk liquid configuration is then duplicated in the vertical, z-direction, and placed at the center of a cell of height $L_z(=52.218\sigma)$ and width $L_x(=13.055\sigma)$, as shown in Fig. 3.5. The simulation cell thus has two vapor-liquid interfaces, and initially there are no particles in either vapor slabs. Periodic boundary conditions are also imposed in both x and z directions.

The equilibration of the two-fluid phase system is continued for $5x10^4$-$2x10^5$ time steps until the large interfacial fluctuations, caused by a large bubble being driven out of the liquid, have relaxed to equilibrium. However, the bubble is sometimes so large that it might break the liquid phase into two pieces, forcing us to discard the run and restart a new one.

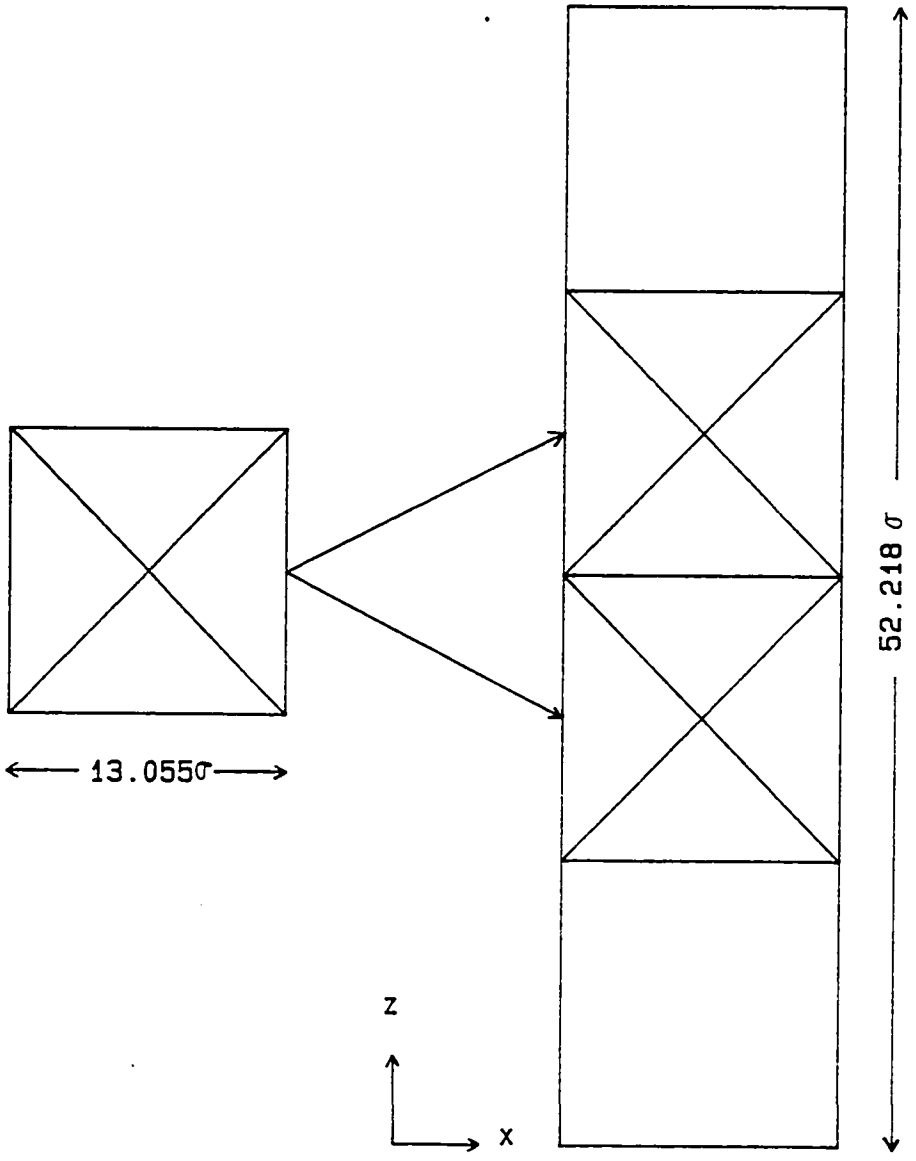

Fig. 3.5 Schematic illustration of the construction of the vapor-liquid interface from the equilibrated bulk liquid slab shown to the left.

After the equilibration period, 10^4-$2x10^4$ more time steps are used to absorb the shock due to the abrupt termination of the velocity scaling. The data of interest are collected thereafter.

The density profile is computed as the time average of the number of particles in a strip of width Δz centered at z and parallel to the x-axis. The value of the strip width Δz must be chosen small enough so that the discretization of the system is a good approximation, but large enough in order to obtain good statistical accuracy. In the present study, Δz is chosen to be $\frac{L_z}{200}$ in all the calculations. Usually, the density profile is obtained by averaging over $1x10^5$-$3x10^5$ time steps after equilibration. During the period in which data are collected, the energy fluctuations are always less than 0.2% of the total energy, which is extremely stable. There are some fluctuations in the density profile due to an insufficient averaging and these could be smoothed out over a longer period of time. As Fig. 3.6 illustrates: the longer the run, the smoother the profile.

Once the density profile is obtained, the bulk phase densities can be obtained by averaging over the fluctuations in the bulk phases. If we use eqn. (2.22) to determine the interfacial thickness, we must choose a function for the density profile in order to perform the curve fitting and obtain the density gradient $d\rho/dz$. To minimize the uncertainty of the exact function describing the density profile, we use the 10-90 rule[48], in which the interfacial thickness is taken to be equal to the distance between the values $\rho_v+0.1(\rho_l-\rho_v)$ and $\rho_v+0.9(\rho_l-\rho_v)$. This 10-90 thickness is less sensitive to the exact shape of the density profile than that of eqn. (2.22).

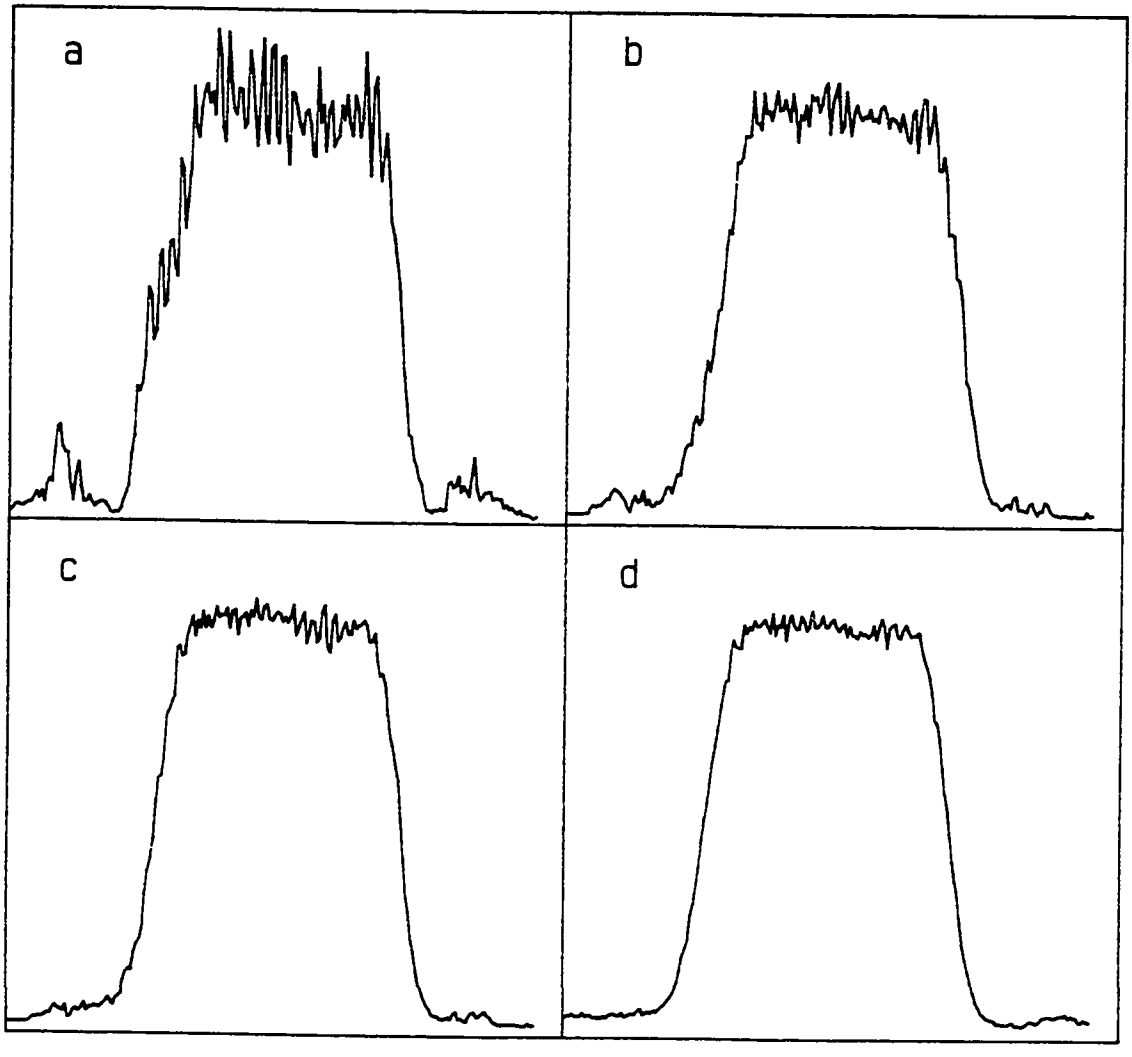

Fig. 3.6 Density profiles for a Lennard-Jones fluid at T*=0.433 obtained by averaging over (a) 10,000, (b) 50,000, (c) 100,000, and (d) 300,000 time steps. Averaging over more time steps is clearly seen to reduce the scatter in the data.

3.4 RESULTS AND DISCUSSION

In order to study the variation of the thickness of the interface as a function of temperature, we have performed simulations at nine different temperatures. The statistical averages for the bulk phases and the interfacial thickness are summarized in Table 3.2, where $T^*=kT/\varepsilon$ and $\rho^*=\rho\sigma^2$.

The density profiles we have obtained are shown in Figs. 3.7 to 3.15, where the density along the y-axis is the dimensionless density ρ^*. Fig. 3.16 shows the temperature dependence of the interfacial thickness L, where the dimensionless temperature t is defined by (2.35) and $T_c^*=0.533$.[47] The error bars are based on the values of the interfacial thickness obtained from intermediate results (see Figs. 3.17 to 3.25), which are obtained by averaging over blocks of $4\text{x}10^4$ - 10^5 consecutive time steps.

In Fig. 3.16, the slope obtained by the least-squared regression method yields the critical exponent $\omega=0.91$, which is much closer to the prediction of the van der Waals theory ($\omega=1$) than to that of the capillary wave theory ($\omega=9/32$). On the other hand, within the statistical uncertainty, the interfacial thickness is seen to follow the prediction of the van der Waals theory quite well by drawing a line with slope=-1 through the point of $T^*=0.474$, as shown in Fig. 3.16. This agreement of our results with the prediction of the van der Waals theory supports the view that the suppression of long-wavelength capillary waves in a finite system yields an intrinsic interface with a thickness that varies with temperature like the bulk correlation length.

Table 3.2 Statistical averages for bulk phase densities and interfacial thickness.

T^{*} (a)	ρ_l^{*} (b)	ρ_v^{*} (b)	N (c)	$\frac{L}{\sigma}$
0.424	0.736	0.0334	$25x10^4$	4.56
0.433	0.724	0.0376	$30x10^4$	4.85
0.436	0.710	0.0427	$30x10^4$	4.68
0.441	0.710	0.0518	$30x10^4$	5.03
0.446	0.701	0.0458	$30x10^4$	5.39
0.456	0.686	0..0438	$12x10^4$	5.80
0.461	0.678	0.0610	$30x10^4$	6.67
0.468	0.674	0.0722	$30x10^4$	7.03
0.474	0.656	0.0801	$20x10^4$	7.70

a $T^{*}=\frac{kT}{\varepsilon}$,

b $\rho^{*}=\rho\sigma^2$,

c N= number of time steps used to calculate the interfacial thickness.

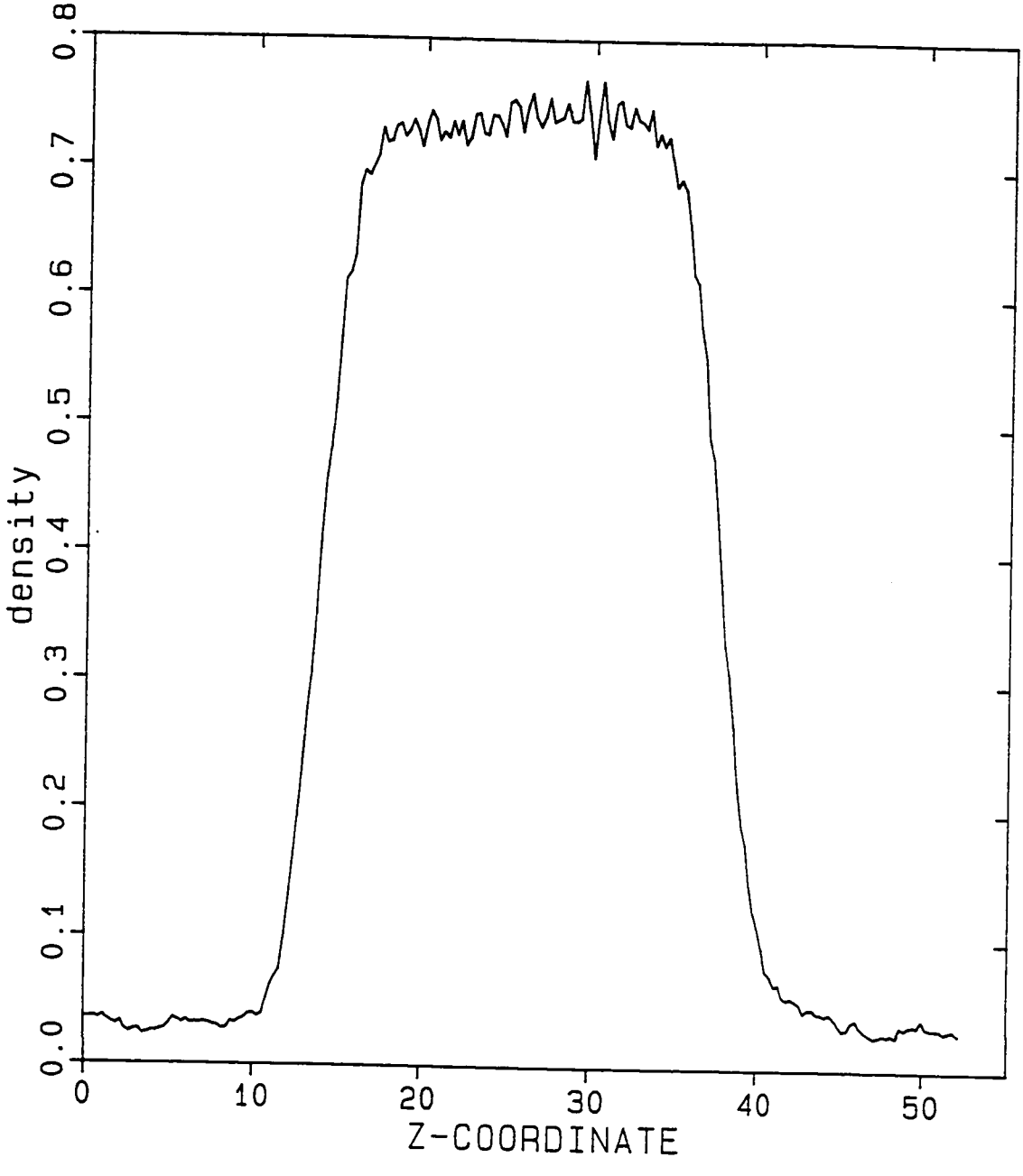

Fig. 3.7 Density profile of a two-dimensional Lennard-Jones fluid at T*=0.424 obtained by averaging over 250,000 time steps.

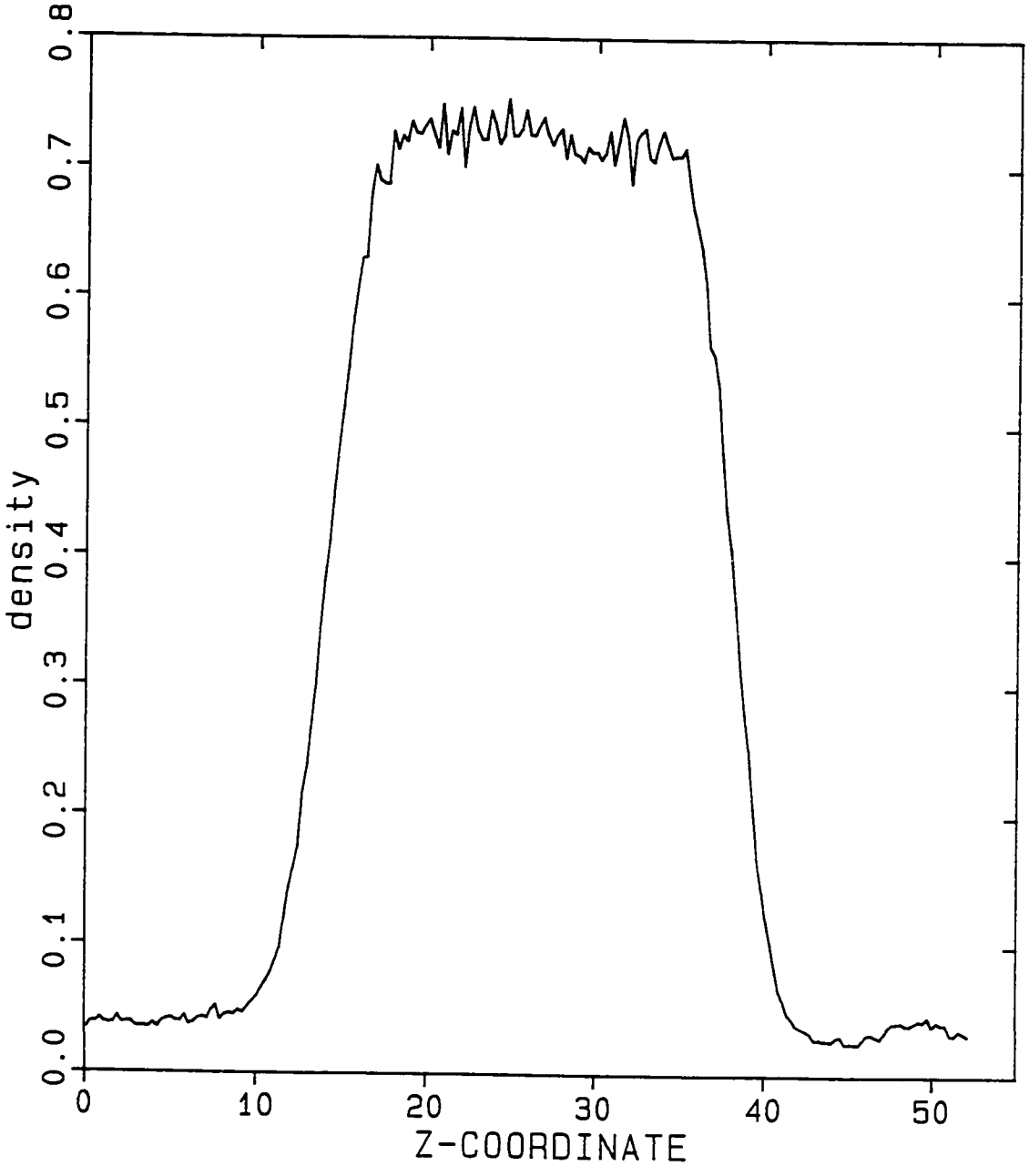

Fig. 3.8 Density profile of a two-dimensional Lennard-Jones fluid at T*=0.433 obtained by averaging over 300,000 time steps.

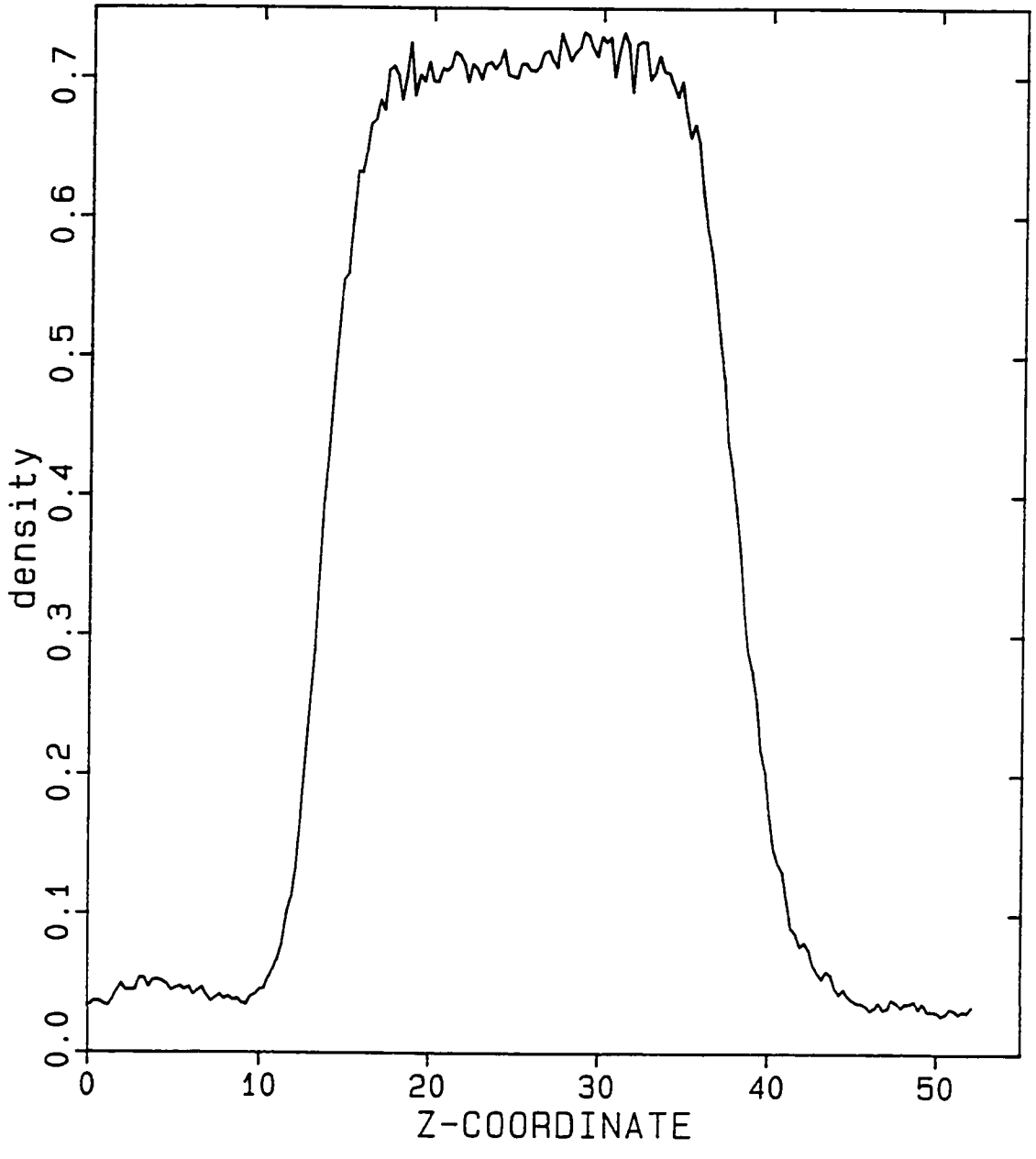

Fig. 3.9 Density profile of a two-dimensional Lennard-Jones fluid at T*=0.436 obtained of averaging over 300,000 time steps.

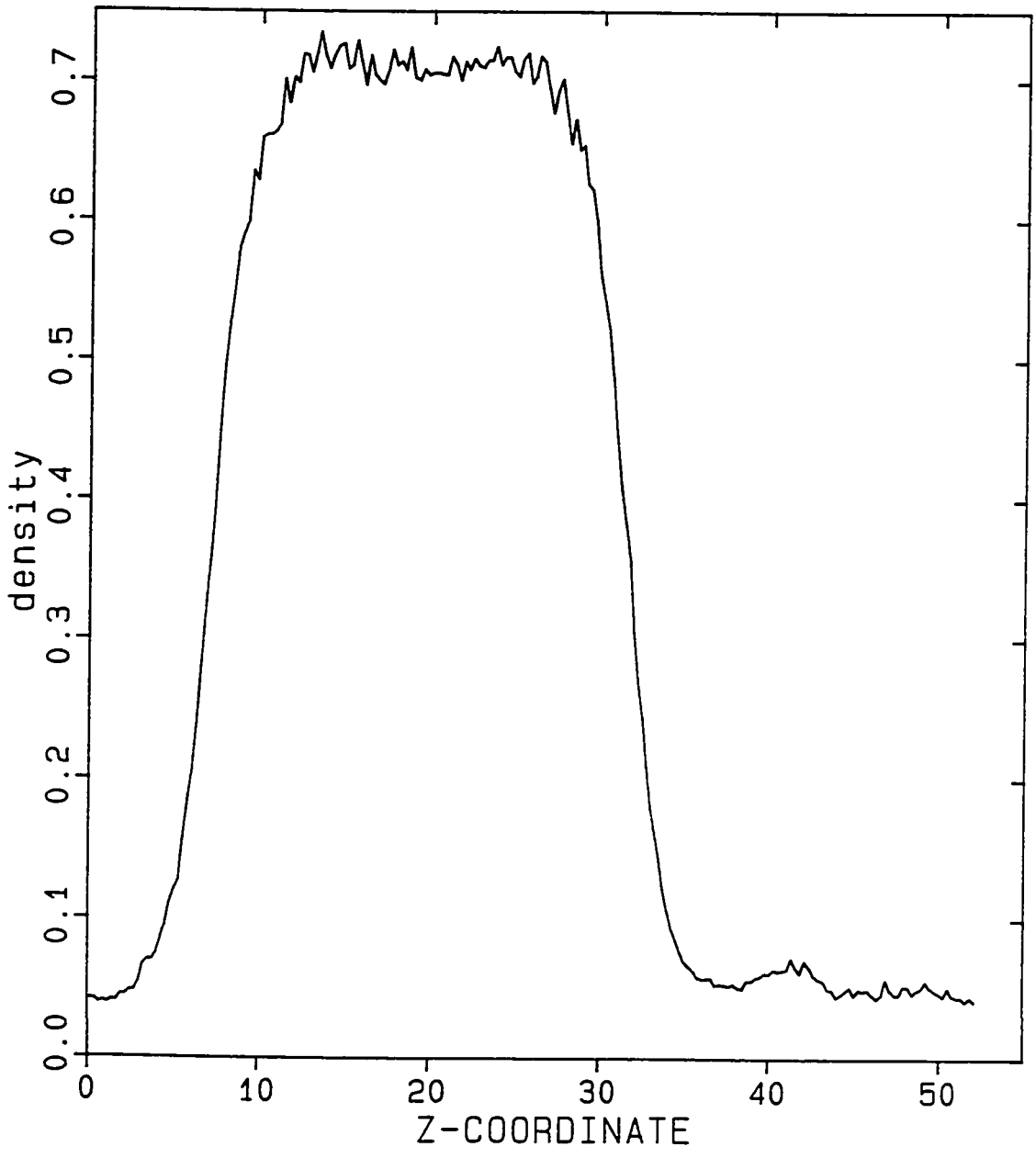

Fig. 3.10 Density profile of a two-dimensional Lennard-Jones fluid at T*=0.441 obtained by averaging over 300,000 time steps.

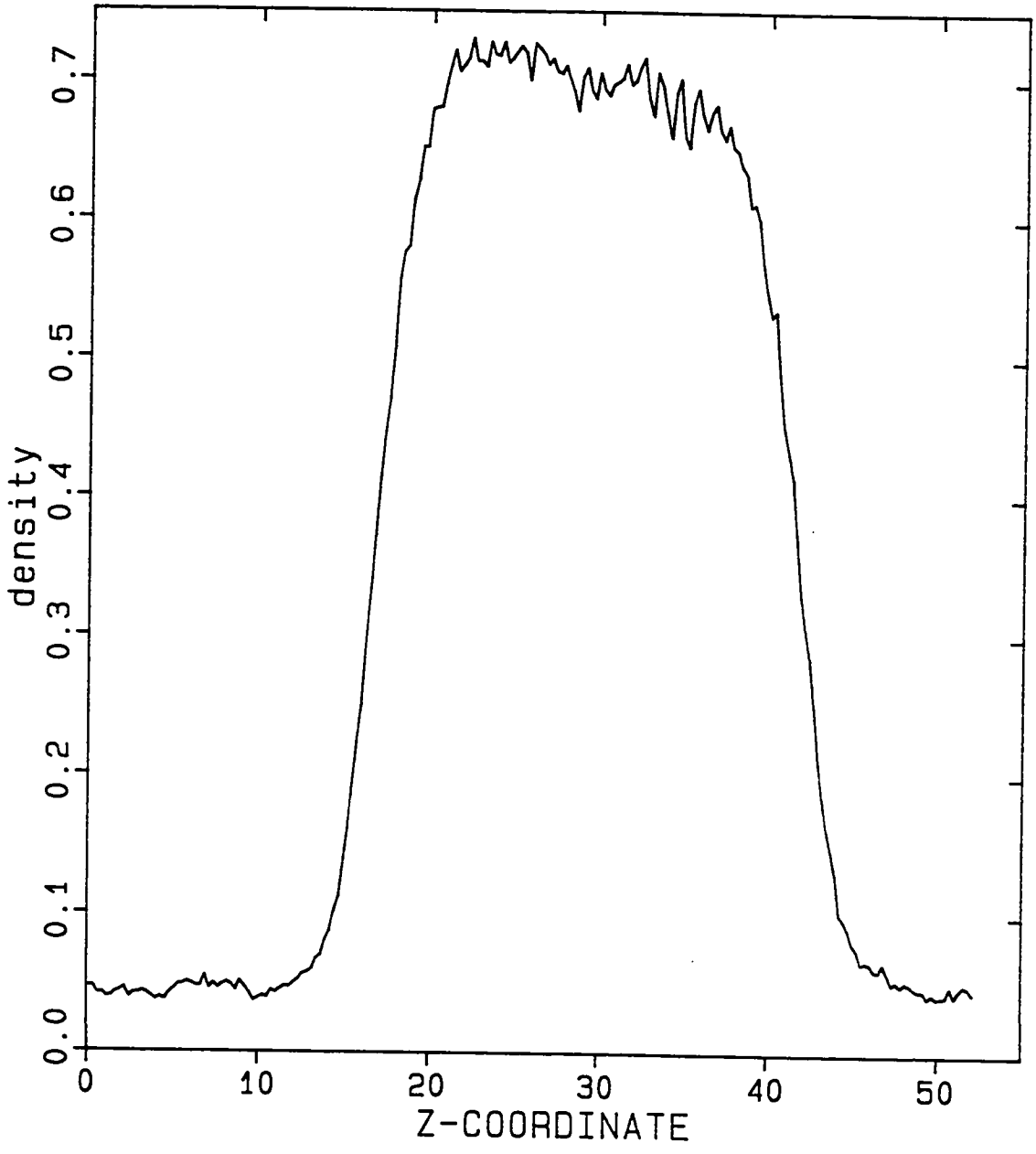

Fig. 3.11 Density profile of a two-dimensional Lennard-Jones fluid at T*=0.446 obtained by averaging over 300,000 time steps.

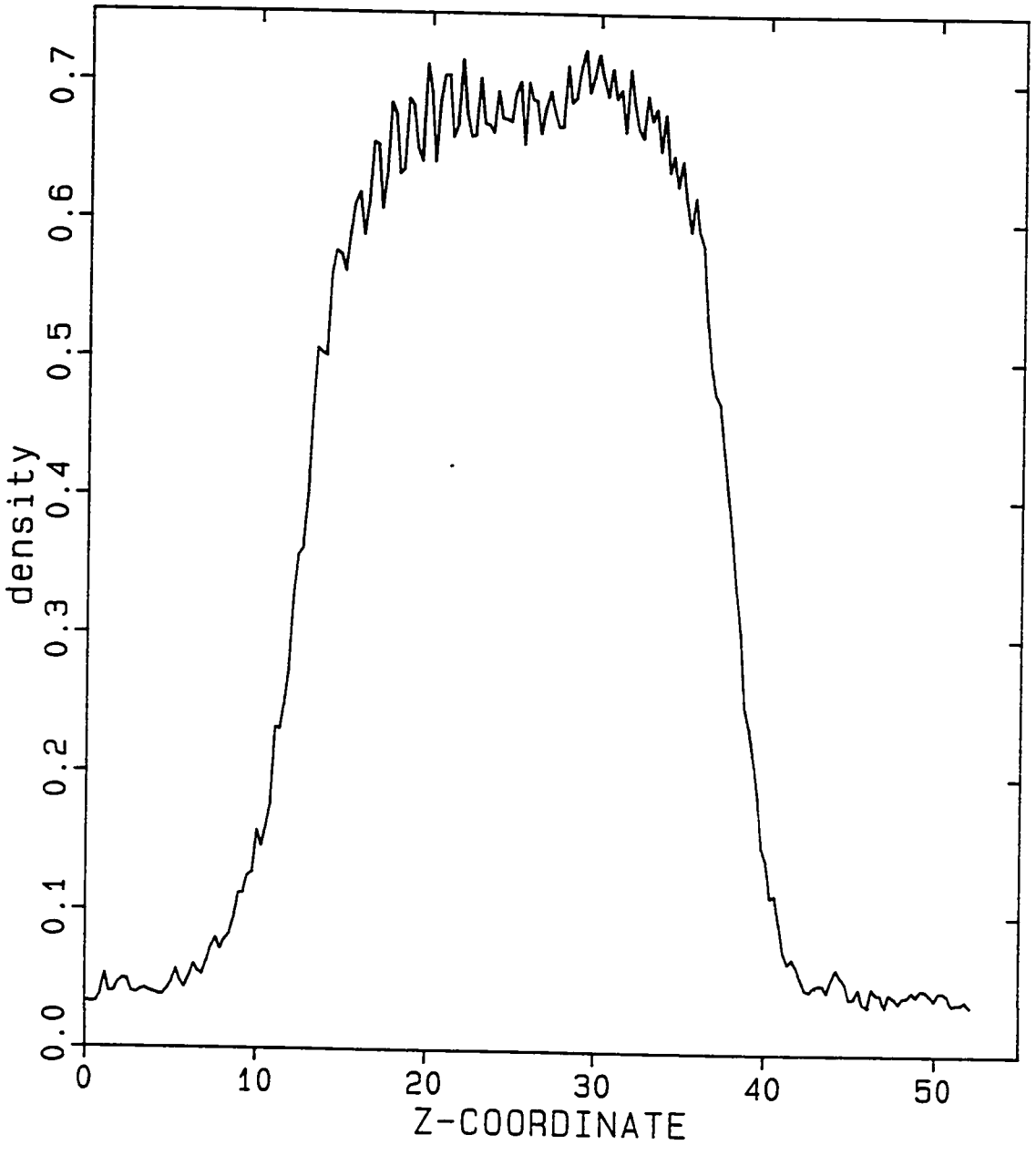

Fig. 3.12 Density profile of a two-dimensional Lennard-Jones fluid at T*=0.456 obtained by averaging over 120,000 time steps.

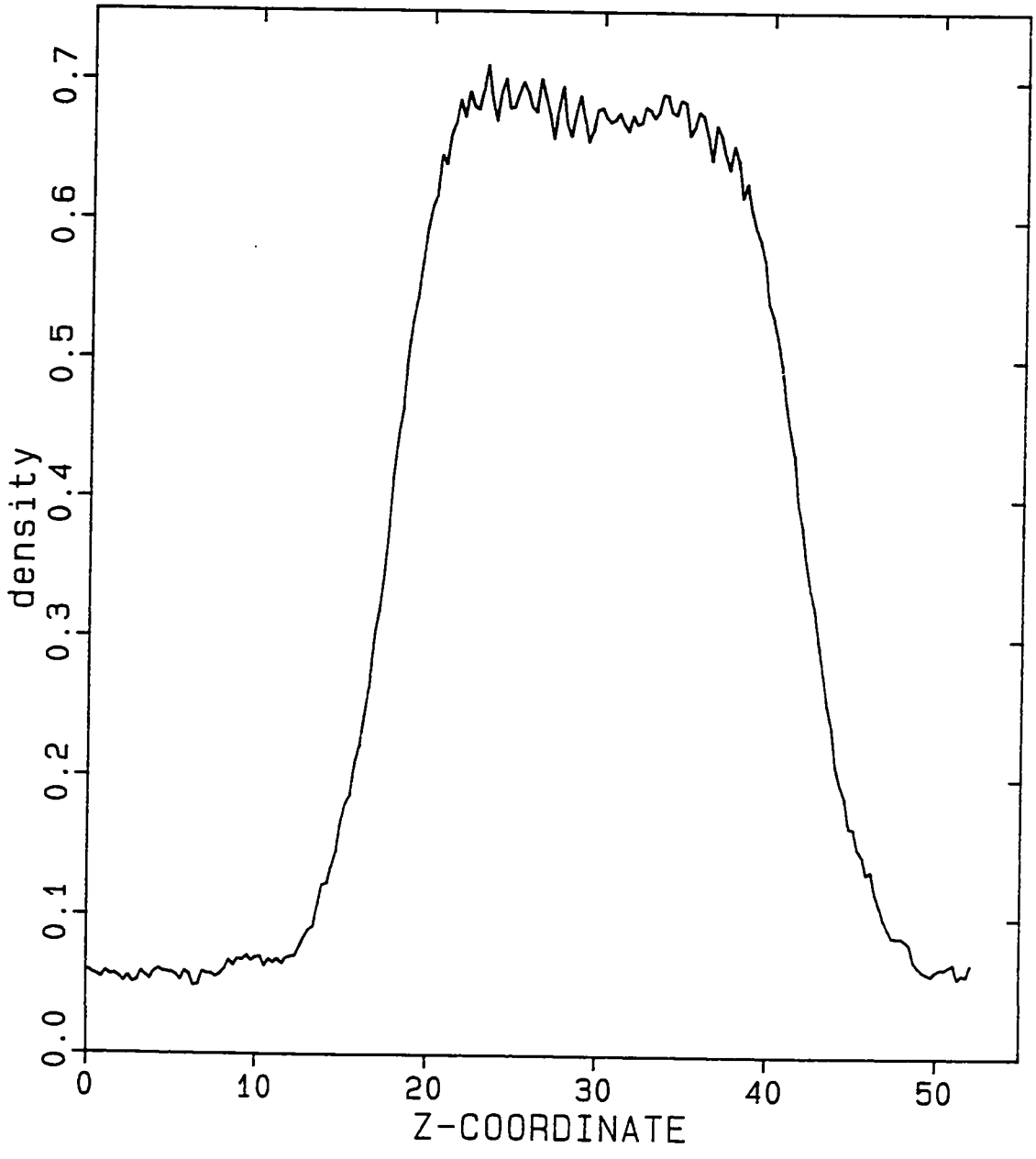

Fig. 3.13 Density profile of a two-dimensional Lennard-Jones fluid at T*=0.461 obtained by averaging over 300,000 time steps.

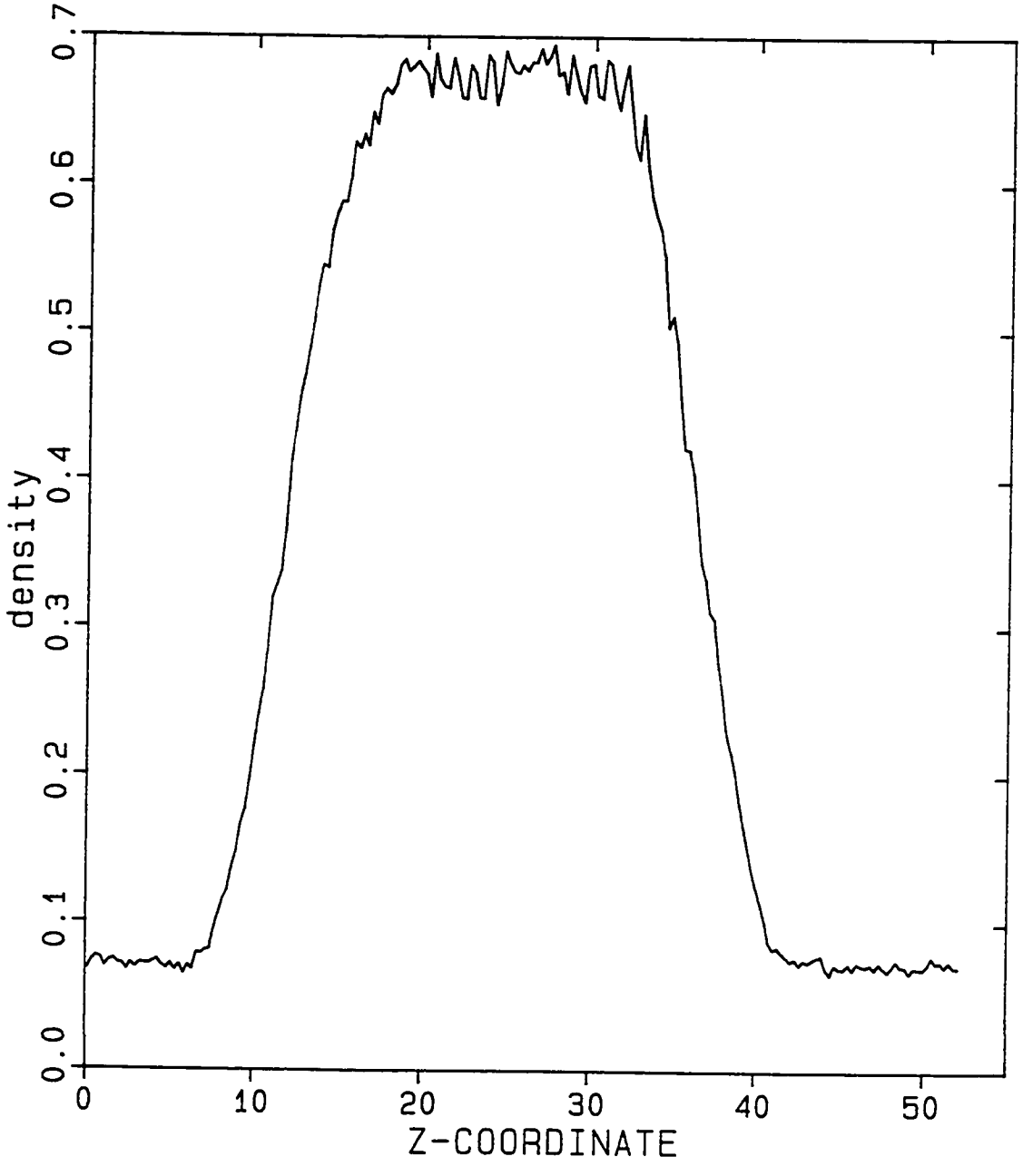

Fig. 3.14 Density profile of a two-dimensional Lennard-Jones fluid at T*=0.468 obtained by averaging over 300,000 time steps.

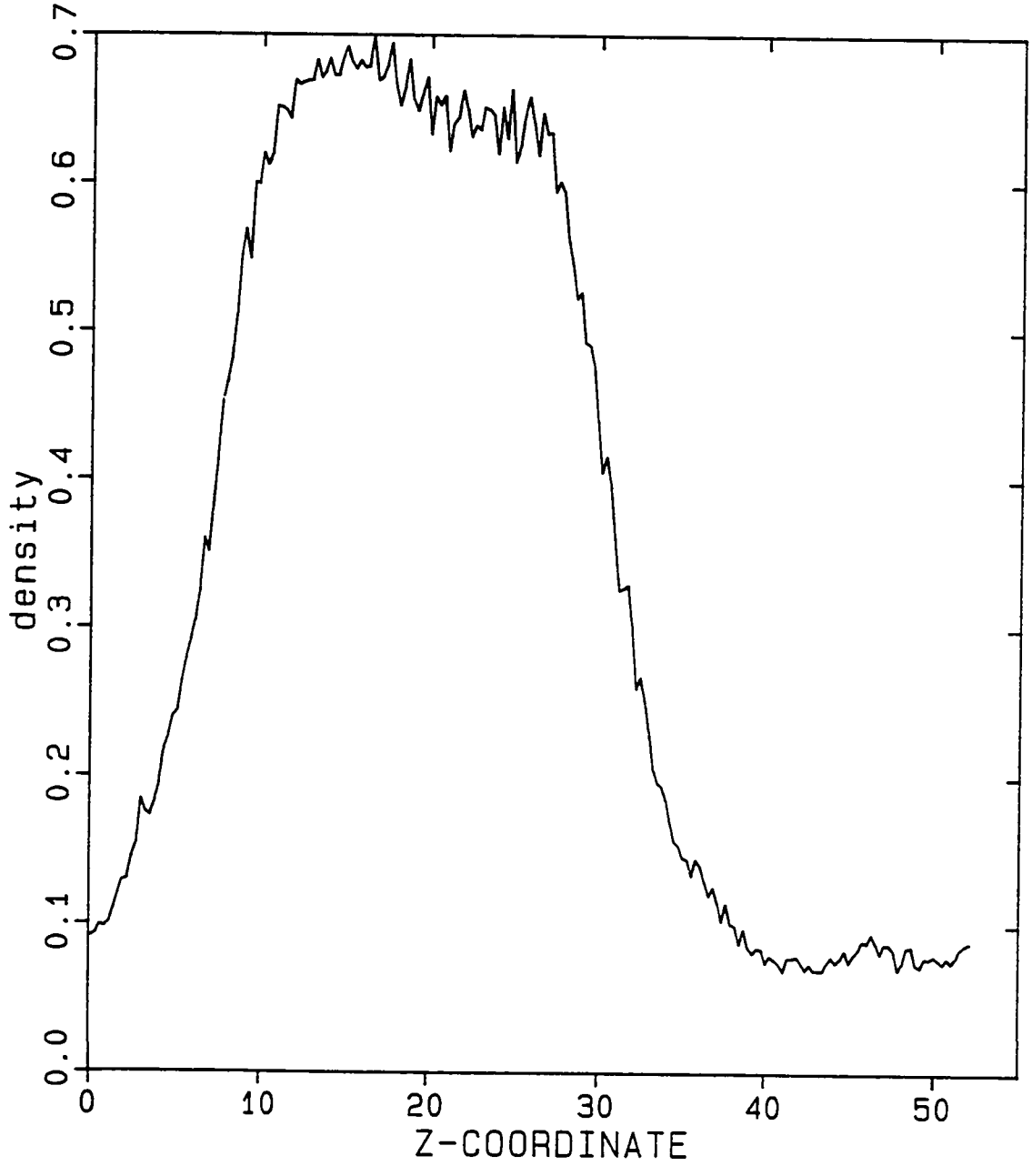

Fig. 3.15 Density profile of a two-dimensional Lennard-Jones fluid at T*=0.474 obtained by averaging over 200,000 time steps.

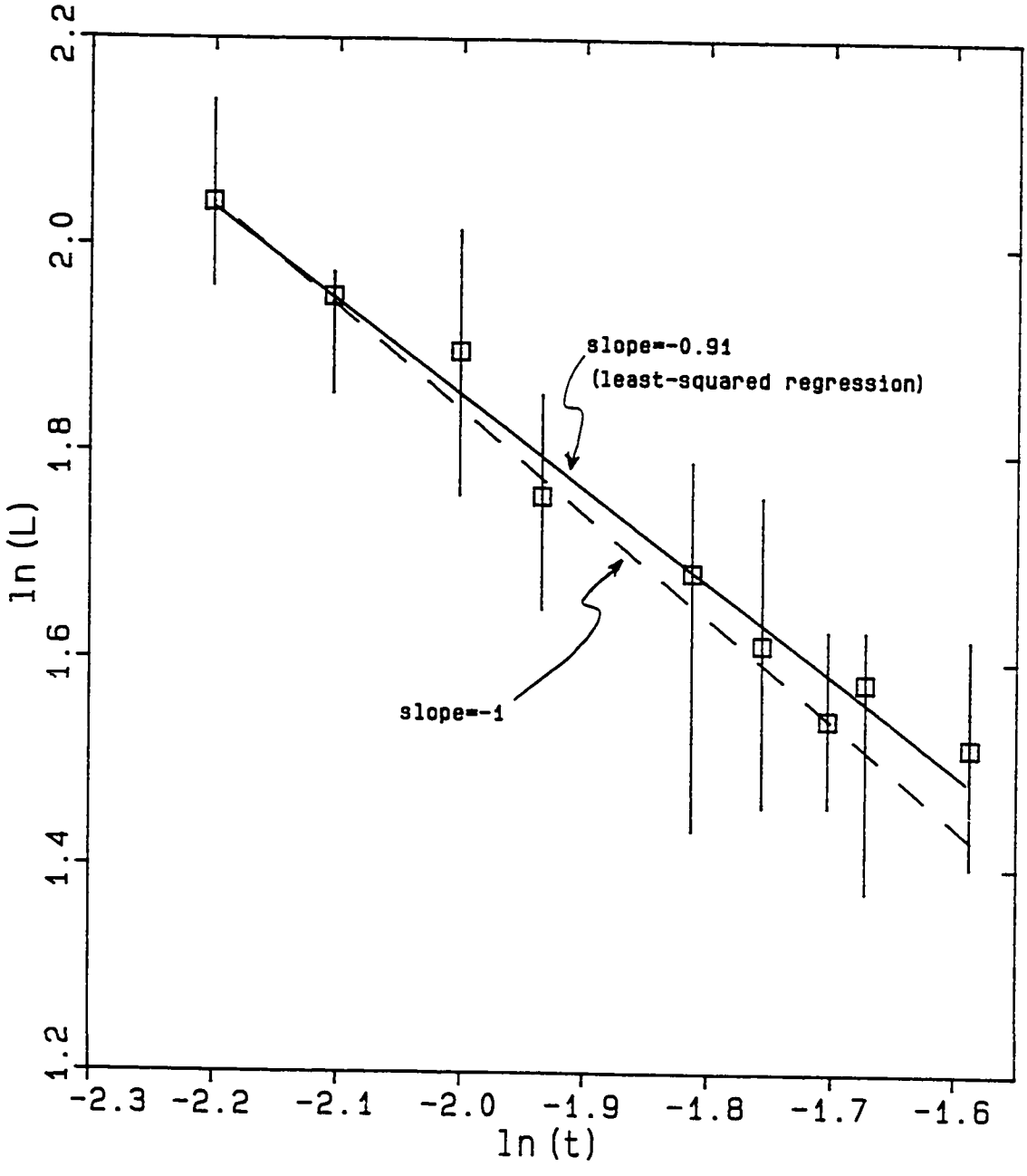

Fig. 3.16 Variation of the interfacial thickness L as a function of the dimensionless temperature t.

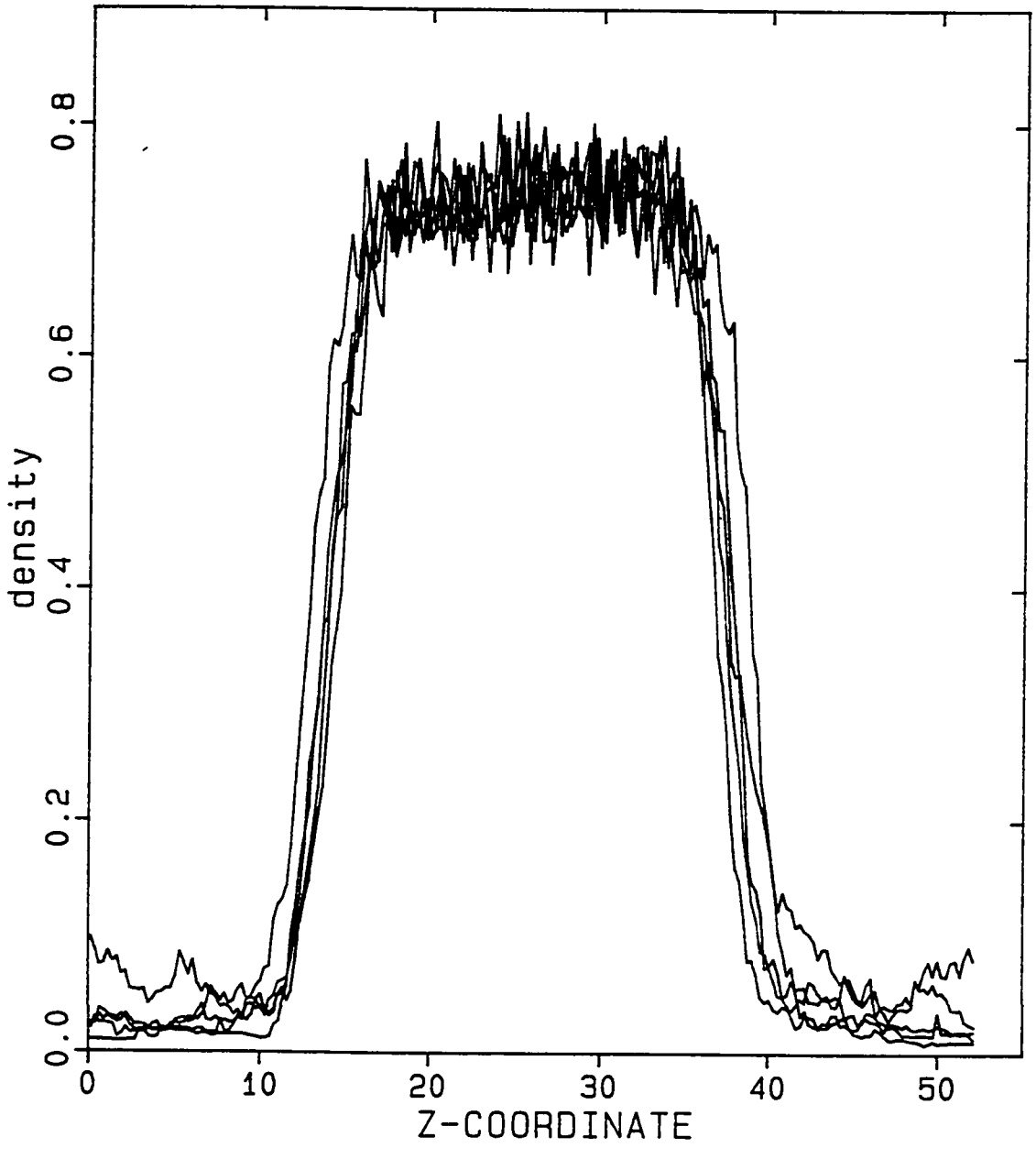

Fig. 3.17 Intermediate results for the density profile at T*=0.424. Each curve is obtained by averaging over 50,000 time steps.

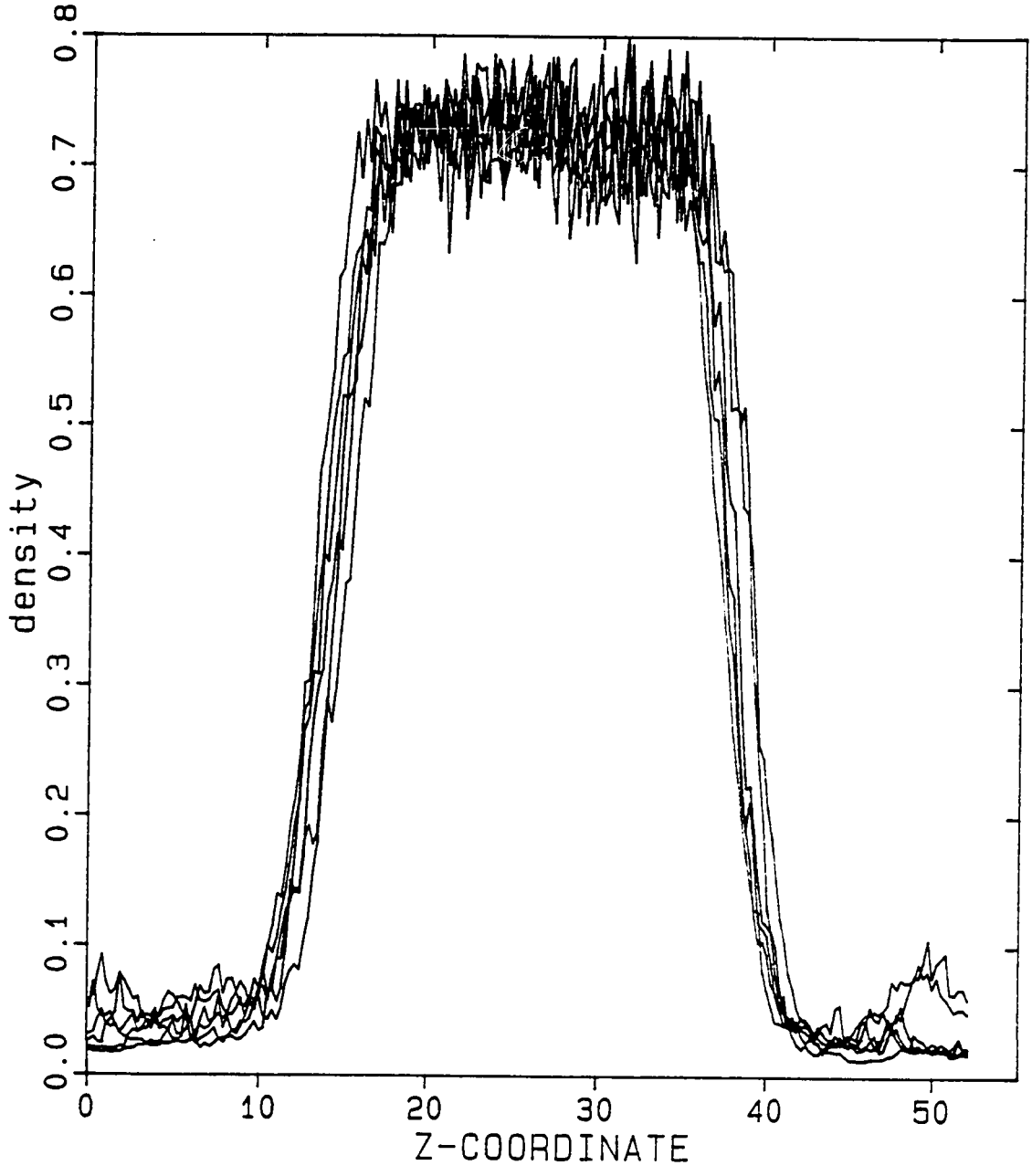

Fig. 3.18 Intermediate results for the density profile at T*=0.433. Each curve is obtained by averaging over 50,000 time steps.

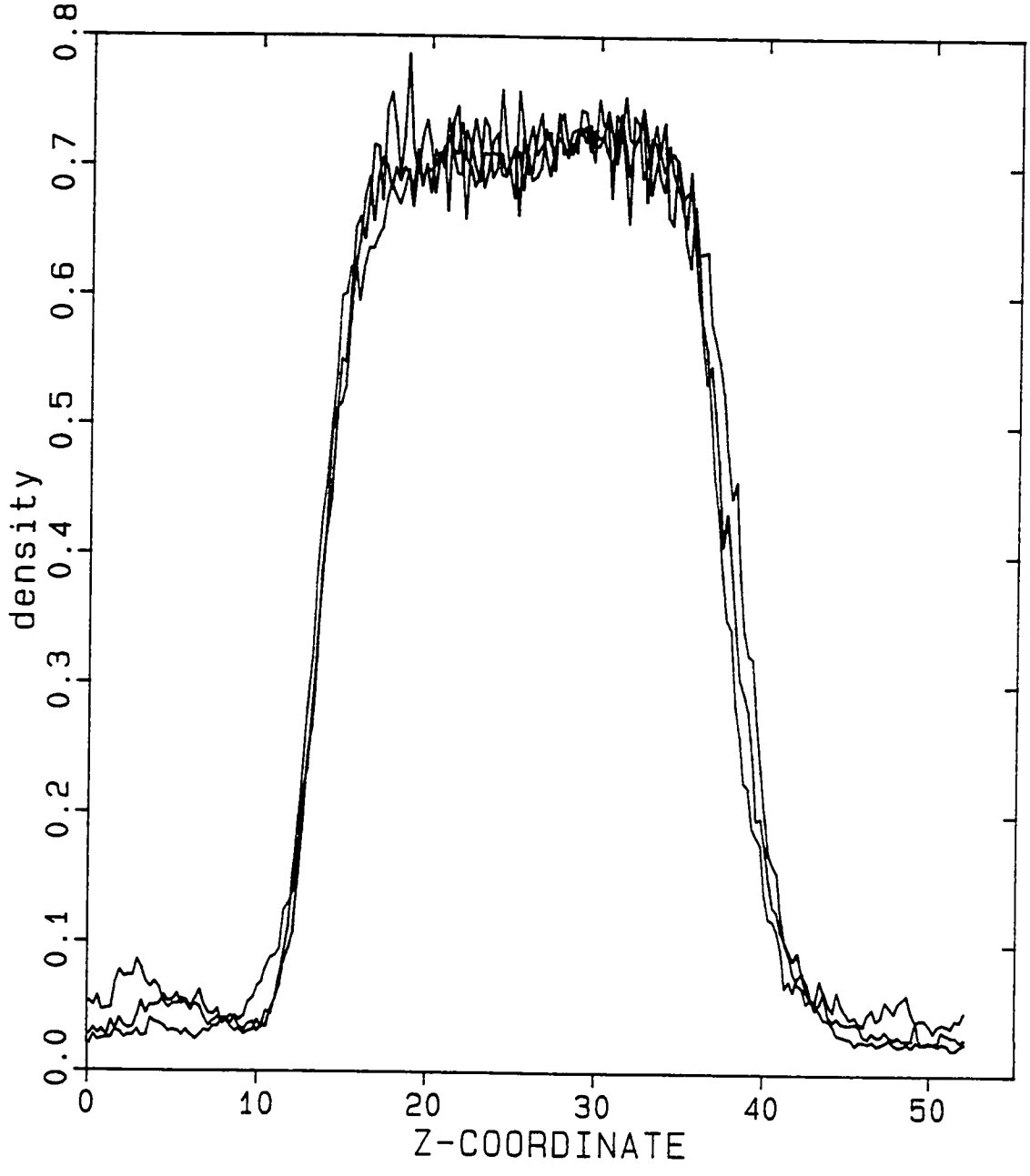

Fig. 3.19 Intermediate results for the density profile at T*=0.436. Each curve is obtained by averaging over 100,000 time steps.

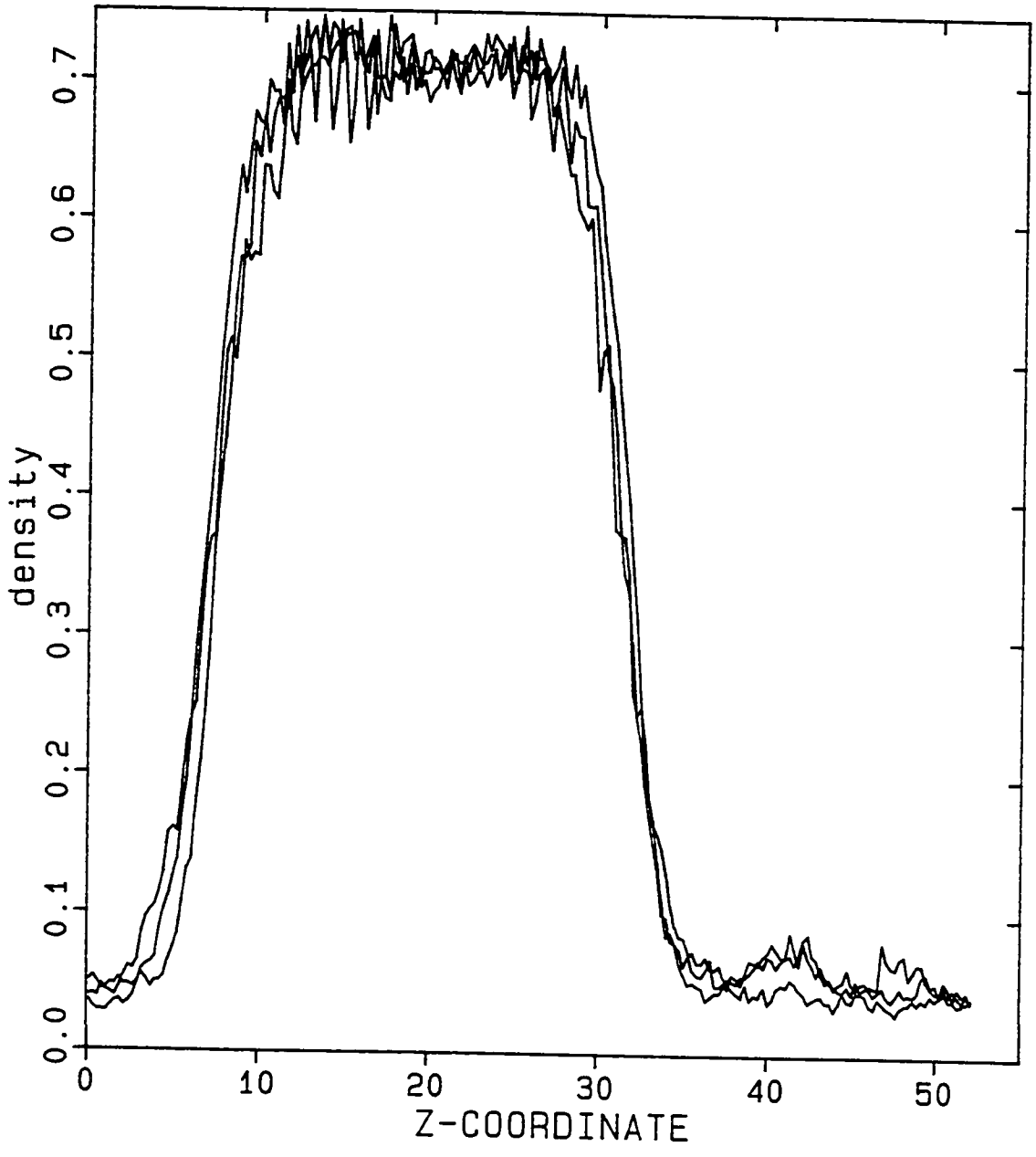

Fig. 3.20 Intermediate results for the density profile at T*=0.441. Each curve is obtained by averaging over 100,000 time steps.

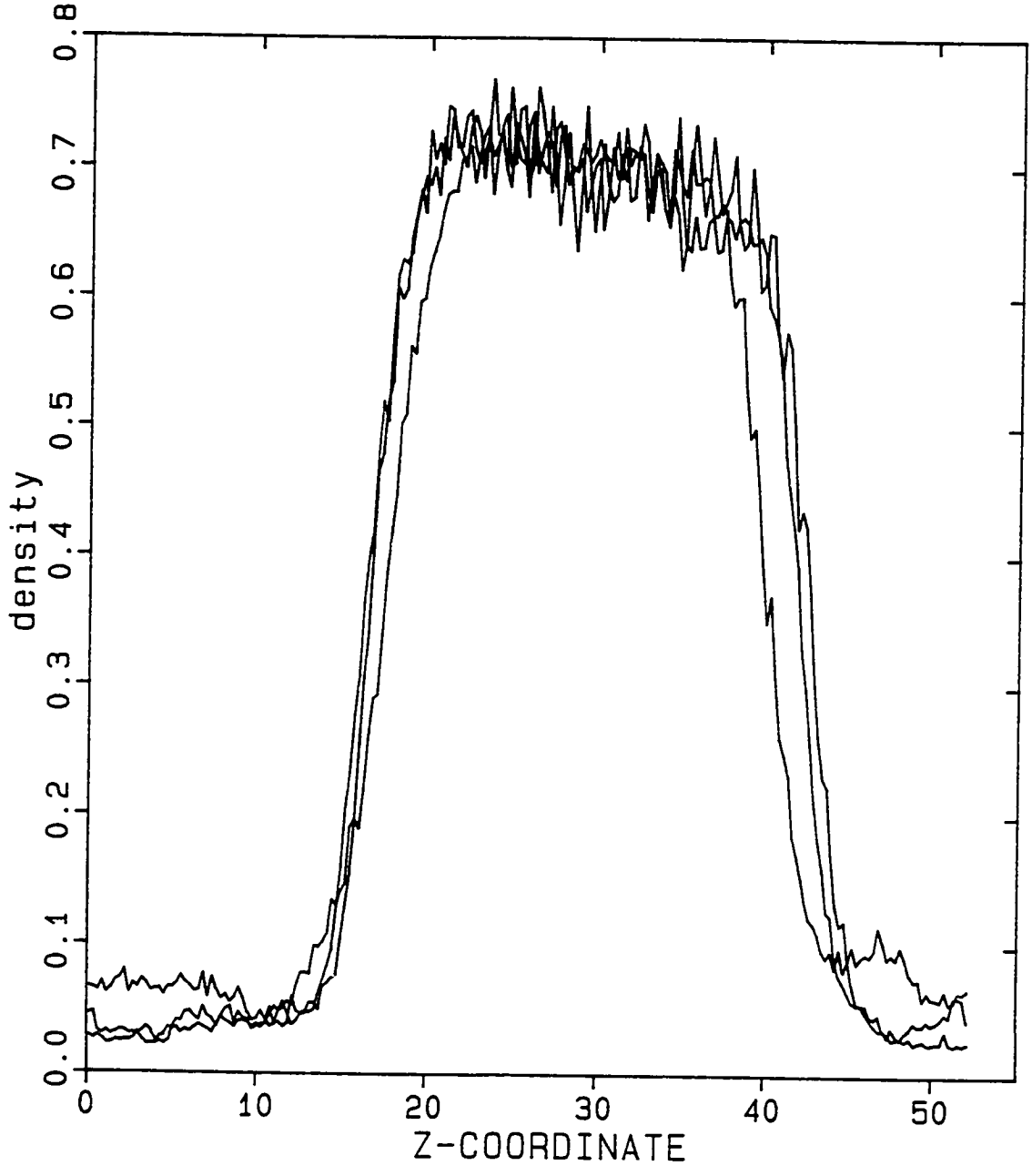

Fig. 3.21 Intermediate results for the density profile at T*=0.446. Each curve is obtained by averaging over 100,000 time steps.

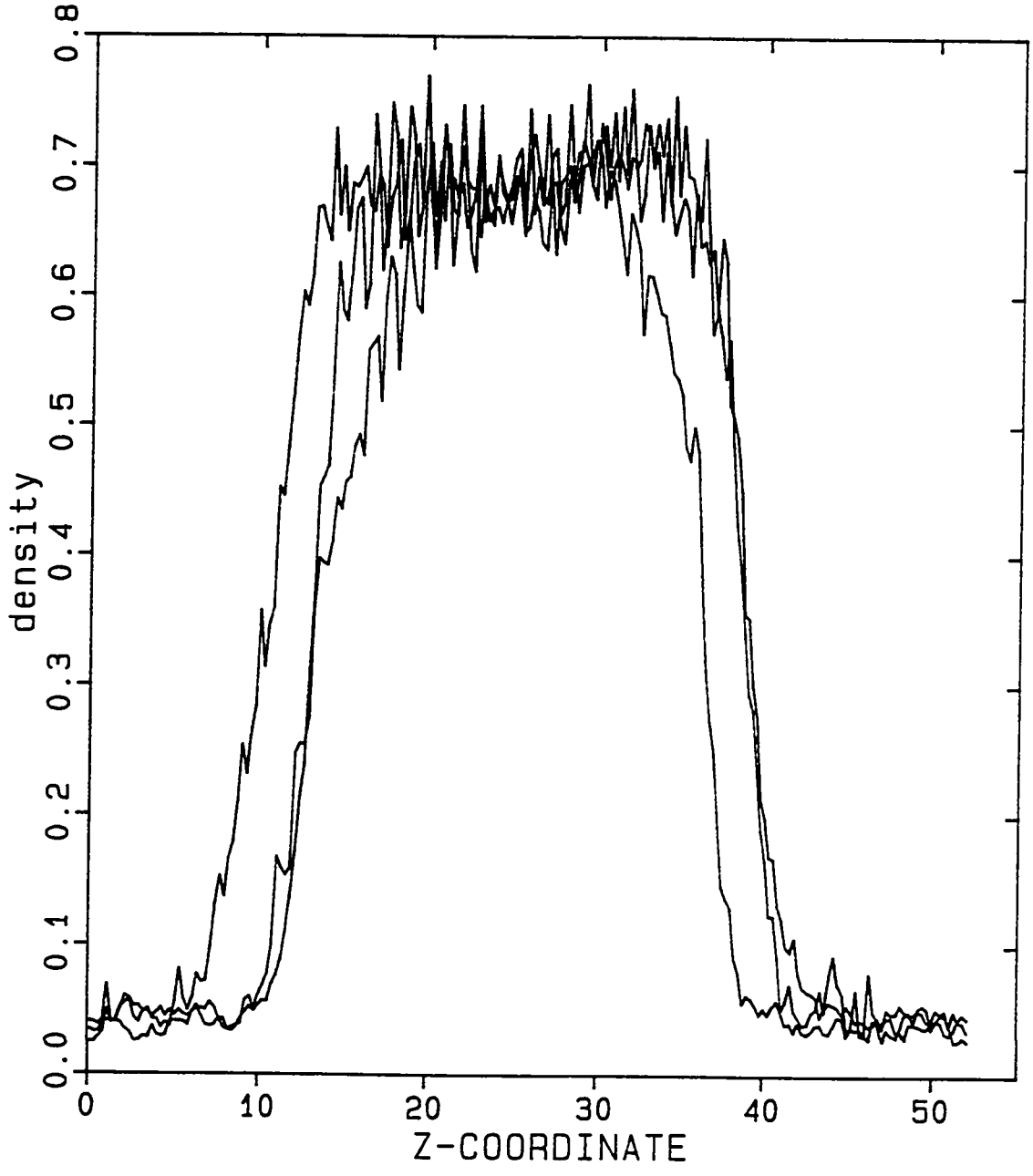

Fig. 3.22 Intermediate results for the density profile at T*=0.456. Each curve is obtained by averaging over 40,000 time steps.

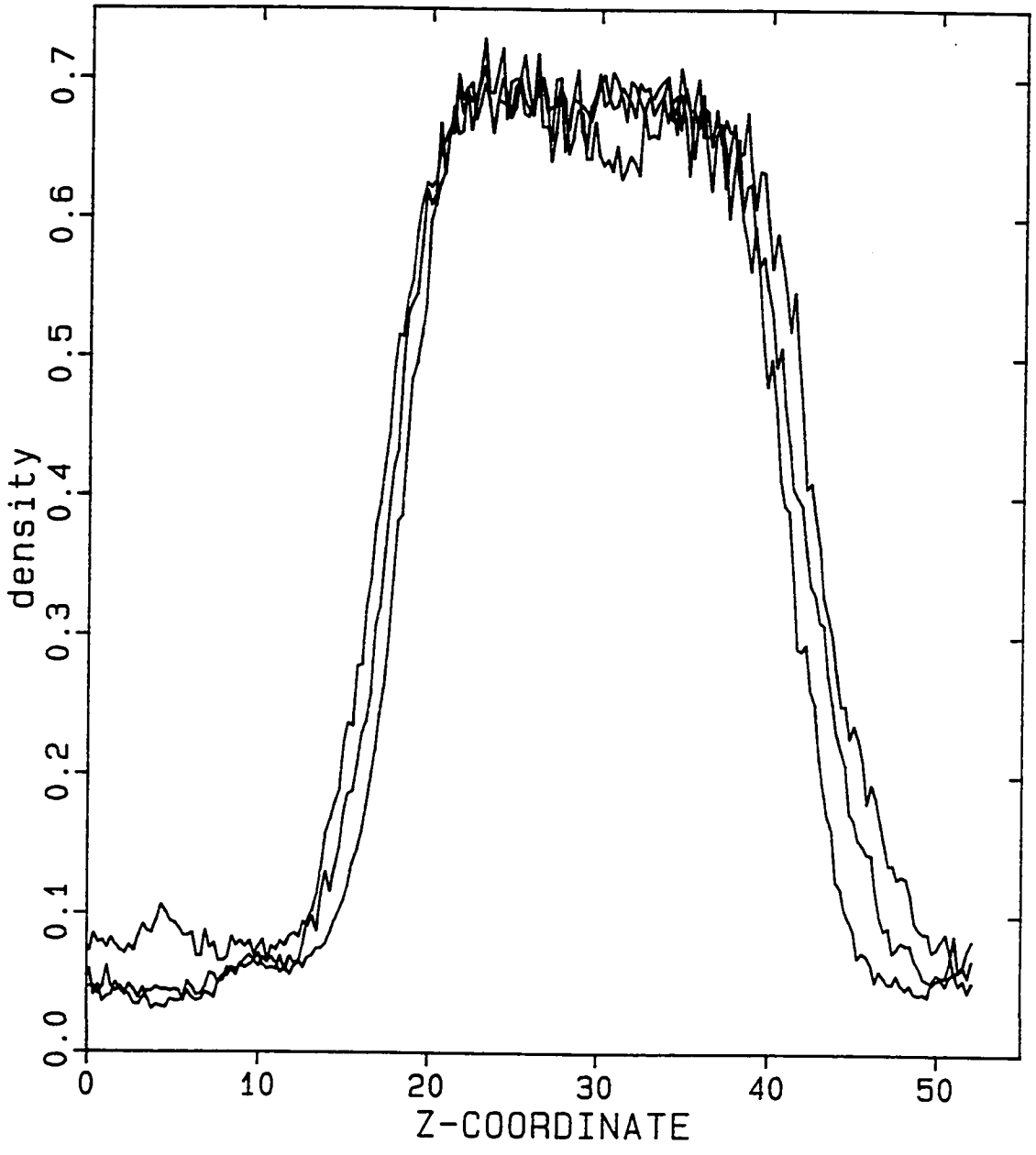

Fig. 3.23 Intermediate results for the density profile at T*=0.461. Each curve is obtained by averaging over 100,000 time steps.

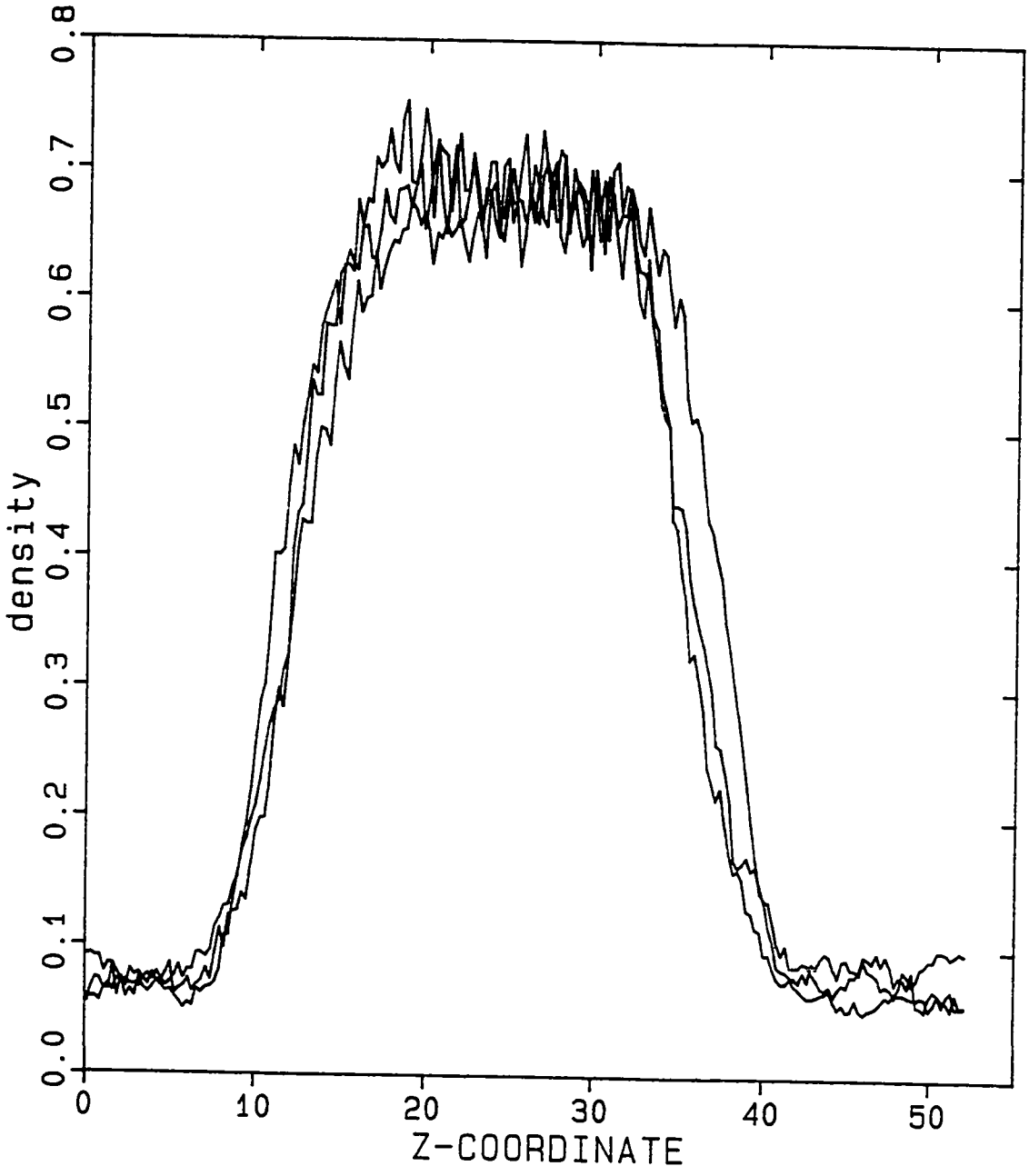

Fig. 3.24 Intermediate results for the density profile at T*=0.468. Each curve is obtained by averaging over 100,000 time steps.

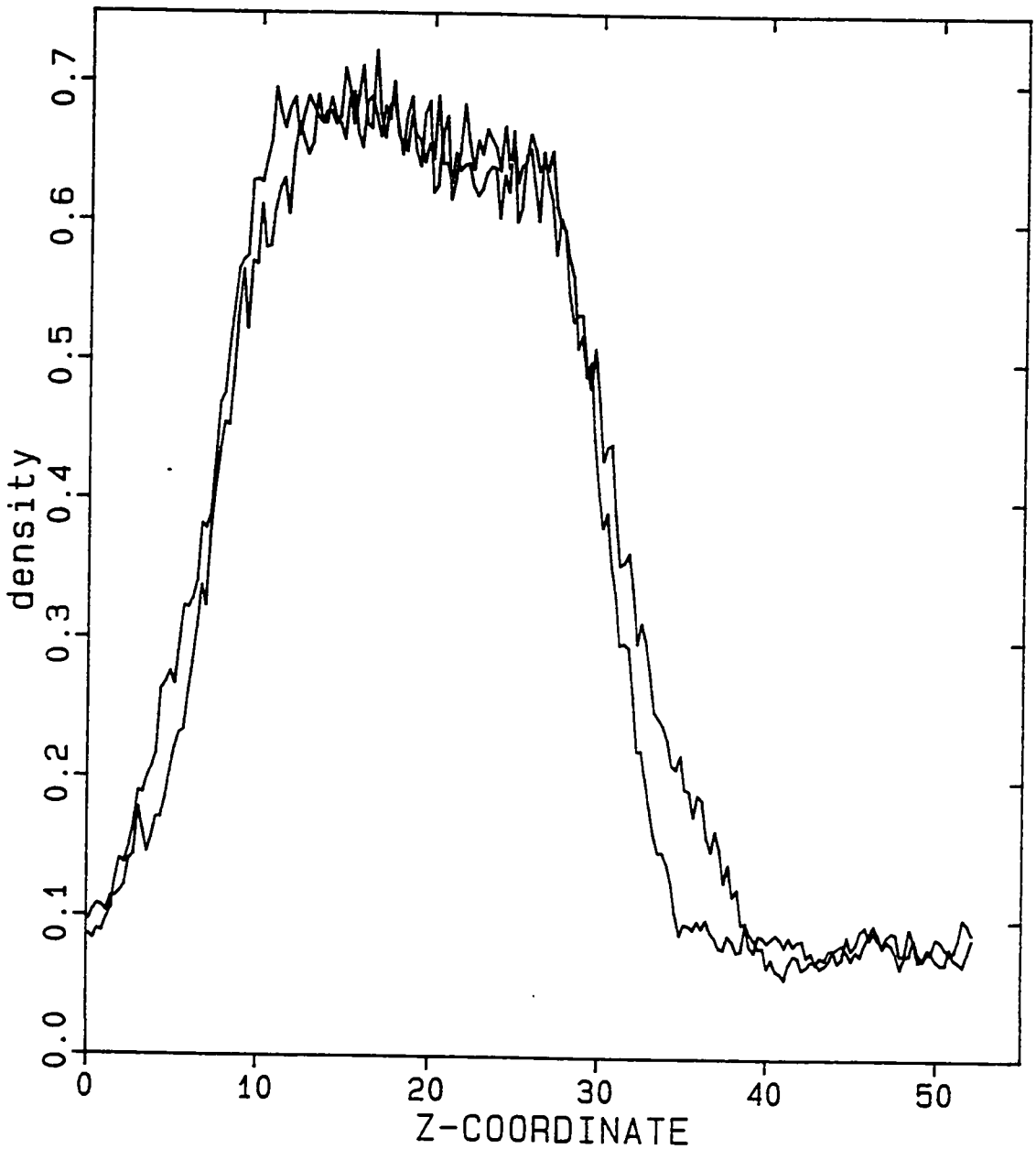

Fig. 3.25 Intermediate results for the density profile at T*=0.474. Each curve is obtained by averaging over 100,000 time steps.

It should be kept in mind that the present computer simulations are restricted to the case of a finite system in a vanishing macroscopic external field. Consequently, for such a two-dimensional system, the critical exponent ω of the interfacial thickness predicted by capillary wave theory which, in its original version, explicitly takes such a field into account at the thermodynamic limit, must be redefined.

Because of the periodic boundary conditions used in the simulations, the wave vectors may take the values

$$|\mathbf{k}| = \frac{2\pi n}{L}, \qquad n=1,2,3,\ldots \tag{3.28}$$

where L is the edge length of the system.

Converting the sum in eqn. (2.17) into an integral but still considering the size of the system to be finite (although large), the mean-squared thickness becomes

$$\lambda^2 = \frac{1}{2\pi\beta K} \int_{|\mathbf{k}_{min}|}^{|\mathbf{k}_{max}|} \frac{d|\mathbf{k}|}{1+\frac{1}{2}l^2|\mathbf{k}|^2}, \tag{3.29}$$

where $|\mathbf{k}_{min}| = \frac{2\pi}{L}$ and $|\mathbf{k}_{max}| = \frac{2\pi}{a_o}$, with a_o the lower wavelength cut off on the capillary fluctuations. Integration of the last equation yields

$$\lambda^2 = \frac{1}{\sqrt{2}\pi\beta K l}\left[\arctan\left(\frac{l|\mathbf{k}_{max}|}{\sqrt{2}}\right) - \arctan\left(\frac{l|\mathbf{k}_{min}|}{\sqrt{2}}\right)\right]. \tag{3.30}$$

If we take the limit of a vanishing external field, the mean-squared thickness is given by:

$$\lambda^2 = \frac{L - a_o}{4\pi^2 \beta \sigma_o} \,. \tag{3.31}$$

The critical exponent ϖ of the root-mean-squared thickness is found, by introducing the power law (1.31) describing the critical behavior of the bare surface tension, to be equal to $\frac{\mu}{2}(=\frac{1}{2}$ in $d=2)$ instead of $\frac{\mu+\beta}{4}$ $(=\frac{9}{32}$ in $d=2)$ obtained in eqn. (2.33).

It may be noted that for the two-dimensional lattice gas in the absence of a macroscopic external field, but with symmetry-breaking boundary conditions, the density profile of the interface can be determined rigorously and its thickness, which must be measured on the scale of the fluctuations since the density profile does not exist at the thermodynamic limit, is found to diverge at the critical point with an exponent $\omega=\frac{1}{2}$.[49]

Snapshots of the particle positions at different temperatures are presented in Figs. 3.26 to 3.34. The bulk correlation length ξ can be roughly estimated from the size of the bubbles present in the bulk liquid. We observe that in accord with intuition the size of the bubbles increases with increasing temperature. When the size of the bubbles is comparable to the system size, as it is when the temperature is close to its critical value, the bulk liquid phase tends to break into several pieces and the two distinct vapor-liquid interfaces no longer exist. As a consequence, there is a upper limit on temperature values in our simulation, which is set by the finite

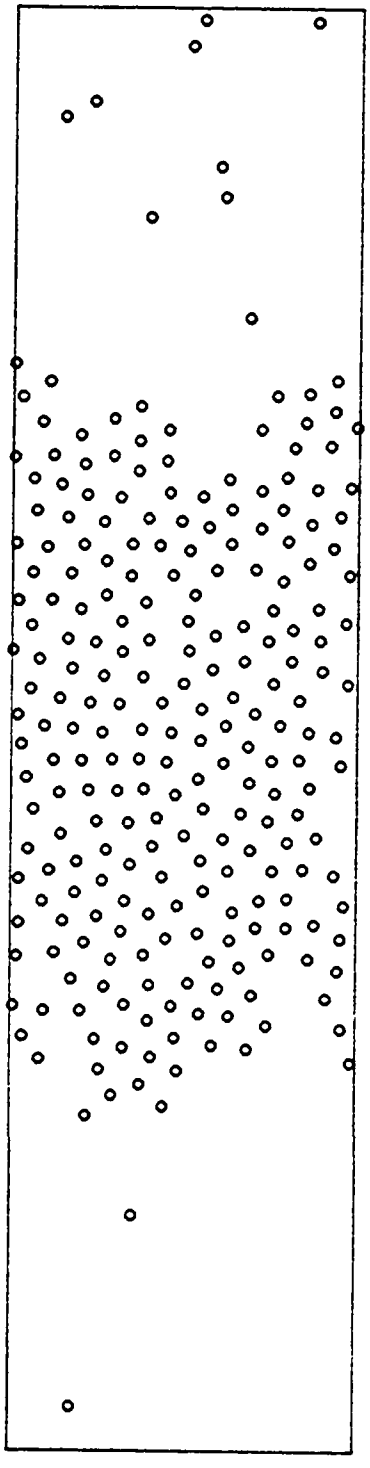

Fig. 3.26 Snapshot of the particle positions at T*=0.424 after a trajectory of 250,000 time steps following equilibration.

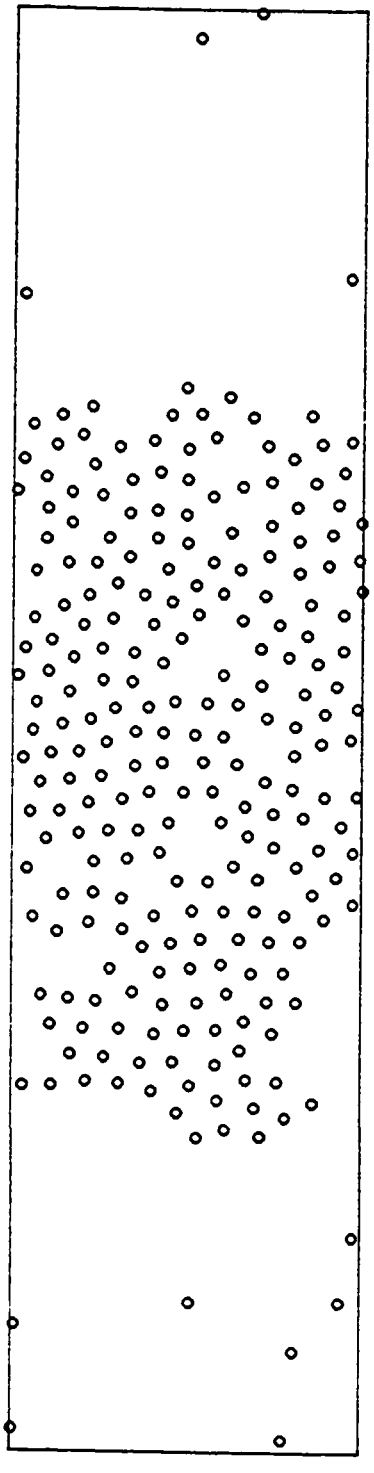

Fig. 3.27 Snapshot of the particle positions at T*=0.433 after a trajectory of 300,000 time steps following equilibration.

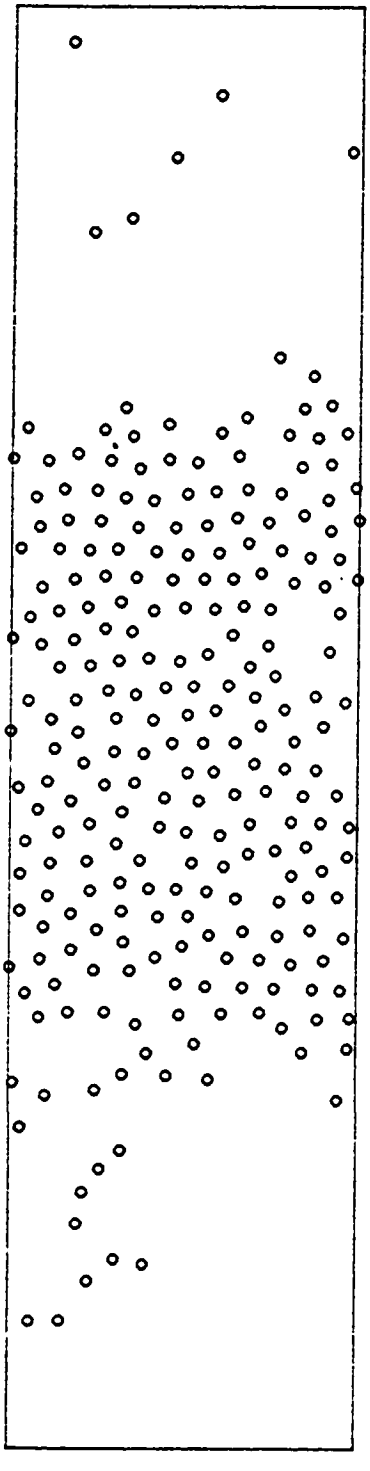

Fig. 3.28 Snapshot of the particle positions at T*=0.436 after a trajectory of 300,000 time steps following equilibration.

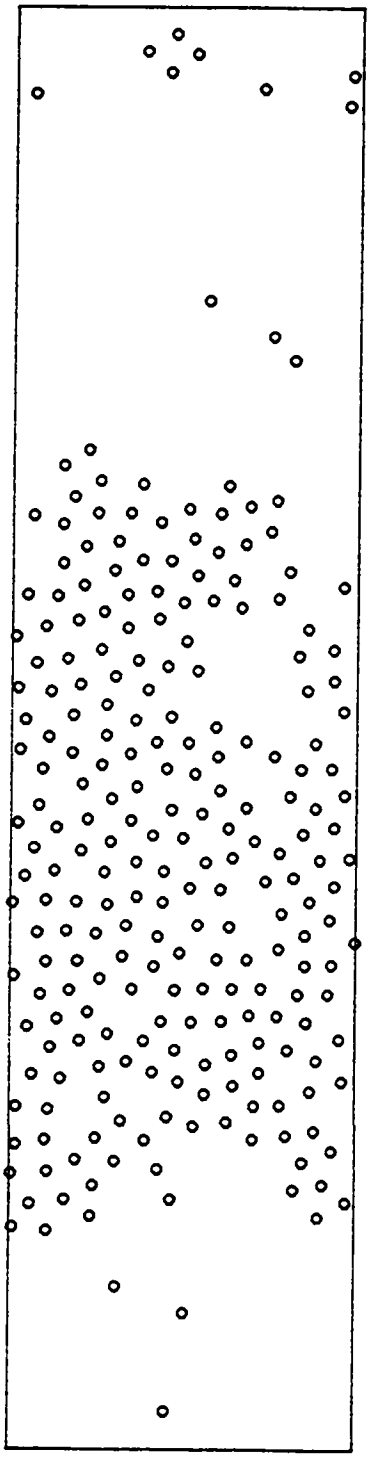

Fig. 3.29 Snapshot of the particle positions at T*=0.441 after a trajectory of 300,000 time steps following equilibration.

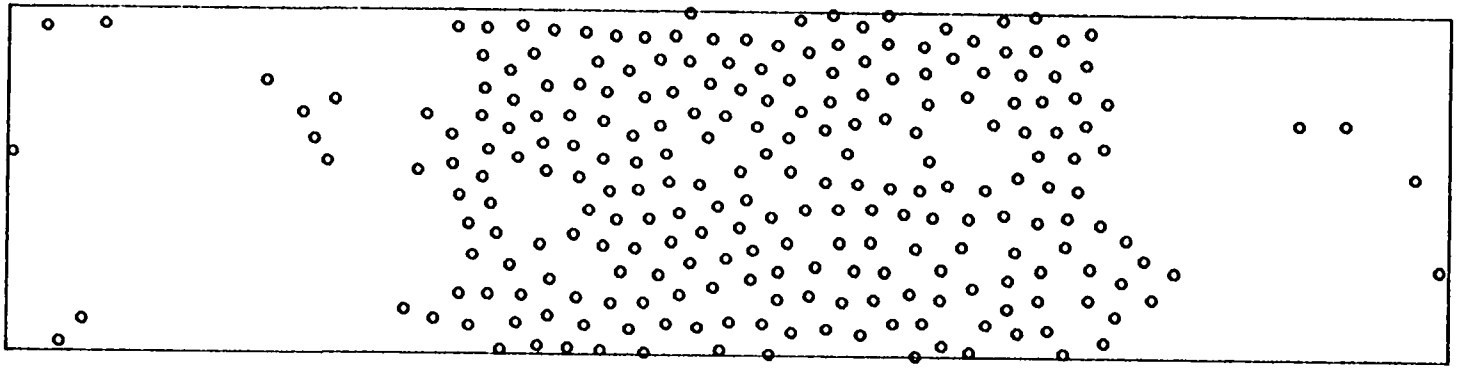

Fig. 3.30 Snapshot of the particle positions at T*=0.446 after a trajectory of 300,000 time steps following equilibration.

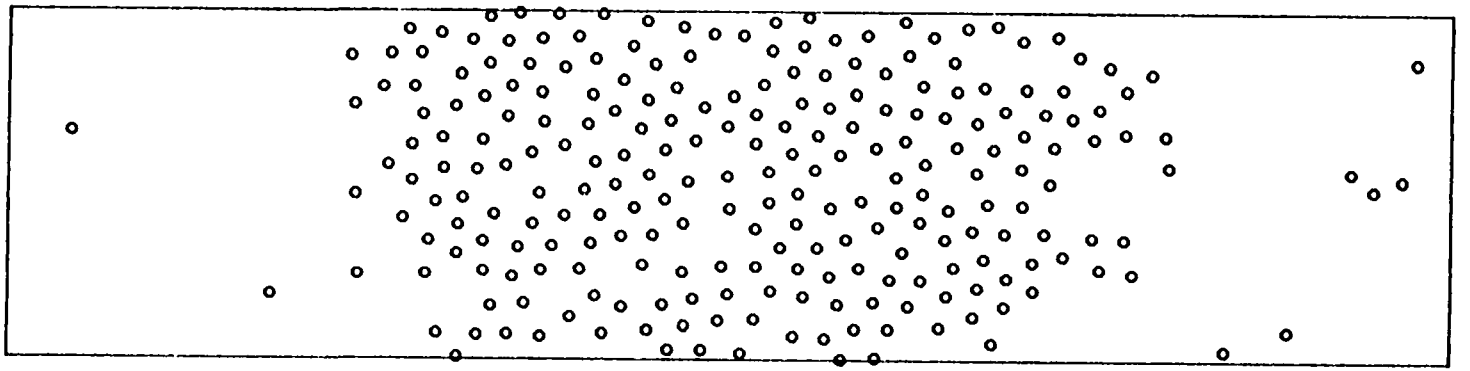

Fig. 3.31 Snapshot of the particle positions at T*=0.456 after a trajectory of 120,000 time steps following equilibration.

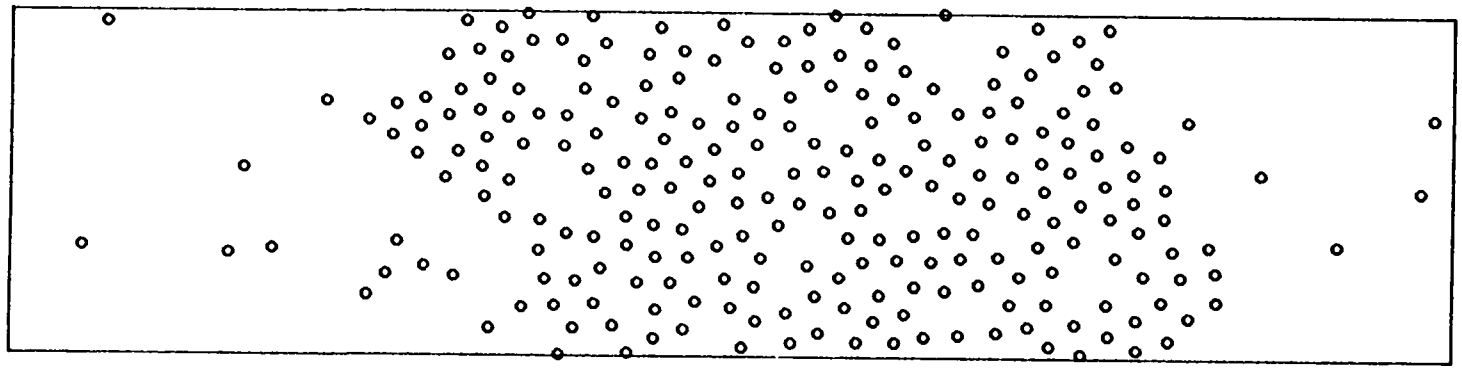

Fig. 3.32 Snapshot of the particle positions at T*=0.461 after a trajectory of 300,000 time steps following equilibration.

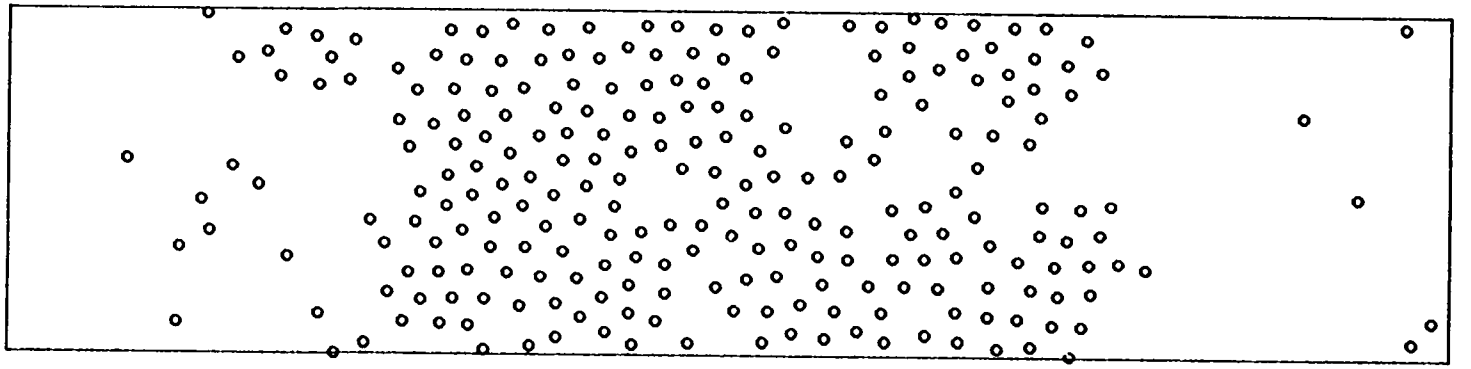

Fig. 3.33 Snapshot of the particle positions at T*=0.468 after a trajectory of 200,000 time steps following equilibration.

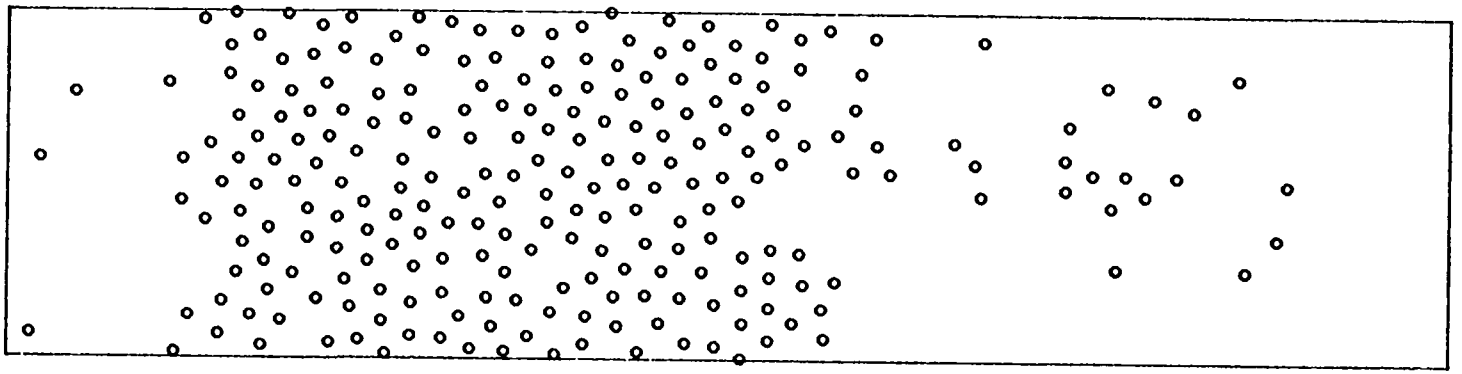

Fig. 3.34 Snapshot of the particle positions at T*=0.474 after a trajectory of 100,000 time steps following equilibration.

size of the system. In our results, the highest temperature we can reach is $T^*=0.474$, beyond which no stable, distinct vapor-liquid interfaces exist.

3.5 SUGGESTED FURTHER STUDIES

It must be appreciated that several points remain unclear and can only be clarified by further studies. In particular, the procedure of determining the critical exponent ω describing the divergence of the interfacial thickness by extrapolating from non-critical temperatures could certainly be improved by studying larger systems. The bulk correlation length will then be allowed to be much larger than the range of the intermolecular forces, so that the critical region can be investigated more closely and more reliably.

It would be of interest to determine the effect of various macroscopic external fields on the critical behavior of the interfacial thickness. Such a study should provide another test of the generalized capillary wave theory of fluid interfaces in external fields and enable us to test the recent theoretical predictions[20] according to which in two- but not in three-dimensional fluids the nature of the increase of the interfacial thickness near the critical point depends strongly on the form of the external field.

In the presence of an external field such as gravity, scaling (non-classical van der Waals) theory breaks down very close to the critical point and the interfacial thickness no longer increases with increasing temperature. Sengers and van Leeuwen[50] have estimated that for Earth gravity in three dimensions, these intrinsic gravity effects become significant at temperature $|T-T_c| < 6X10^{-4}$ °K (see Fig. 2.2). It would be of

interest to estimate the analogous temperature range for two-dimensional systems.

CHAPTER 4

INTERFACIAL PHASE TRANSITIONS IN THREE-COMPONENT SURFACTANT SYSTEMS

It is well known that water and oil are practically insoluble in each other. However, if a small amount of surfactant is added, the mutual solubility of water and oil increases substantially. Within a certain temperature range, the water/oil/surfactant system, which is called a three-component surfactant system, may separate into three coexisting fluid phases, namely, a water-rich (lower) phase, an oil-rich (upper) phase, and a surfactant-rich (middle) phase.

In general, when any three fluid phases coexist at equilibrium, the middle phase can obviously either wet or not wet the interface between the upper and lower phases. These two cases are illustrated in Fig. 4.1. Much less obvious is the fact that a given system can exhibit both types of interfacial behavior (wetting and nonwetting) for different thermodynamic conditions. This transition from a wetting regime to a nonwetting regime, or vice versa, is called a wetting transition, and is the subject of intense current researches[51].

In this chapter, we present experimental results of a systematic search for the occurrence of wetting transitions in three-component

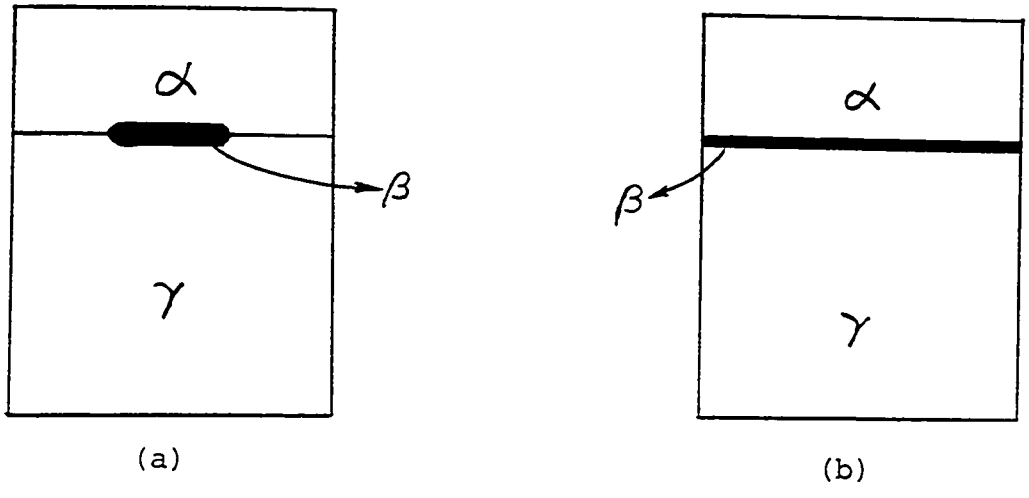

Fig. 4.1 Schematic illustration of three phases in equilibrium: (a) nonwetting and (b) wetting.

surfactant systems consisting of water, an n-alkane, and a nonionic surfactant chosen to be a polyoxyethylene alcohol. The phase behavior of systems of the type water/oil/nonionic surfactant, which has been extensively studied by several investigators[52], is briefly reviewed in Section 4.1. In Section 4.2, we describe the wetting and nonwetting behaviors of these surfactant systems, as well as the wetting transition which may occur between them. The experimental procedure for determining the wetting transition of three-component surfactant systems of the type water/n-alkane/polyoxyethylene alcohol is described in Section 4.3. It is found in Section 4.4 that two such three-component surfactant systems exhibit a wetting transition which lies at least 10 ^{o}C below their upper critical point temperatures, and one three-component surfactant system has a wetting transition which lies 4.3 ^{o}C below its upper critical point temperature. In the last section, some future works are suggested.

4.1 PHASE BEHAVIOR OF THREE-COMPONENT SURFACTANT SYSTEMS

Surfactant systems are known to exhibit remarkable properties. In particular, the surface tensions of their various interfaces are found to be very low. For this reason, surfactant systems are widely studied because of their potential use in many industrial applications such as tertiary oil recovery, detergency, pharmaceuticals and cosmetics. For example, while the surface tension between pure water and oil is typically about 50 mN/m, addition of surfactant to the system reduces the surface tension to

as little as 0.01 mN/m; this fact is exploited in modern technological methods used to enhance recovery of oil trapped by surface forces in porous reservoirs.

The phase behavior of a ternary mixture of water/oil/nonionic surfactant depends on temperature, pressure and the nature of the components. According to Winsor's classification[53], which is illustrated in Fig. 4.2, the various phase equilibria of such systems can be grouped into three types:

Type I phase equilibria consist of two phases with most of the surfactant dissolved in the aqueous phase and a small amount of oil dispersed in the aqueous phase, and are commonly called lower-phase microemulsions.

Type II phase equilibria consist of two phases with most of the surfactant dissolved in the oil-rich phase and a small amount of water dispersed in the oil-rich phase, and are commonly called upper-phase microemulsions.

Type III phase equilibria consist of three phases with a middle phase containing most of the surfactant and significant amounts of water and oil, which coexists with a water-rich phase and an oil-rich phase. These middle-phase are called middle-phase microemulsions.

At constant pressure, these three types of phase equilibria can be observed in three-component surfactant systems by simply varying temperature, as shown in Fig. 4.2. The surfactant transfers continuously from the water-rich phase to the oil-rich phase as the temperature rises, i.e., the mutual solubility between surfactant and oil increases with rising temperature. One finds Winsor type I phase equilibria at low

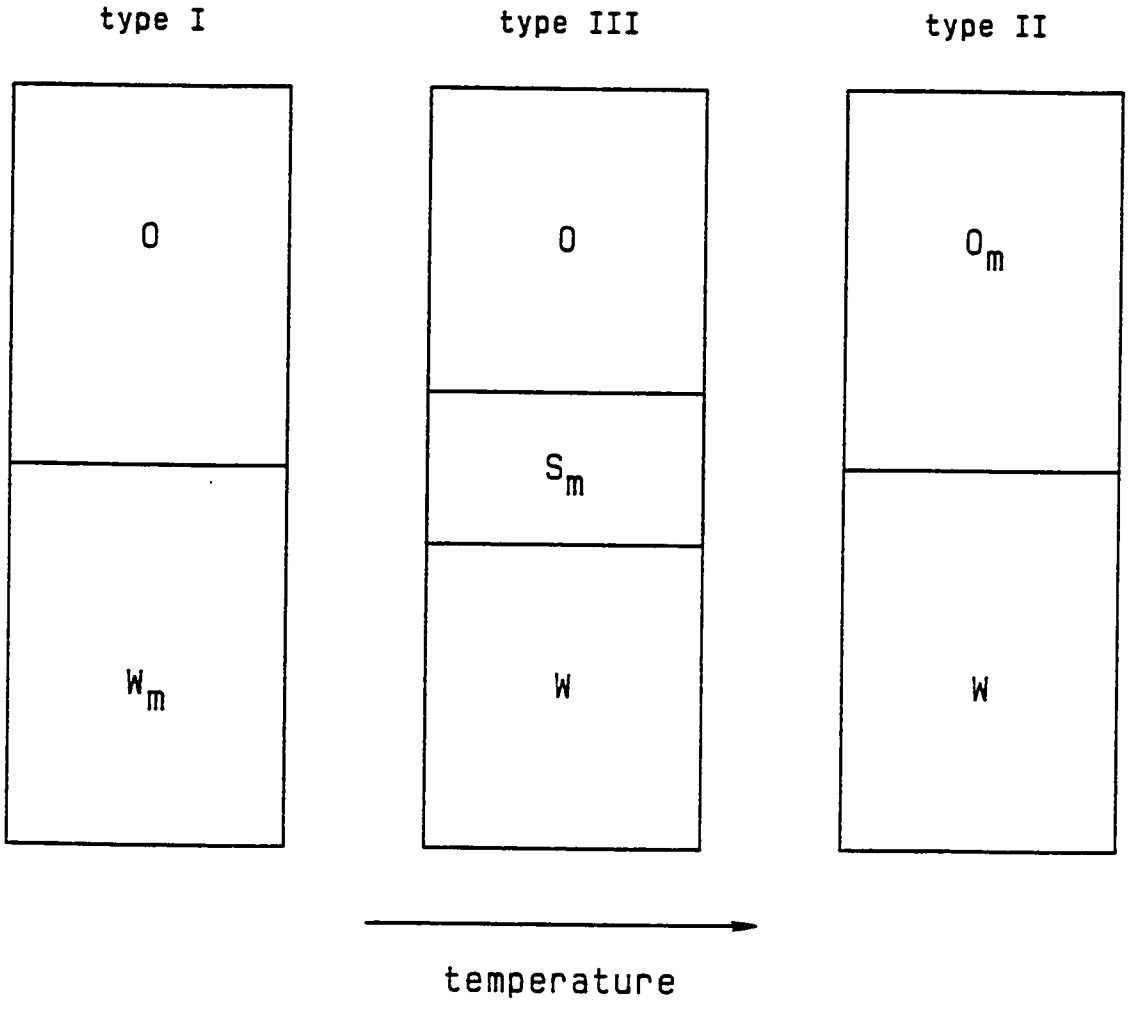

Fig. 4.2 Three types of phase equilibria according to Winsor (Ref. 53). O, S and W denote oil-rich, surfactant-rich and water-rich phases, respectively. The subscript m stands for microemulsion and denotes a microemulsion.

temperatures and Winsor type II phase equilibria at high temperatures. In between, one may or may not find Winsor type III phase equilibria, depending on the nature of the oil and of the surfactant.

Apart from temperature, there are other system parameters that can be chosen to monitor the phase behavior between types I-III-II. These system parameters are the alkyl chain length of the surfactant, the aromaticity of the oil, and the concentration of salt.[52a,d]

The ternary phase diagrams of surfactant systems as a function of the system parameter mentioned above are schematically shown in Fig. 4.3, where S, O, and W represent, respectively, surfactant, oil, and water, the dashed lines represent the tie-lines of two-phase equilibria, and the solid lines in diagrams (b) and (d) are critical tie-lines. The compositions may be expressed either in weight, volume or mole fractions. If the system parameter is chosen to be temperature, the diagrams (b) and (d) in Fig. 4.3 correspond to the phase diagrams, respectively, at the lower critical temperature T_l and at the upper critical temperature T_u. The phase diagram (a) below T_l represents a typical phase diagram of the Winsor type I, while the diagram (e) above T_u is a typical phase diagram of the Winsor type II and the diagram (c) between T_u and T_l a typical phase diagram of the Winsor type III.

With increasing temperature, the three-phase triangle stems from the lower critical tie-line at T_l, i.e., a lower-phase microemulsion separates into a middle-phase microemulsion and a water-rich phase, and the triangle reduces to an upper critical tie-line at T_u , i.e., a middle-phase microemulsion and oil-rich phase merge into a upper-phase

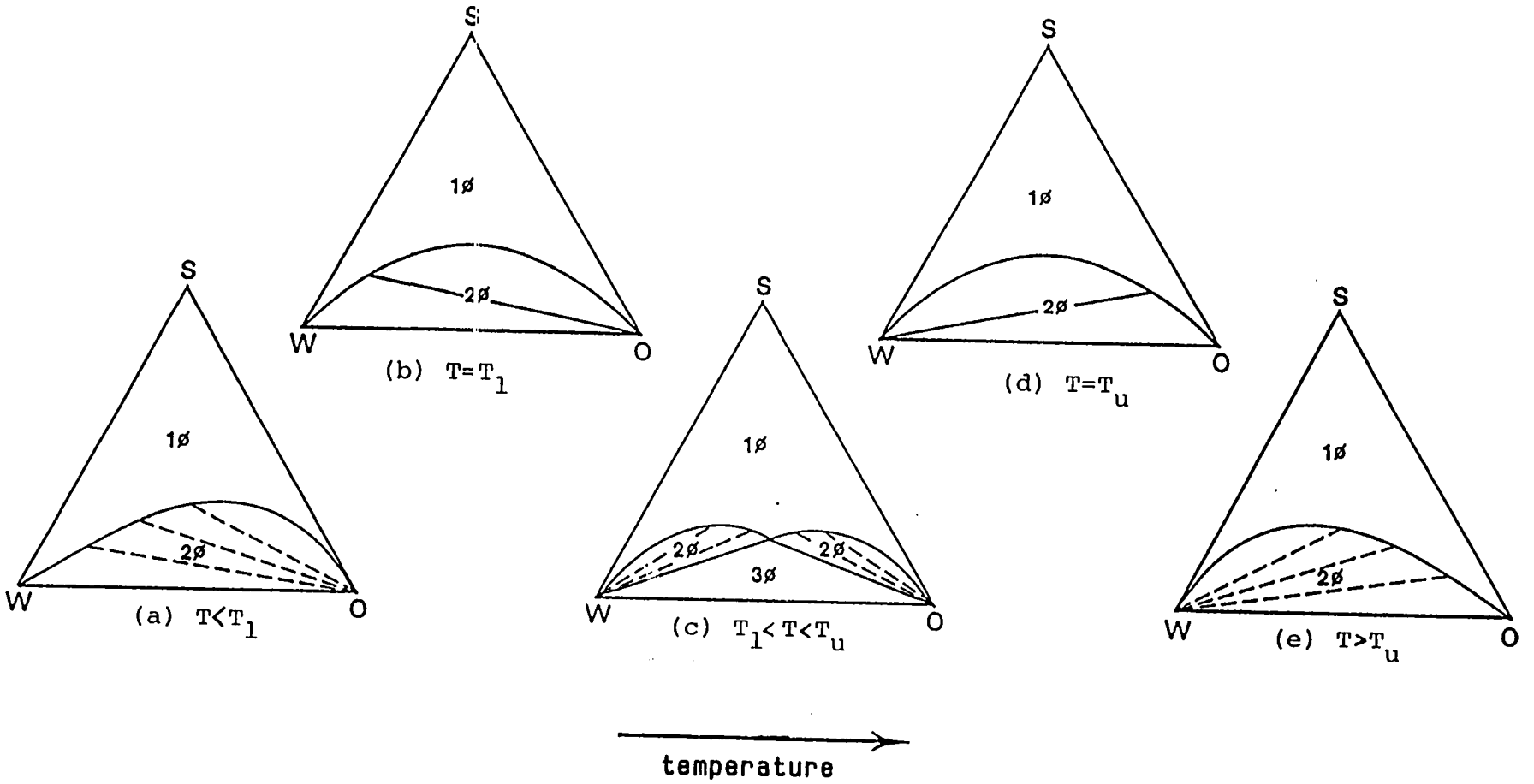

Fig. 4.3 Schematic illustration of simple microemulsion phase behavior as a function of system parameter (here temperature).

microemulsion. Between T_l and T_u, the shape of the three-phase triangle changes such that the top of the triangle moves continuously from the left (lower critical point) to the right (upper critical point) as the temperature increases.

Note that the general pattern of the phase diagrams discussed above only covers the region of low volume (weight) fraction of surfactant. If the volume (weight) fraction of surfactant is high enough, various ordered liquid crystalline phases such as lamellar or hexagonal phases may also appear, depending on the nature of the surfactant. For long chain surfactant/water/oil systems, liquid crystalline phases exist in a wide range of compositions.(52a)

We focus next on the phase behavior of some well-studied systems of the type water/n-alkane/C_iE_j, where C_iE_j denotes a polyoxyethylene alcohol $C_iH_{2i+1}(OCH_2CH_2)_jOH$. Fig. 4.4 shows the phase diagrams of the systems water/n-decane/C_4E_1, water/n-decane/C_8E_3, and water/n-tetradecane/$C_{12}E_5$, at different temperatures(54).

For short-chain surfactants like C_4E_1 and C_8E_3, the short hydrocarbon chain is not sufficient to stabilize a liquid crystalline phase, hence the phase equilibria involving only liquid phases are much easier to reach. For example, equilibrium of the systems containing C_4E_1, C_4E_2, C_6E_2, or C_8E_3 can be reached within minutes(52b). However, equilibration processes of some systems containing $C_{10}E_4$ may take more than four years(52b). The water/n-decane/C_8E_3 system forms a lamellar phase(52c), but only at temperatures well below the three-phase region ($T_l<T<T_u$). Fig.

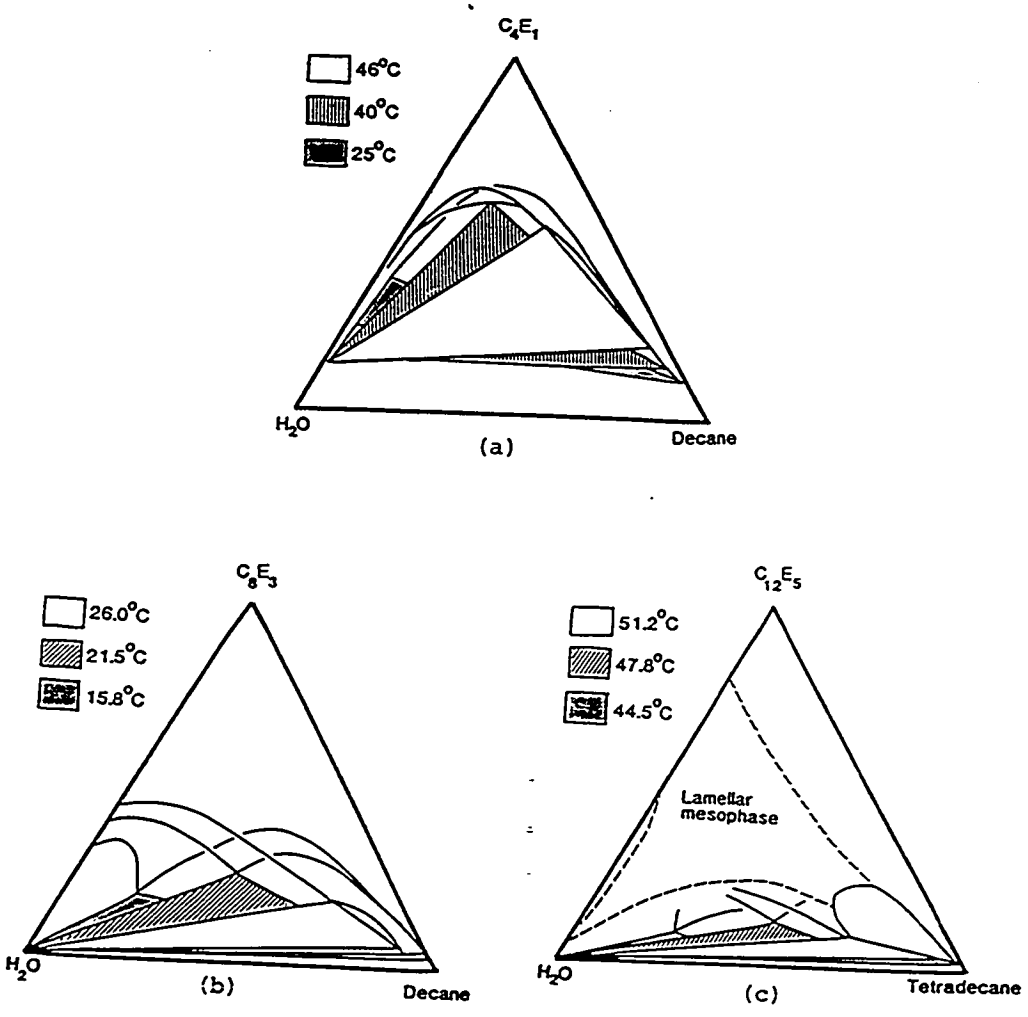

Fig. 4.4 Evolution of the three-phase triangle with increasing temperature for three surfactant systems (Ref. 54).

4.4(c) shows that $C_{12}E_5$ forms a lamellar phase even at temperatures between T_l and T_u.

As the temperature rises, the evolution of the three-phase triangle in Fig. 4.4 is quite similar for different systems. The most pronounced difference among the phase diagrams of different systems is the shape of the three-phase triangles: the longer the chain of the surfactant, the closer the top of the three-phase triangle to the water-oil side of the triangle. This difference implies that the more amphiphilic the surfactant, the better the ability of the surfactant to solubilize water and oil.

Apart from showing the complete miscibility between n-decane and C_8E_3, Fig. 4.4(b) also shows that there is a distinct miscibility gap along the C_8E_3-water edge, and this gap becomes more pronounced at higher temperatures. The miscibility gap along the C_iE_j-water edge does not exist in the systems water/n-alkane/C_4E_1 and water/n-alkane/C_4E_2. However, the miscibility gap appears in the systems water/n-alkane/C_6E_2. As a consequence of the presence of this miscibility gap, there is no critical point for the two-phase region fanning out from the surfactant-water edge to the n-alkane-water edge.

4.2 WETTING AND NONWETTING REGIMES

Over thirty years ago, Buff and Saltsburg[55] found that in the three liquid-phase region of the system water/heptane/aniline, the middle aniline-rich phase completely wets the interface between the lower aqueous and the upper heptane-rich phases. But when detergent is added to the

system, these authors found that the middle phase collapses into a lens floating on the interface between the upper and lower phases. In these experiments the detergent was not well characterized.

Whether the middle phase wets or does not wet the interface between the upper and lower phases is determined by the surface tensions of the interfaces separating the various coexisting phases. Consider a system of three phases α, β, and γ in equilibrium, as illustrated in Fig. 4.1. There are three surface tensions: $\sigma_{\alpha\beta}$, $\sigma_{\alpha\gamma}$, and $\sigma_{\beta\gamma}$, which are the surface tensions of the α-β, α-γ, and β-γ interfaces, respectively.

When the middle β phase wets the interface between the upper α and lower γ phases, the surface tensions satisfy Antonow's rule[56]:

$$\sigma_{\alpha\gamma} = \sigma_{\alpha\beta} + \sigma_{\beta\gamma} \ . \qquad (4.1)$$

When eqn. (4.1) holds, the contact angle between the β phase and the α-γ interface is zero, and the β phase completely spreads across the interface between the α and γ phases.

When the middle β phase does not wet the interface between the upper α and lower γ phases, the surface tensions are related by Neumann's inequality[57],

$$\sigma_{\alpha\gamma} < \sigma_{\alpha\beta} + \sigma_{\beta\gamma} \ . \qquad (4.2)$$

When eqn. (4.2) holds, the contact angle between the β phase and the α-γ interface is nonzero, and therefore the β phase only partially wets the α-γ interface.

Measurements of interfacial tensions have been performed[58] for three-phase surfactant systems, in which the surfactant can be either anionic, such as sodium dodecyl sulfate (SDS), cationic, such as dodecyltrimethyl-ammonium bromide (DTAB), or nonionic, such as dodecyl hexaoxyethylene alcohol ($C_{12}E_6$). It has been reported[58d] that close to optimal conditions, where approximately equal amounts of oil and water are solubilized, $\sigma_{\alpha\gamma}$ is nearly equal to the larger of $\sigma_{\alpha\beta}$ and $\sigma_{\beta\gamma}$, and consequently the middle β phase is found to be nonwetting.

Typical experimental results[59] for interfacial tensions as well as for the phase volume percentage of the three phases for the system water/n-decane/C_8E_3 are shown as a function of temperature in Fig. 4.5. From the phase behavior discussed in the previous section, since the β and γ phases separate at T_l, the surface tension $\sigma_{\beta\gamma}$ is equal to zero below and at T_l, and increases with increasing temperature. On the other hand, the α and β phases merge into a single phase at T_u, and therefore $\sigma_{\alpha\beta}$ decreases with rising temperature and becomes zero at T_u. The dashed line in Fig. 4.5 represents the sum of $\sigma_{\alpha\beta}$ and $\sigma_{\beta\gamma}$. $\sigma_{\alpha\gamma}$ is always inferior to the sum of $\sigma_{\alpha\beta}$ and $\sigma_{\beta\gamma}$, i.e., eqn. (4.2) holds, and therefore the middle β phase does not wet the interface between the aqueous and n-decane-rich phases.

This observation is consistent with the predictions of the theory recently proposed by Jeng and Miller[60]. These authors assume the microstructure of the microemulsion phases to be one of monodispersed,

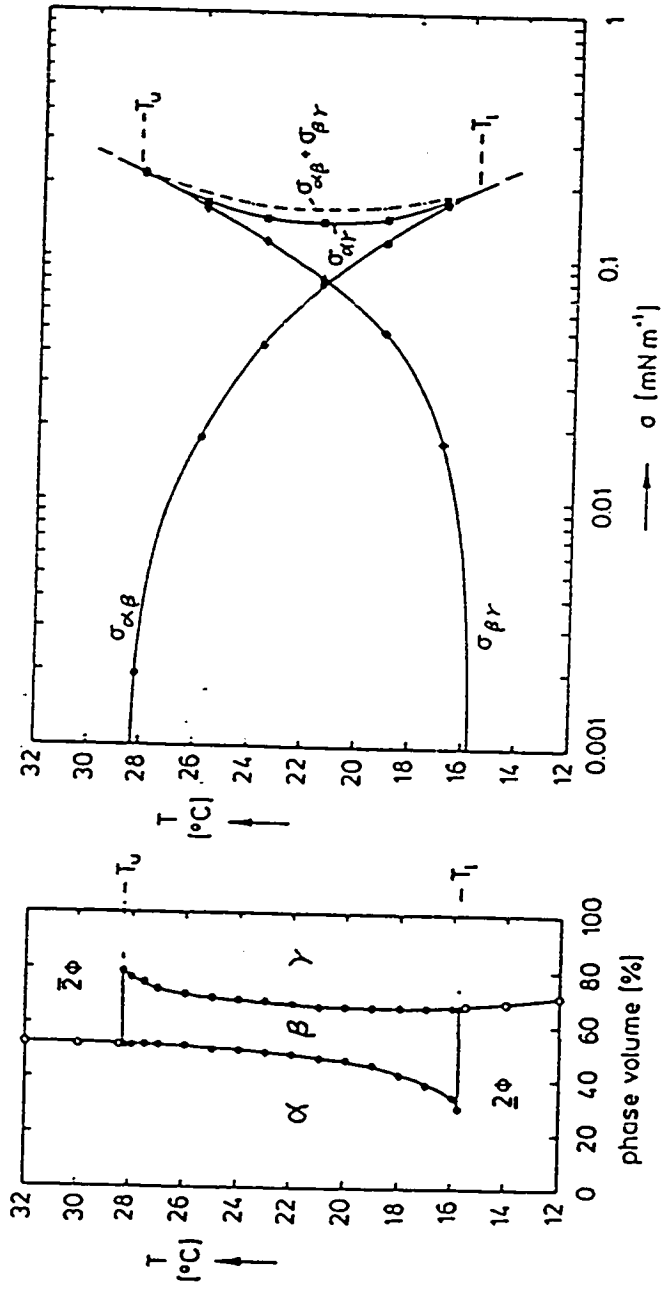

Fig. 4.5 (a) Phase volume percentage and (b) surface tensions of the three-phase region of the system water-n-decane-C_8E_3. (Ref. 59)

spherical drops. In addition, the interfacial structures of the middle-upper and middle-lower interfaces are precisely and realistically defined: a surfactant monolayer for one interface and a more diffuse interface for the other. This view of two coexisting , but structurally different interfaces in a three-phase microemulsion equilibrium is supported by experimental findings[58]. These authors also found that the middle phase always exhibits nonwetting behavior.

Note that the β phase is found[58,59] to be nonwetting, except possibly very close to the critical endpoint, only for the systems containing the moderate or long chain amphiphiles such as C_8E_3, $C_{12}E_6$, SDS, and DTAB. In contrast, the β phase is found[61] to be wetting across the α-γ interface for the systems with small nonionic surfactants, such as ethanol, propanol, and butanol, at all temperatures between T_l and T_u.

According to the phenomenological arguments of Cahn[62a] and Ebner and Saam[62b], when a three-phase system with a nonwetting middle phase approaches a critical endpoint, the middle phase should completely wet the interface between the upper and lower phases. In other words, as a multiphase system is brought close to a critical endpoint, these arguments predict that a transition must occur from a nonzero contact angle (partial wetting) to a zero contact angle (complete wetting). Such a transition has been observed in a mixture of cyclohexane and methanol[63], as well as in a few other binary mixtures[64].

However, it has been found[65] that contrary to these theoretical predictions, some systems do not undergo a wetting transition and remain in a nonwetting regime up to a critical point. An interesting suggestion[66]

is that for the system SDS/1-butanol/brine/n-heptane the middle phase may exhibit both wetting and nonwetting behaviors at different compositions. This ionic surfactant system would thus appear to be a good candidate for our wetting transition study. However, the phase behavior of a five-component system is very complicated. As a consequence, the determination of the locations of the wetting transition points and the critical endpoints in this system would require extensive and time-consuming efforts.

On the other hand, in three-component nonionic surfactant systems, the phase behavior is much easier to determine with the temperature as the unique system parameter. According to Gibbs' phase rule, there is only one degree of freedom for a three-component system separating into three phases at a fixed pressure. We thus expect to observe a wetting transition, if it exists, by simply varying the temperature. The temperature at which the phase transition occurs from wetting to nonwetting, or vice versa, is called the wetting transition temperature.

According to the available experimental results[67] mentioned above, in the water/n-decane/C_8E_3 system, the middle phase does not wet the α-γ interface, while in the water/n-alkane/C_4E_1 system, the middle phase completely wets the α-γ interface at all temperatures between T_l and T_u. It is therefore natural to conjecture that in three-component surfactant systems the chain length of the surfactant molecule plays a crucial role in the existence of a wetting transition. More precisely, if a wetting transition occurs far from the critical endpoints in any of the water/n-alkane/C_iE_j

systems, the systems exhibiting a wetting transition must be those with a surfactant intermediate between C_4E_1 and C_8E_3.

In this study, we undertake a systematic experimental search for the wetting transition temperature in water/n-alkane/C_iE_j systems. For each system, we expect to find two wetting transition temperatures: one close to the lower critical temperature T_l and the other one close to the upper critical temperature T_u, as is schematically illustrated in Fig. 4.6.

4.3 EXPERIMENTAL

In laboratory experiments, the wetting and nonwetting regimes can be distinguished by direct eye observation, provided sufficient care is taken. In fact, such direct eye observation may well be the most reliable method to determine whether a wetting transition occurs[68]. In order to perform such experiments, one must prepare a sample containing three liquid-phases in equilibrium with a small amount of the middle phase. If the amount of the middle phase is sufficiently small, the latter can form either a lens floating on the interface between the upper and lower phases or a ring along the walls of the test tube, indicating nonwetting behavior, or it can spread across the interface and form a very thin layer between the upper and lower phases, indicating wetting behavior.

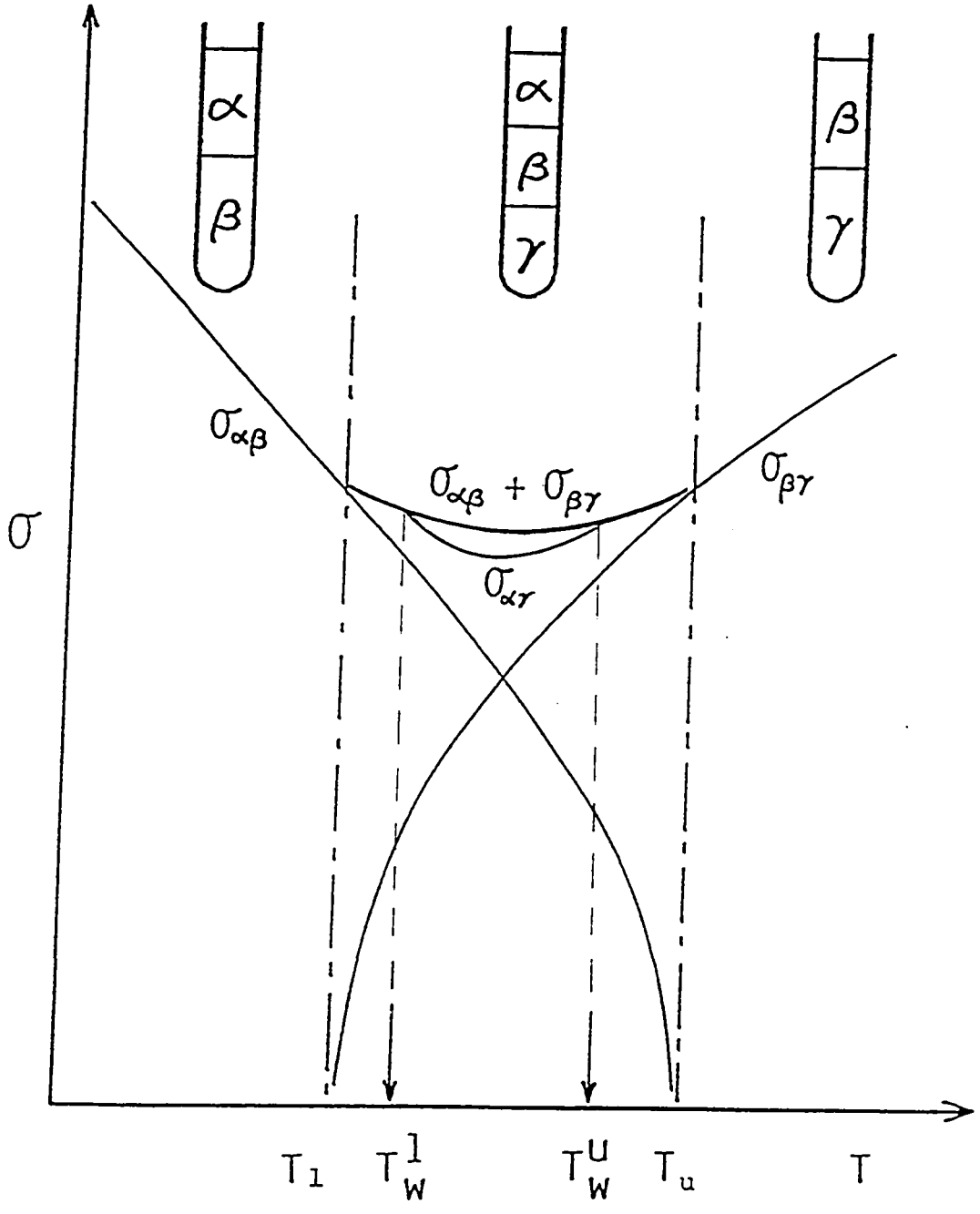

Fig. 4.6 Qualitative behavior of surface tensions for systems with two wetting transition temperatures T_w^l and T_w^u.

Materials

The hydrocarbons we use, n-octane, n-decane, n-dodecane, n-tetradecane, and n-hexadecane are products of Aldrich Chemical Co. with 99+% purity, while n-hexane, n-heptane, and n-octadecane are products of Fluka Chemical Co. with 99+% purity. The nonionic amphiphiles C_4E_1(99+%), C_4E_2(99%), and C_6E_2(99+%) are also purchased from Aldrich Chemical Co. All these chemicals are used without any further purification, and water is purified by a Barnstead NAPOpure II System.

Procedure

The samples are prepared in a clean glass test tube of 1 cm in diameter, and the compositions are chosen in a volume ratio of water: oil: C_iE_j roughly equal to 10: 2: 1. To avoid any perturbation of the phase equilibrium of the system, no color enhancing dies are used. To allow the system to reach equilibrium, the prepared sample is set aside at room temperature for several hours. If room temperature is higher than the upper critical temperature or lower than the lower critical temperature of the system, the sample is placed in a air bath which is set at a temperature lying within the three-phase region. The sample is kept in the air bath for several hours to allow the system to reach equilibrium. Before and during the equilibration process, the samples are shaken vigorously several times to ensure a thorough mixing. After equilibrium is reached, all three phases are transparent with sharp, mirror-like interfaces. Following

equilibration, the upper and lower phases are carefully removed and put into a second test tube by using pipettes. Next, one or two drops of the middle phase are added to the second test tube containing only the upper and lower phases, and in the nonwetting regime the middle phase is seen to form a lens floating on the interface between the upper and lower phases.

It should be pointed out that if a parallelepipedic optical cell is used, the middle phase is seen to form a ring, instead of a lens, at the edges of parallelepiped[69](Fig. 4.8). We believe that this difference in the nonwetting geometry is due to the nature and shape of glass.

Next, the samples are placed in a water bath. The temperature of the water bath, which is indicated by a calibrated mercury thermometer, is controlled manually and allowed to vary at a rate of no more than a degree per ten minutes. The wetting transition temperature T_w is recorded by direct eye observation of the spreading and contracting of the middle phase as the temperature is respectively increased above and decreased below T_w. The phenomenon is schematically shown in Fig. 4.7

A typical run includes several such increases and decreases of the temperature, respectively above and below T_w, to examine the reversibility of this interfacial transition, as schematically illustrated in Fig. 4.7. During the process of increasing or decreasing temperature, all three phases remain transparent. The transition we observe is very abrupt in that the surfactant-rich phase is seen to spread (contract) rapidly as soon as the temperature reaches T_w from below (above). We believe the observed spreading (contracting) at $T=T_w$ is a true equilibrium phenomenon and is not induced by heat transfer from test tube walls, because the latter would

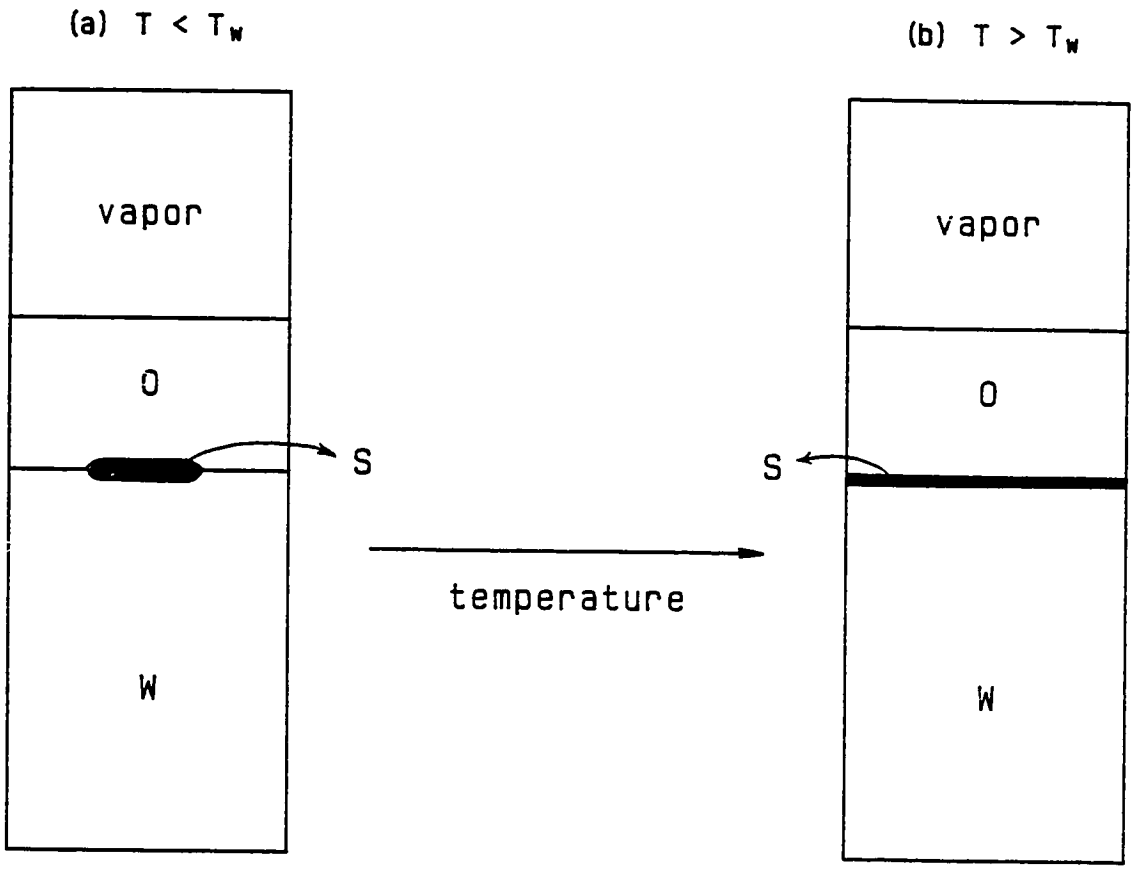

Fig. 4.7 Schematic illustration of the observation of the wetting transition from nonwetting (a) to wetting (b). O, W and S denote respectively oil-rich, water-rich and surfactant-rich phases.

have also induced spreading at any temperature, including at those below T_w.

4.4 RESULTS AND DISCUSSION

In Table 4.1, we list all the three-component surfactant systems used in our search of the wetting transition. First, we observe that no wetting transition near the lower critical temperature is found in these systems. Next, all systems of the type water/n-alkane/C_4E_j are found to exhibit wetting behavior for all the temperatures between the lower and upper critical temperatures T_l and T_u. Among the systems we study, we find two systems, water/n-hexadecane/C_6E_2 and water/n-octadecane/C_6E_2, which exhibit a wetting transition lying at least 10 ^oC below the upper critical temperature, and one system, water/n-tetradecane /C_6E_2, which exhibits a wetting transition 4.3 ^oC below its upper critical temperature. Our results are summarized in Table 4.2, where the upper critical temperatures of the systems are also given. These results are reproducible for several different samples, and the wetting transition is also found to be fully reversible.

Our results for the system water/n-hexadecane/C_6E_2 agree with the earlier observations of Robert and Jeng[70]. These results have also been reproduced and confirmed by Perrot, Robert and Beysens[69] in the Laboratory of Dr. Beysens at the French Center for Nuclear Studies in Saclay. In the experiments of Perrot, Robert and Beysens, the middle phase is seen to form a ring, instead of a lens, at the edges of a

Table 4.1 The three-component systems water/n-alkane/C_iE_j used in the search of the wetting transition temperature.

	C_4E_1	C_4E_2	C_6E_2
n-hexane		X	
n-heptane	X		
n-octane	X	X	
n-decane	X		X
n-dodecane	X		X
n-tetradecane	X		X
n-hexadecane			X
n-octadecane			X

Table 4.2 The wetting transition temperatures T_w and the upper critical temperatures T_u of the systems water/n-alkane/C_6E_2.

System	T_w(°C)	T_u(°C)
water/n-octadecane/C_6E_2	62.0	75.0
water/n-hexadecane/C_6E_2	49.1	61.0
water/n-tetradecane/C_6E_2	42.0	46.3

parallelepiped optical cell. The observation of the wetting transition in a parallelepiped optical cell is schematically illustrated in Fig. 4.8.

Due to the fact that only a small amount of the middle phase is present in our experiments, it is necessary to verify that the phenomenon we observe is really a wetting transition rather than the disappearance of the middle phase as the system moves from a three-phase region into a two-phase region upon increasing the temperature. This verification is confirmed by our observation that the amount of the middle phase does not decrease during the heating process up to the wetting transition temperature; indeed, the amount of the middle phase is expected to decrease gradually if the system is moving away from a three-phase region into a two-phase region.

We also perform another experiment to confirm that the wetting transition we observe is not due to the system moving away from a three-phase region into a two-phase region upon increasing the temperature. First, we prepare a sample with a volume ratio of water: oil: C_6E_2 approximately equal to 10: 2: 1. This sample is then placed into a air bath at a temperature higher than the transition temperature already observed; it is kept there for several hours to allow the system to reach equilibrium. Before and during the equilibration process, the samples are shaken vigorously several times to ensure a thorough mixing. After equilibrium is reached, the upper and lower phases are very carefully removed to another test tube by using pipettes. Then, a drop of the middle phase is added to the test tube containing the upper and lower phases only. It is found that the middle phase completely wets the interface between the upper and lower

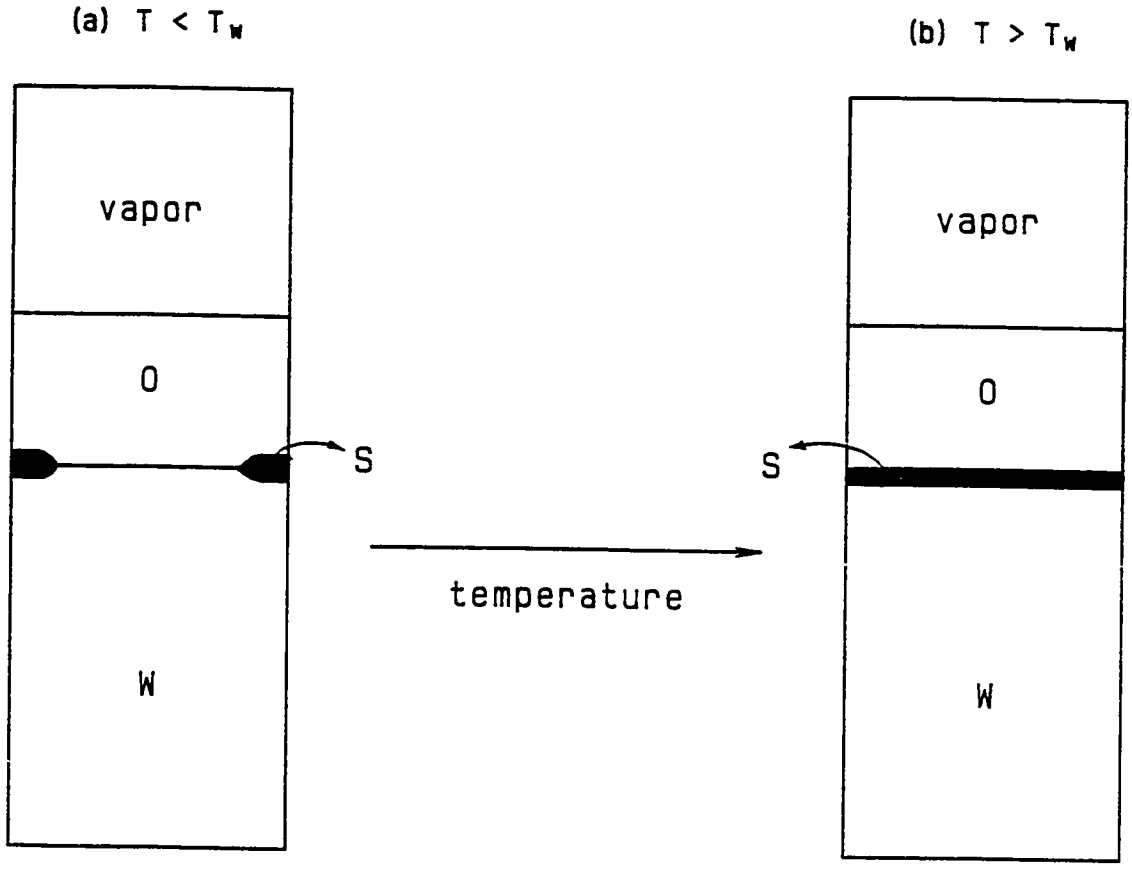

Fig. 4.8 Schematic illustration of the observation of Perrot, Robert and Beysens (Ref. 69) for the wetting transition from nonwetting (a) to wetting (b). O, W and S denote respectively oil-rich, water-rich and surfactant-rich phases.

phases. This implies and confirms the existence of a wetting transition at a temperature T_w since the middle phase forms a lens below T_w and completely wets the interface between the upper and lower phases above T_w. Furthermore, this sample can be used to locate the transition temperature following the same procedure mentioned above, and the transition temperature is reproduced and found to be consistent with the results observed in the first set of different experiments.

It has been briefly mentioned by Widom[71] that wetting transitions in surfactant systems may be related to the molecular structure of the surfactant in. According to the experimental evidence[72] on the microstructure of these systems, surfactants of the type C_4E_j form neither micelles nor liquid crystalline phases, surfactants of the type C_6E_j form apparently only micelles, while surfactants of the type C_iE_j with $i \geq 8$ form both micelles and liquid crystalline phases. Therefore, the more amphiphilic the surfactant, the stronger its tendency to form micelles and liquid crystalline phases. In other words, the systems with smaller amphiphiles are less specifically structural or more molecularly dispersed.

All the systems of the type water/n-alkane/C_4E_j investigated in our study are found to exhibit wetting behavior for all temperatures between T_l and T_u. On the other hand, the systems of the type water/n-alkane/C_8E_j have been reported[67] to exhibit nonwetting behavior all the temperatures between T_l and T_u. It thus appears that the formation of the microstructure such as micelles will induce the system to exhibit nonwetting behavior.

In the light of these observations, a possible explanation of the occurrence of the wetting transition we observe in the systems water/n-tetradecane/C_6E_2, water/n-hexadecane/C_6E_2, and water/n-octadecane/C_6E_2 may be the transition of the microstructure of the microemulsion phase from micellar to random as temperature increases.

4.5 SUGGESTED FURTHER STUDIES

In the course of this study, several problems have arisen which appear to be worthy of investigation. We shall briefly describe some of them and suggest possible approaches to their solutions.

At the end of the previous section, a tentative explanation for the occurrence of a wetting transition in surfactant systems is proposed. It would be of interest to have firm experimental evidence to test this explanation. This evidence may be obtained by nuclear magnetic resonance and light scattering techniques, which have been widely used to determine the microstructure of microemulsions[72].

Another approach which could shed light on this problem is that of computer simulations. Several investigators[73] have applied molecular dynamics and Monte Carlo simulation techniques to study a single spherical micelle. In particular, a Monte Carlo simulation of an idealized lattice model has been successfully performed by Larson[74] to study the microstructure of water/oil/surfactant systems in two and three dimensions. As expected, the formation of microstructures was found to depend on the composition, the length of the surfactant, and the ratio of the

length of the hydrophilic part to that of the hydrophobic part of the surfactant molecule. It was also found that as the surfactant concentration decreases, the microstructure evolves from a lamellar phase to a cylindrical micellar phase and then to a spherical micellar phase. This evolution reproduces reasonably well that of a real system. These studies thus show that phase behavior of surfactant systems can be predicted qualitatively by computer simulations. In addition, ultralow surface tensions, which are an important characteristic of real microemulsions, were also found in Larson's study.

In view of these encouraging results, computer simulation appears to be a promising method to study the origin of wetting transitions in microemulsions. Another advantage of computer simulation is that the role played by surfactant molecular structure in the existence of the wetting transition can be easily investigated by varying both the length of the surfactant tail and the strength of the intermolecular interactions between the component.

Another problem which deserves to be studied is that of the order of the wetting transition in surfactant systems. Theory predicts that for simple fluids the wetting transition can be either a first-[62] or a second-order[75] phase transition. For surfactant systems, there are no experimental results for this problem . To study this problem, one may use enhanced videomicroscopy to observe the variations, as a function of temperature, of the contact angles between the interfaces separating the middle phase and the upper and lower phases of three-component surfactant systems.

In preliminary experiments using enhanced videomicroscopy, we have found that the major problem in this approach lies in the equilibration of the various phases of the system. Our sample is prepared in a capillary cell of size 50x8x0.4 mm. It is then set aside for 10 days without being disturbed, to allow the phases to reach equilibrium. If the sample is shaken vigorously to ensure thorough mixing, numerous small air bubbles are created and trapped in the bulk liquid phases. Even after the sample is set aside for several days, these air bubbles show no sign of leaving the liquid phases and reaching the vapor phase.

Our preliminary results for the system water/n-hexadecane/C_6E_2 at room temperature are shown in Fig. 4.9. It is seen that the middle phase forms a lens, shown in Fig. 4.9(a), which floats on the interface between the upper and lower phases, and a ring, shown in Fig. 4.9(b), which clings to the shorter edge of the same capillary cell. There are also a few spherical droplets lying on the interface between the upper and middle phases. We believe that these droplets are created by spontaneous emulsification, a phenomenon known to be associated with diffusion of the various species[76]. The presence of such droplets implies that the system has not yet reached equilibrium even after a ten-day equilibration period.

Figs. 4.10 to 4.13 show the effect of temperature on the geometry of the middle phase. These pictures are taken at various temperatures, during continuous heating from room temperature to 50 ^{o}C within 30 minutes. At room temperature (Fig. 4.9), the system is close to equilibrium and the middle phase is seen to be homogeneous with no droplets present. Since the system is heated too rapidly to allow true equilibrium to be

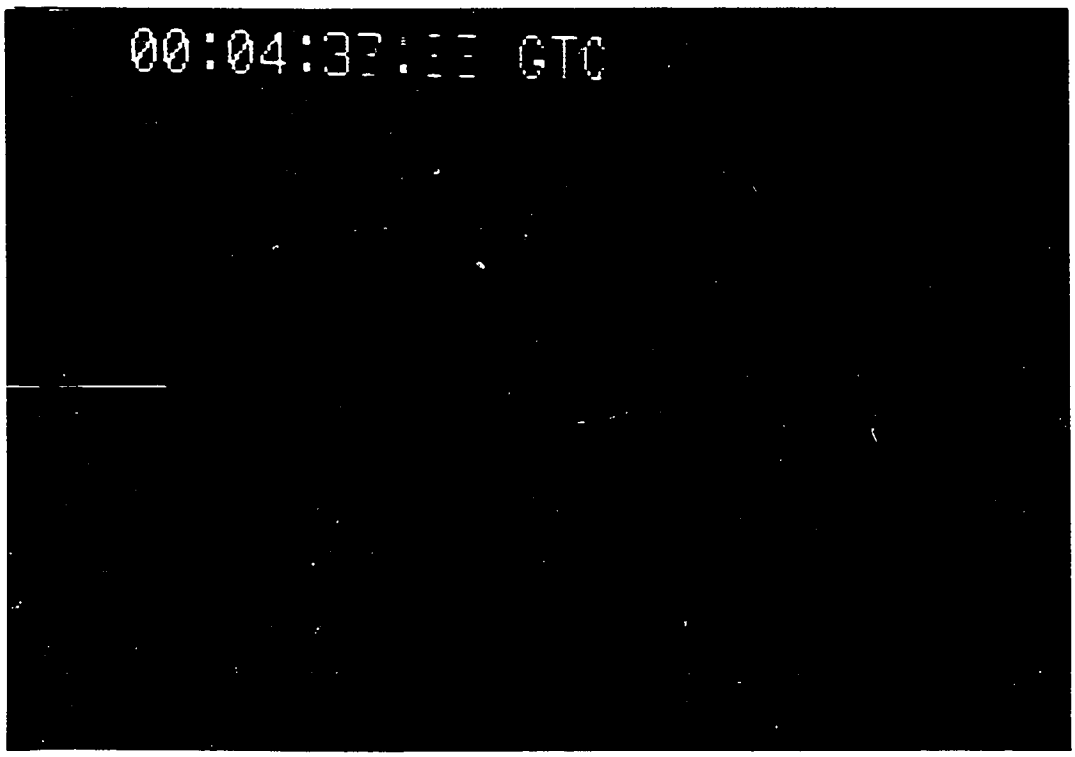

(a)

Fig. 4.9 Nonwetting middle phase in the system water/n-hexadecane/ C_6E_2 at T=25 ^{0}C: (a) Lens; (b) Ring. (continued)

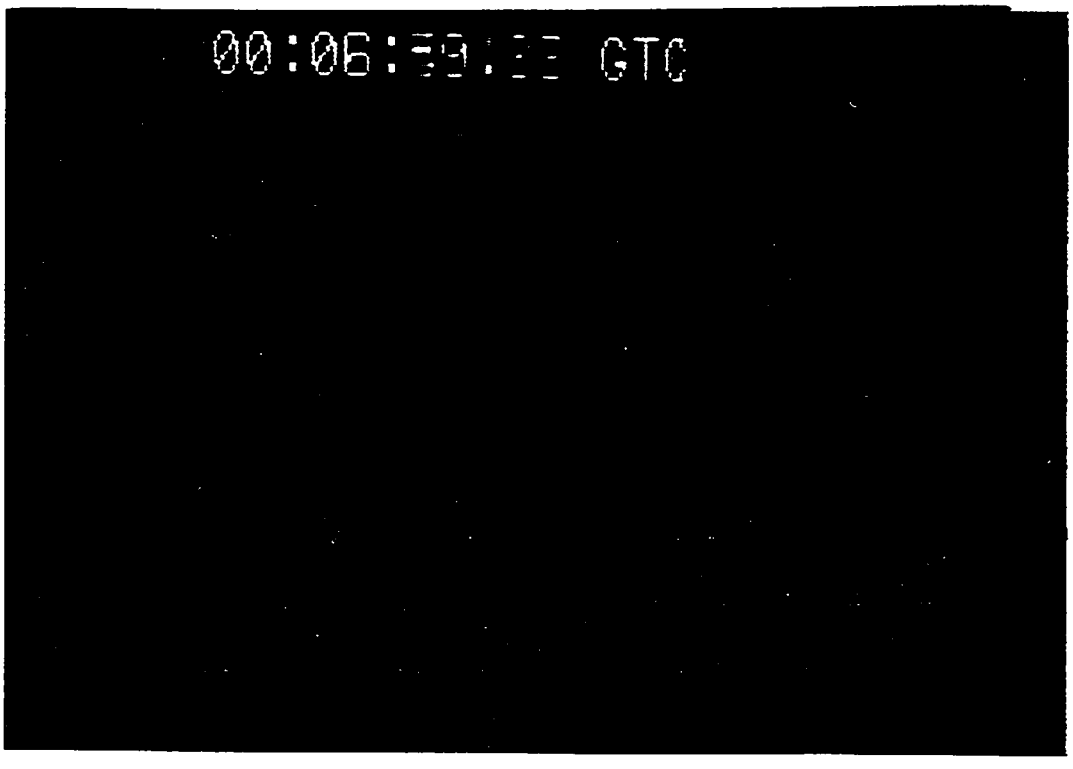

(b)

Fig. 4.9 Nonwetting middle phase in the system water/n-hexadecane/ C_6E_2 at T=25 ^{o}C: (a) Lens; (b) Ring.

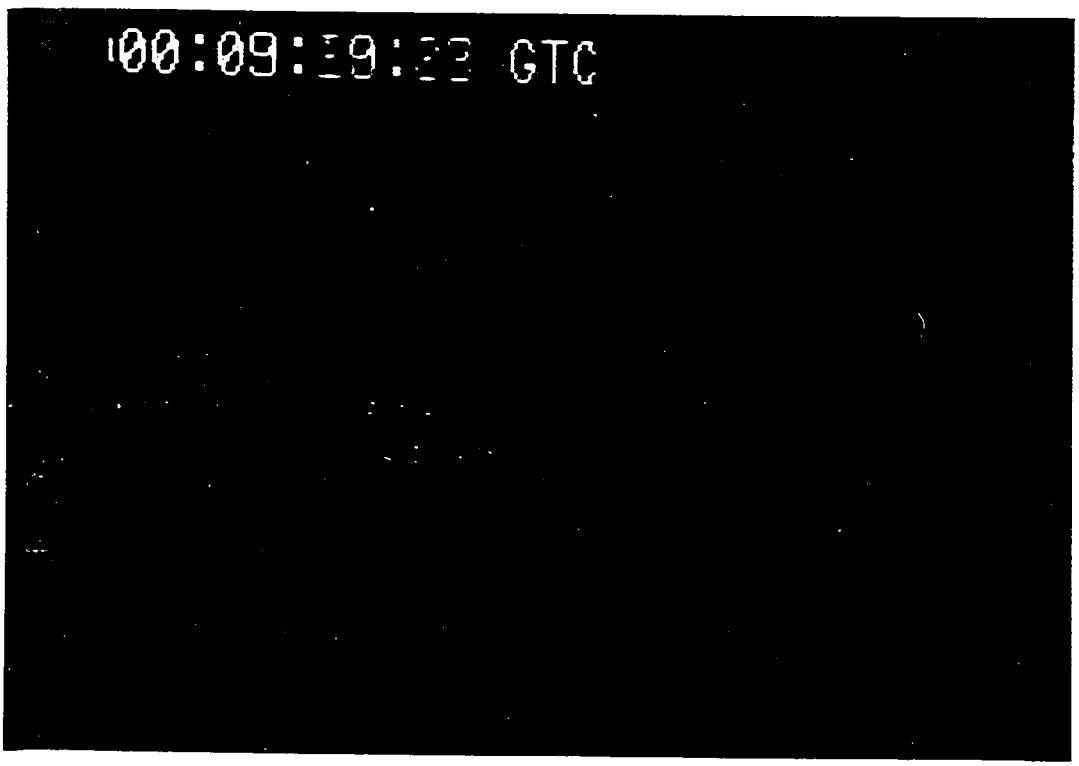

Fig. 4.10 Nonwetting middle phase in the system water/n-hexadecane/ C_6E_2 at T=35 ^{o}C.

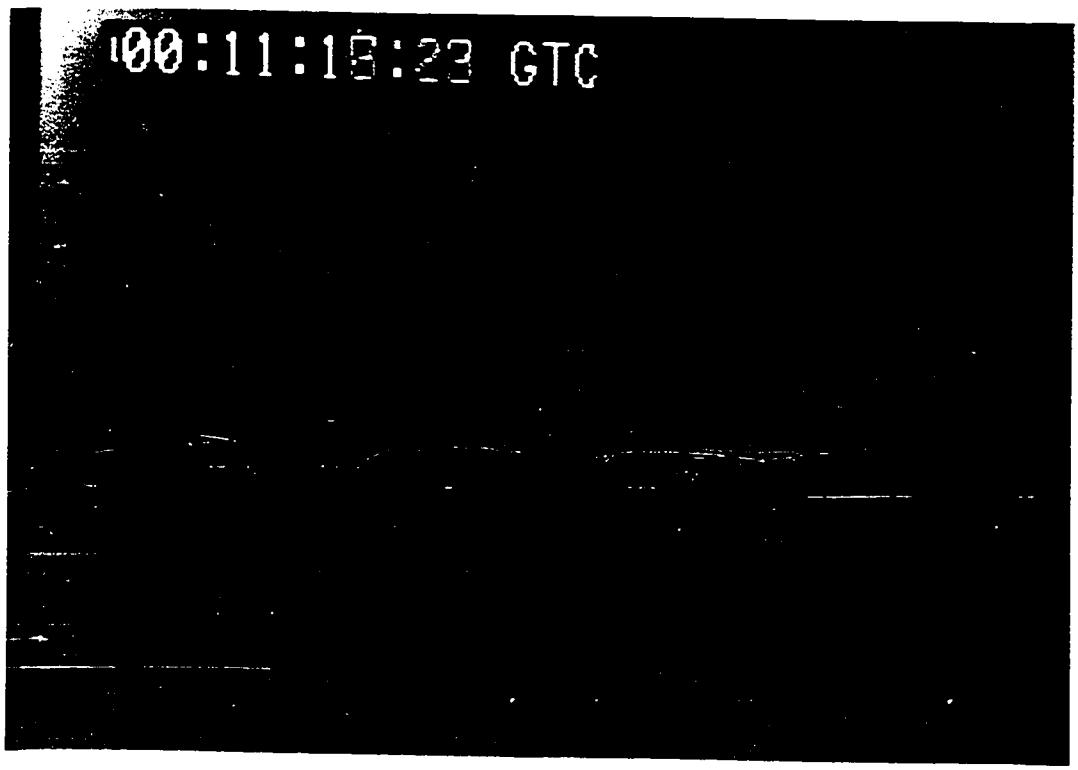

Fig. 4.11 Nonwetting middle phase in the system water/n-hexadecane/ C_6E_2 at T=42 ^{o}C.

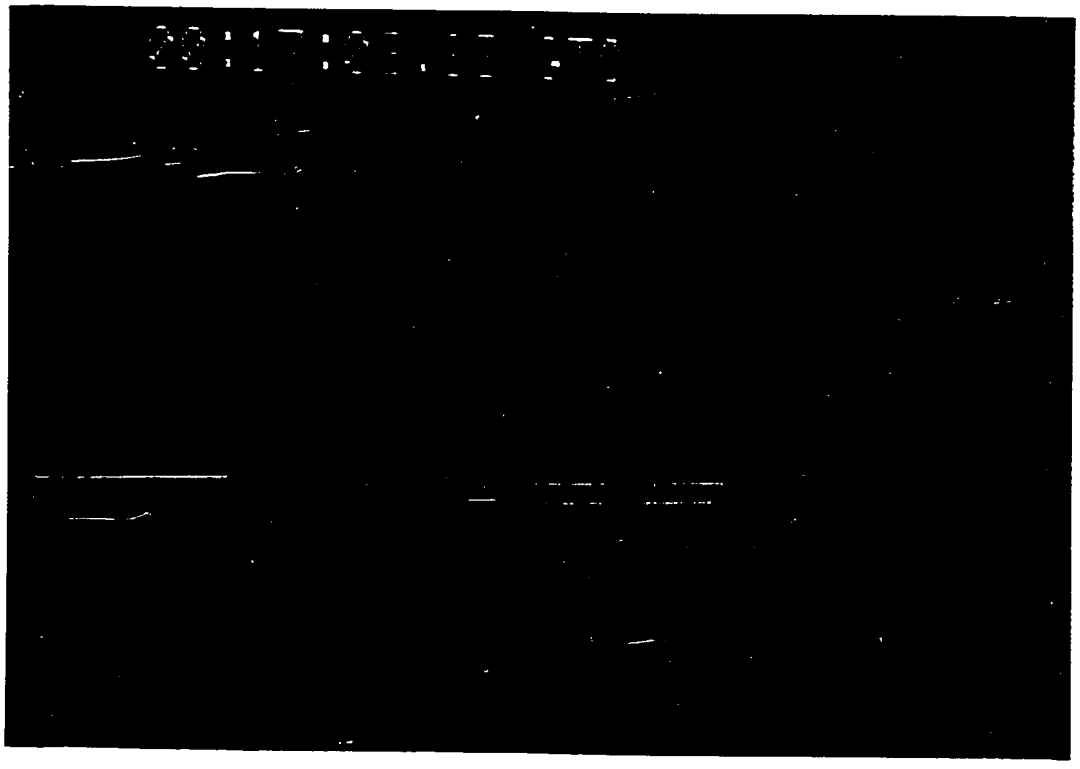

Fig. 4.12 Wetting middle phase in the system water/n-hexadecane/C_6E_2 at T=49.1 ^{o}C.

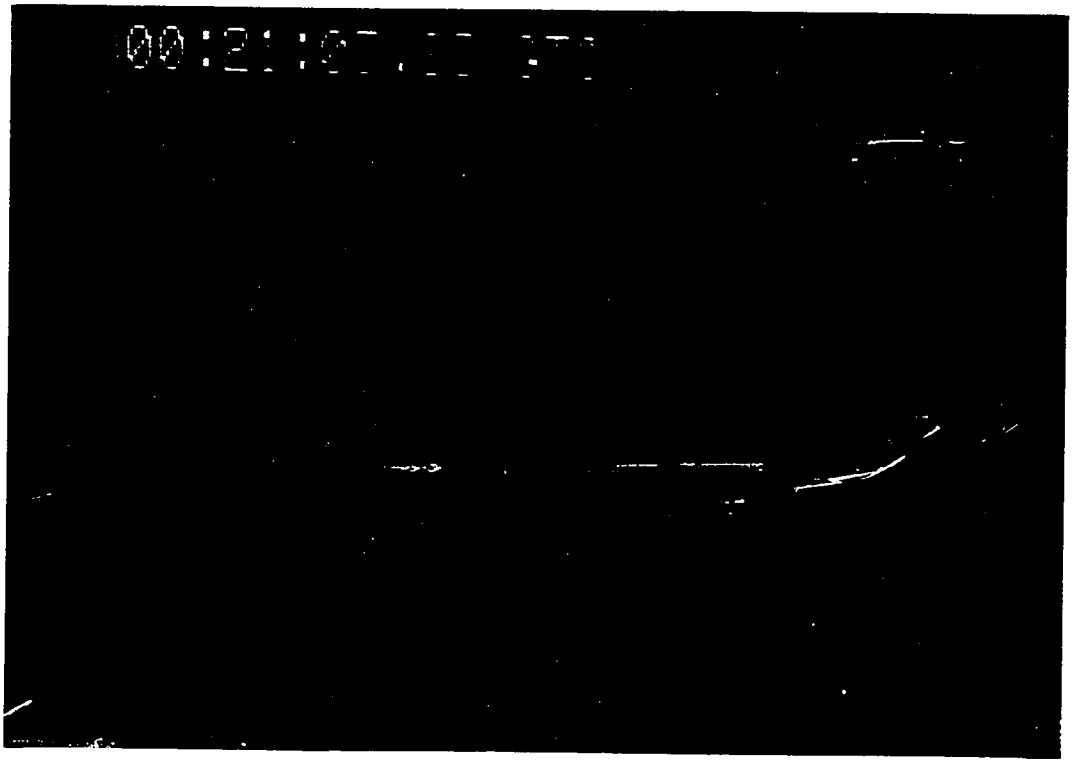

Fig. 4.13 Wetting middle phase in the system water/n-hexadecane/C_6E_2 at T=50 ^{o}C.

reached at each temperature, it is driven further away from equilibrium as temperature increases. Numerous droplets are thus created in the middle phase due to spontaneous emulsification.

In spite of this equilibration problem, Figs. 4.9 to 4.13 nevertheless successfully demonstrate the variations, as a function of temperature, of the contact angles between the interface separating the middle phase and the upper and lower phases. We observe that the contact angles become smaller as the temperature increases. Figs. 4.12 and 4.13 show the collapse of the lens tips at and above the wetting transition temperature. These figures also show that, as expected, the contact angles are equal to zero at and above the wetting transition temperature.

REFERENCES

1. This point is emphasized by: J.M.J. van Leeuwen and J.V. Sengers, Physica **132A**, 207 (1985).

2. J.D. van der Waals, Versl. Meded. Afd. Natuurk. 3rd Series, Part V, p. 171 (1889). See also the detailed memoir: Verk. K. Ned. Akad. Wet. Afd. Natuurk, Reeks **1**, 8 (1893); for a slightly shorter English translation, see: J.S. Rowlinson, J. Stat. Phys. **20**, 197 (1979).

3. S.D. Poisson, Nouvelle Theórie de l'Action Capillaire, p. 108, Bachelier, Paris (1831).

4. J.C. Maxwell, *Scientific Papers*, Vol. 2 (Dover, New York, 1965), p. 561.

5. *Miscellaneous Works of the Late Thomas Young*, George Peacock, editor (J. Murray, London, 1855), Vol. 1, pp. 462-466.

6. R. Becker, Ann. Physik **32**, 128 (1938).

7. (a) M. Robert, Kinam **6A**, 19 (1984); (b) M. Robert, Phys. Rev. Lett. **54**, 444 (1985).

8. (a) J.L. Lebowitz and J.K. Percus, J. Math. Phys. **4**, 116 (1963); (b) A.J.M. Yang, P.D. Fleming, and J.H. Gibbs, J. Chem. Phys. **64**, 3732 (1976).

9. J.W. Cahn and J.E. Hilliard, J. Chem. Phys. **28**, 258 (1958).

10. P.D. Fleming, A.J.M. Yang, and J.H. Gibbs, J. Chem. Phys. **65**, 7 (1976).

11. B. Widom, J. Chem. Phys. **43**, 3892 (1965).

12. F.P. Buff, R.A. Lovett, and F.H. Stillinger, Phys. Rev. Lett. **15**, 621 (1965).

13. J.S. Huang and W.W. Webb, J. Chem. Phys. **50**, 3677 (1969); E.S. Wu and W.W. Webb, Phys. Rev. **A8**, 2065 (1973).

14. See the review by: M.E. Fisher, J. Math. Phys. **5**, 944 (1964).

15. B. Kaufman and L. Onsager, Phys. Rev. **76**, 1244 (1949).

16. S. Fisk and B. Widom, J. Chem. Phys. **50**, 3219 (1969).

17. (a) M. Robert, Phys. Rev. **A30**, 2785 (1984); (b) F.P. Buff and M. Robert, J. Stat. Phys. **41**, 1037 (1985).

18. J.S. Huang, Ph.D. thesis, Cornell University (1969), p. 67.

19. R.A. Lovett, Ph.D. thesis, University of Rochester (1965), p. 78.

20. (a) M. Knackstedt and M. Robert, J. Chem. Phys. **89**, 3747 (1988); (b) M. Knackstedt and M. Robert, Inter. J. Thermophys. **10**, 321 (1989).

21. (a) D.B. Abraham, Phys. Rev. **B29**, 525 (1984); (b) R.F. Kayser, Phys. Rev. **A33**, 1948 (1986); (c) J.K. Percus, in *Liquid State of Matter: Fluids, Simple and Complex*, edited by E.W. Montroll and J.L. Lebowitz (North-Holland, Amsterdam, 1982).

22. (a) J. Meunier, J. Physique **48**, 1819 (1987); (b) J. Meunier and D. Langevin, J. Phys. Lett. (Paris) **43**, L185 (1982); (c) D. Beysens and M. Robert, J. Chem. Phys. **87**, 3056 (1987); (d) D. Beaglehole, in *Fluid Interfacial Phenomena*, edited by C.A. Croxton, p.523 (John Wiley & Sons Ltd., 1986).

23. D. Beaglehole, Phys. Rev. Lett. **43**, 2016 (1979).

24. (a) ref. 11; (b) D.A. Huse, W. van Saarloos, and J.D. Weeks, Phys. Rev. **B32**, 233 (1985); (c) J.D. Weeks, J. Chem. Phys. **67**, 3106 (1977).

25. D. Beaglehole, Phys. Rev. Lett. **58**, 1434 (1987).

26. M. Rao, B.J. Berne, J.K. Percus, and M.H. Kalos, J. Chem. Phys. **71**, 3802 (1979), appendix B.

27. (a) M. Robert and C. Stuart, Phys, Rev. Lett. **49**, 1434 (1982); (b) S. Fisk and B. Widom, J. Chem. Phys. **50**, 3219 (1969).

28. M. Robert and B. Widom, J. Stat. Phys. **37**, 419 (1984).

29. See, for example: J.S. Rowlinson and B. Widom, *Molecular Theory of Capillary*, Clarendon Press, Oxford, 1982, p.180.

30. J.H. Sikkenk, J.M.J. van Leeuwen, E.O. Vossnack, and A.F. Bakker, Physica **146A**, 622 (1987).

31. M.W. Kim and D.S. Cannell, Phys. Rev. Lett. **35**, 899 (1975).

32. H.K. Kim and M.H.W. Chan, Phys. Rev. Lett. **53**, 170 (1984).

33. (a) L. Onsager, Phys. Rev. **65**, 117 (1944); (b) M.E. Fisher, J. Phys. Soc. Japan **26**, 87 (1969).

34. G.A. Hawkins and G.B. Benedek, Phys. Rev. Lett. **32**, 524 (1974).

35. For d =3, see, for example: (a) J.K. Lee, J.A. Barker, and G.M. Pound, J. Chem. Phys. **60**, 1976 (1974); (b) M.P. D'Evelyn and S.A. Rice, J. Chem. Phys. **78**, 5081 & 5225 (1983); (c) M.J.P. Nijmeijer, A.F. Bakker, C. Bruin, and J.H. Sikkenk, J. Chem. Phys. **89**, 3789 (1988); (d) G.A. Chapela, G. Saville, and J.S. Rowlinson, Faraday Disc. Chem. Soc. **59**, 22 (9175); (e) G.A. Chapela, G. Saville, S.M. Thompson and J.S. Rowlinson, Faraday Trans. II **73**, 1133 (1975); (f) D.J. Lee, M.M. Telo da Gama, and K.E. Gubbins, Mol. Phys. **53**, 1113 (1984); (g) T.R. Osborn and C.A. Croxton, Mol. Phys. **34**, 841 (1977); (h) K.S. Liu, J. Chem. Phys. **60**, 4226 (1974).

36. For d =2, see, for example: S. Toxvaerd, J. Chem. Phys. **62**, 1589 (1975); F.F. Abraham, J. Chem. Phys. **72**, 1412 (1980); J.H. Sikkenk, H.J. Hilhorst and A.F. Bakker, Physica **131A**, 587 (1985).

37. D.W. Heermann, *Computer simulation methods in theoretical physics*, Springer-Verlag, Berlin Heidelberg, 1986.

38. J.p. Hansen and I.R. McDonald, *Theory of simple liquids* (2nd ed.), Academic Press, New York, 1986, Chap. 3.

39. M.P. Allen and D.J. Tildesley, *Computer simulation of liquids*, Clarendon Press, Oxford, 1987.

40. (a) N. Metropolis and S. Ulam, J. Am. Stat. Ass. **44**, 335 (1949); (b) N. Metropolis, A.W. Rosenbluth, M.N. Rosenbluth, A.H. Teller, and E. Teller, J. Chem. Phys. **21**, 1087 (1953).

41. B.J. Alder and J.E. Wainwright, J. Chem. Phys. **27**, 1208 (1957); **51**, 459 (1959).

42. A. Rahman, Phys. Rev. **136A**, 405 (1964).

43. (a) D. Beeman, J. Comput. Phys. **20**, 130 (1976); (b) H.J.C. Berendsen and W.F. van Gunsteren, *Molecular dynamics simulation of statistical mechanical systems*. Proceedings of the Enrico Fermi Summer School, Varenna, pp 43-65, 1985, Soc. Italiana di Fisica, Bologna.

44. (a) C.W. Gear, Report ANL 7126, Argonne National Laboratory, 1966; (b) C.W. Gear, *Numerical initial value problems in ordinary differential equations*, Prentice-Hall, Englewood Cliffs, NJ, 1971.

45. L. Verlet, Phys. Rev. **159**, 98 (1967).

46. N.D. Mermin, Phys. Rev. **176**, 250 (1968).

47. J.A. Barker, D. Henderson, and F.F. Abraham, Physica **106A**, 226 (1981).

48. J. Lekner and J.R. Henderson, Physica **94A**, 545 (1978).

49. D.B. Abraham and P. Reed, Phys. Rev. Lett. **33**, 377 (1974) and Commun. Math. Phys. **49**, 35 (1976); see also: J. Bricmont, J.L. Lebowitz, and C.E. Pfister, J. Stat. Phys. **26**, 313 (1981).

50. J.V. Sengers and J.M.J. van Leeuwen, J. Phys. Chem. **88**, 6479 (1984).

51. For a review, see: D.E. Sullivan and M.M. Telo da Gama, in *Fluid Interfacial Phenomena*, edited by C.A. Croxton, Wiley, 1985.

52. (a) M. Kahlweit and R. Strey, Angew. Chem. Int. Ed. Engl. **24**, 654 (1985); (b) P.K. Kilpatrick, C.A. Gorman, H.T. Davis, L.E. Scriven, and W.G. Miller, J. Phys. Chem. **90**, 5292 (1986); (c) H. Kunieda and S.E. Friberg, Bull. Chem. Soc. Jpn. **54**, 1010 (1981); (d) M. Kahlweit, R. Strey, and D. Haase, J. Phys. Chem. **89**, 163 (1985).

53. P.A. Winsor, Trans. Faraday Soc. **44**, 376 (1948).

54. (a) H. Kunieda and K. Shinoda, J. Disp. Sci. Technol. **3**, 233 (1982); (b) M. Kahlweit and R. Strey, Angew. Chem. Int. Ed. Engl. **24**, 654 (1985); (c) H. Kunieda and S.E. Friberg, Bull. Chem. Soc. Jpn. **54**, 1010 (1981).

55. F.P. Buff and H. Saltsburg, J. Chem. Phys. **26**, 23 (1957).

56. (a) G.N. Antonow, J. Chim. Phys. **5**, 372 (1907); Kolloid-Zeit. 59, 7 (1932); **64**, 336 (1933); (b) N.K. Adam, *The Physics and Chemistry of Surfaces*, 3rd ed., pp. 7, 214-5, Oxford University Press (1941).

57. (a) F. Neumann, *Vorlesungen über die Theorie der Capillarität* (ed. A. Wangerin) Chapter 6, Sect. 1, especially pp 161-2, Teubner Leipzig (1894); (b) F.P. Buff and H. Saltsburg, J. Chem. Phys. **26**, 23 (1957); (c) F.P. Buff, *Encyclopedia of Physics* (ed. S. Flugge) Vol. 10, Sect. 7, pp. 298-9, Springer, Berlin (1960).

58. (a) R.L. Reed and R.N. Healy, in *Improved Oil Recovery by Surfactant and Polymer Flooding*, eds. D.O. Shah and R.S. Schechter, Academic Press, New York (1977); (b) A. Pouchelon, J. Meunier, D. Langevin, D. Chatenay, and A.M. Cazabat, Chem. Phys. Lett. **76**, 277 (1980); (c) A.M. Bellocq, J. Biais, P. Bothorel, B. Clin, G. Fourche, P. Lalanne, B.

Lemaire, B. Lemanceau, and D. Roux, Adv. Colloid Interface Sci. **20**, 167 (1984); (d) A.M. Bellocq, D. Bourbon, B. Lemanceau, and G. Fourche, J. Colloid Interface Sci. **89**, 427 (1982).

59. M. Kahlweit, R. Strey, P. Firman, D. Haase, J. Jen, and R. Schomacker, Langmuir **4**, 499 (1988).

60. J. Jeng and C.A. Miller, Colloids Surfaces **28**, 247 (1987).

61. (a) Y. Seeto, J.E. Puig, L.E. Scriven, and H.T. Davis, J. Colloid Interface Sci. **96**, 360 (1983); (b) J.C. Lang and B. Widom, Physica **A81**, 190 (1975).

62. (a) J.W. Cahn, J. Chem. Phys. **66**, 3667 (1977); (b) C. Ebner and W.F. Saam, Phys. Rev. Lett. **38**, 1486 (1977).

63. M.R. Moldover and J.W. Cahn, Science **207**, 1073 (1980).

64. See, for example: D.W. Pohl and W.I. Goldburg, Phys. Rev. Lett. **48**, 1111 (1982).

65. J. Garcia, C. Guerrero, J.G. Llanes and A. Robledo, J. Phys. Chem. **90**, 1350 (1986).

66. J. van Niewkoop and G. Snoei, Shell Research, B.V. publication No. 674, Jan. 1983, presented at World Surfactant Congress, Sect. C-3, Munich, May 1984.

67. M. Kahlweit et al, J. Colloid Interface Sci. **118**, 436 (1987).

68. G.H. Findenegg, private communication (1989).

69. F. Perrot, M. Robert and D. Beysens, private communication (1988).

70. M. Robert and J.F. Jeng, J. Phys. France **49**, 1821 (1988).

71. B. Widom, Langmuir **3**, 12 (1987).

72. (a) P.K. Kilpatrick, H.T. Davis, L.E. Scriven, and W.G. Miller, J. Colloid interface Sci. **118**, 270 (1987); (b) M. Kahlweit, R. Strey, and D. Haase, J. Phys. Chem. **89**, 163 (1985); (c) M. Kahlweit, R. Strey, P. Firman, D. Haase, J. Jen, and R. Schomacker, Langmuir **4**, 499 (1988); (d) F. Lichterfeld, T. Schmeling, and R. Strey, J. Phys. Chem. **90**, 5762 (1986); (e) A.M. Bellocq, D. Bourbon, B. Lemanceau, and G. Fourche, J. Colloid Interface Sci. **89**, 427 (1982).

73. B. Owenson and L. Pratt, J. Phys. Chem. **88**, 2905 (1984); P. van der Ploeg and H.J.C. Berendsen, Mol. Phys. **49**, 233 (1983); J.M. Haile and J.P. O'Connell, J. Phys. Chem. **88**, 6363 (1984).

74. R.G. Larson, J. Chem. Phys. 89, 1642 (1988).

75. D.E. Sullivan, J. Chem. Phys. **74**, 2604 (1981).

76. C.A. Miller and P. Neogi, *Interfacial Phenomena*, Marcel Dekker Inc., New York, 1985, pp.281-285.